JET PROPULSION

A publication of the

AMERICAN ROCKET SOCIETY

Research and Development

BIND

VOLUME 28 JANUARY 1958 NUMBER 1

INVITED ARTICLE

Recent Advances in Comets . . . . . *Robert Steinitz* 15

CONTRIBUTED ARTICLES

Inertial Guidance for Rocket-Propelled Missiles . . . . . *William T. Russell* 17

A Deceleration Probe for Measuring Stagnation Pressure and Velocity of a Particle-Laden Gas Stream . . . . . *John L. Dussourd and Ascher H. Shapiro* 24

Mass-Transfer Cooling of a Laminar Boundary Layer by Injection of a Light-Weight Foreign Gas . . *E. R. G. Eckert, P. J. Schneider, A. A. Hayday and R. M. Larson* 34

The Temperature History in a Thick Skin Subjected to Laminar Heating During Entry into the Atmosphere . . . . . *George W. Sutton* 40

Factors Which Influence the Suitability of Liquid Propellants as Rocket Motor Regenerative Coolants . . . . . *D. R. Bartz* 46

TECHNICAL NOTES

Criteria for Orbital Entry . . . . . *Louis G. Varga* 54

Maximality for Problems in Vertical and Horizontal Rocket Flight . . . . . *Stanley Ross* 55

On Turbulent Heat Transfer through a Highly Cooled Partially Dissociated Boundary Layer . . . . . *Ronald F. Probstein, Mac C. Adams and Peter M. Rose* 56

Heat Transfer to a General Three-Dimensional Stagnation Point . . . . . *Eli Reshotko* 58

On the Rational Choice of Flame-Holder Shape . . . . . *Abbott A. Putnam* 60

DEPARTMENTS

Book Reviews 61 New Patents 64 Technical Literature Digest 66

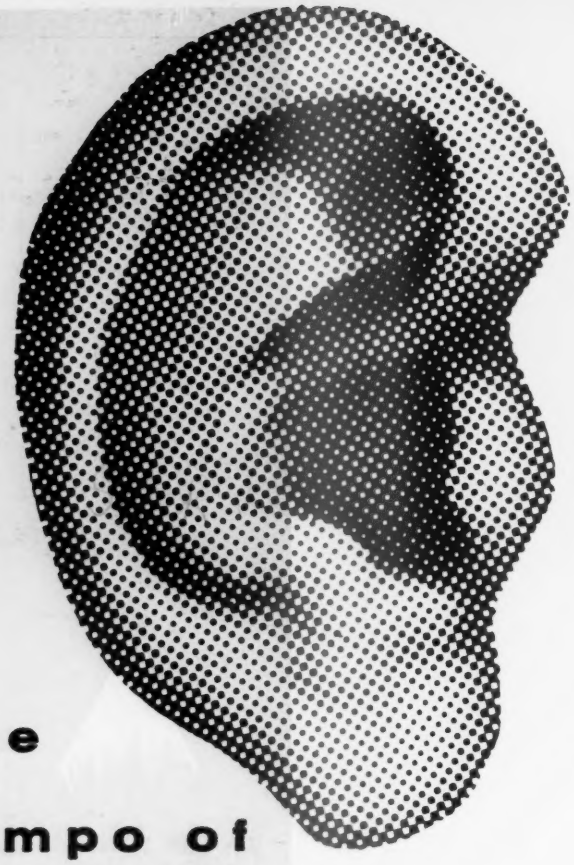

tuned to the tempo of tomorrow

Open ears lead to the open thinking that made possible today's rocket powerplants. They are alert ears—ears acutely sensitive to the unsolved problems that must be conquered in designing powerplants for the vehicles of the future.

RMI puts a premium on just such thinking. Its engineers and scientists form a talented, alert team, efficiently and effectively meeting the rocket power needs of tomorrow.

Engineers, Scientists—Perhaps you, too, can work with America's *first* rocket family. You'll find the problems challenging, the rewards great.

Power for Progress

4841

RMI

REACTION MOTORS, INC.

A MEMBER OF THE OMAR TEAM

DENVILLE, NEW JERSEY

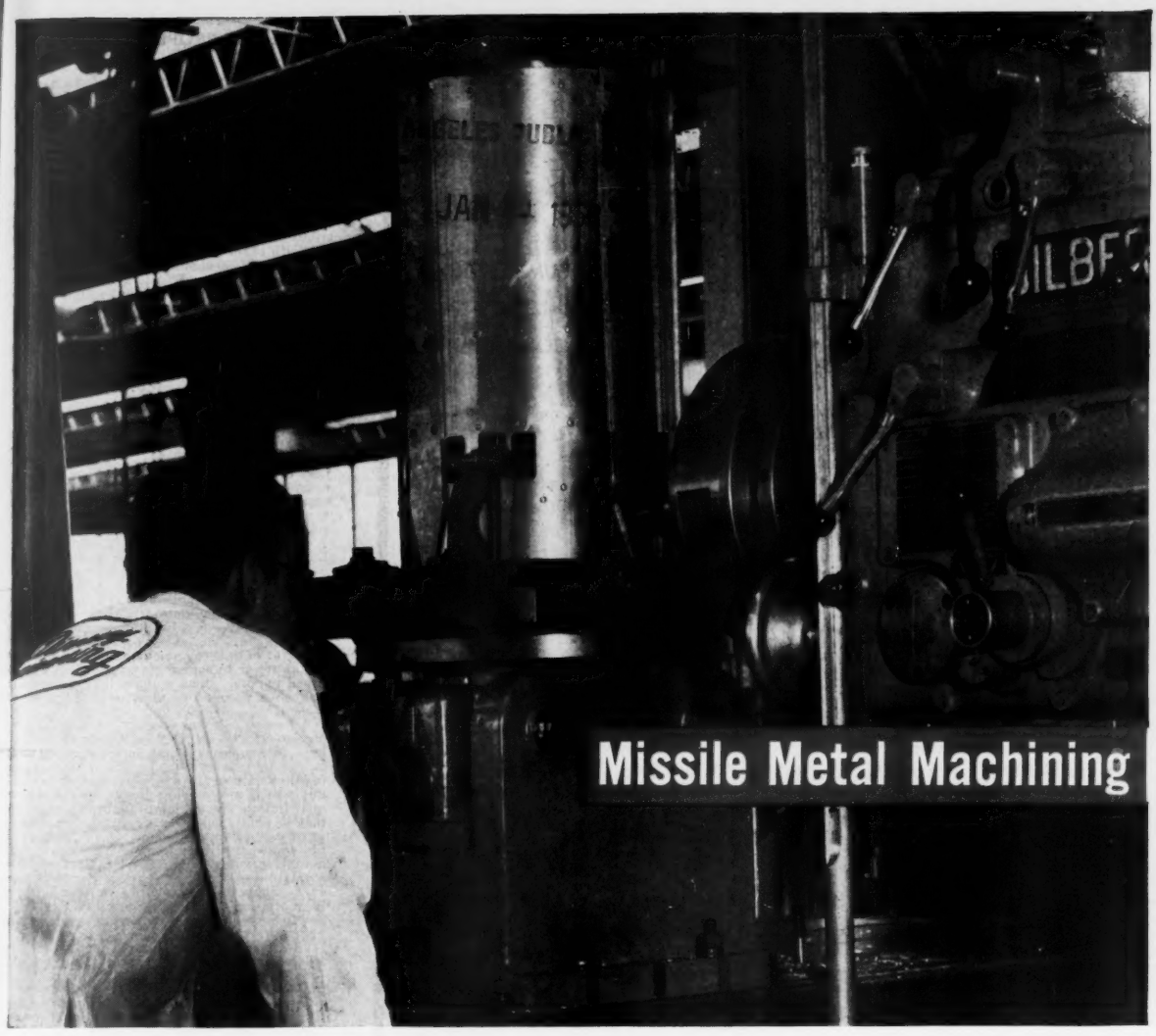

Another Tough Job

Above you see an extremely complex body section of a missile being finish machined on a horizontal boring mill. You are looking at another intricate example of Diversey skill and craftsmanship. A visit to our plants would show you many comparable jobs that would astonish you.

At Diversey you have the LARGEST FACILITIES exclusively devoted to your missile metal machining problems. You work with fast, precise, and progressive technical people who know what works and what won't. Bring your tough jobs to Diversey.

HYDROSPINNING NOW AVAILABLE

A new Hydrospinning Division has been formed at Diversey which uses the latest and largest equipment to produce intricate missile parts.

SEND FOR FREE BOOKLET

LEADERS IN CONTOUR MACHINING

Diversey ENGINEERING COMPANY

10550 WEST ANDERSON PLACE
FRANKLIN PARK, ILLINOIS • *A Suburb of Chicago*

FROM NOSE TO NOZZLE, FROM FIN TO FIN, CONTOUR TURNED PARTS—WITH PRECISION BUILT IN

JET PROPULSION

A publication of the

AMERICAN ROCKET SOCIETY

Research and Development

IRWIN HERSEY—DIRECTOR OF PUBLICATIONS

EDITOR MARTIN SUMMERFIELD

ASSISTANT EDITOR STANLEY BEITLER

ART EDITOR JOHN CULIN

ASSOCIATE EDITORS

ALI BULENT CAMBEL, *Northwestern University*
IRVIN GLASSMAN, *Princeton University*
M. H. SMITH, *Princeton University*

1958
Sci R v. 28

CONTRIBUTORS

MARSHAL FISHER, *Princeton University*
GEORGE F. McLAUGHLIN

ADVERTISING & PROMOTION MANAGER

WILLIAM CHENOWETH

ADVERTISING REPRESENTATIVES

D. C. Emery & Associates
155 East 42 St., New York, N. Y.
Telephone: Yukon 6-6855

James C. Galloway & Co.
6535 Wilshire Blvd., Los Angeles, Calif.
Telephone: Olive 3-3223

Jim Summers & Associates
35 E. Wacker Dr., Chicago, Ill.
Telephone: Andover 3-1154

R. F. and Larry Pickrell
318 Stephenson Bldg., Detroit, Mich.
Telephone: Trinity 1-0790

Louis J. Bresnick
304 Washington Ave., Chelsea 50, Mass.
Telephone: Chelsea 3-3335

AMERICAN ROCKET SOCIETY

Founded 1930

OFFICERS

President	George P. Sutton
Vice-President	John P. Stapp
Executive Secretary	James J. Harford
Secretary	A. C. Slade
Treasurer	Robert M. Lawrence
General Counsel	Andrew G. Haley

BOARD OF DIRECTORS

Terms expiring on dates indicated

Krafft Ehricke, 1959	H. S. Seifert, 1958
S. K. Hoffman, 1958	K. R. Stehling, 1958
Simon Ramo, 1960	Martin Summerfield, 1959
H. W. Ritchey, 1959	Wernher von Braun, 1960

Maurice J. Zucrow, 1960

TECHNICAL DIVISION CHAIRMEN

David G. Simons, Human Factors	John F. Tormey, Propellants and Combustion
Lawrence S. Brown, Instrumentation and Guidance	Brooks T. Morris, Ramjet
Edward N. Hall, Liquid Rocket	William L. Rogers, Solid Rocket

Krafft A. Ehricke, Space Flight

Scope of JET PROPULSION

This Journal is a publication of the American Rocket Society devoted to the advancement of the field of jet propulsion through the dissemination of original papers disclosing new knowledge or new developments. As used herein, the term "jet propulsion" embraces all engines that develop thrust by rearward discharge of a jet through a nozzle or duct; and thus it includes air-consuming engines and underwater systems as well as rockets. JET PROPULSION is open to contributions dealing not only with propulsion but with other aspects of jet-propelled flight, such as flight mechanics, guidance, telemetering, and research instrumentation. Increasing emphasis will be given to the scientific problems of extraterrestrial flight.

Information for Authors

Manuscripts must be as brief as the proper presentation of the ideas will allow. Exclusion of dispensable material and conciseness of expression will influence the Editors' acceptance of a manuscript. In terms of standard-size double-spaced typed pages, a typical maximum length is 22 pages of text (including equations), 1 page of references, 1 page of abstract, and 12 illustrations. Fewer illustrations permit more text, and vice versa. Greater length will be acceptable only in exceptional cases.

Short manuscripts, not more than one quarter of the maximum length stated for full articles, may qualify for publication as Technical Notes. They may be devoted either to new developments requiring prompt disclosure or to comments on previously published papers. Such manuscripts are usually published within two months of the date of receipt.

Sponsored manuscripts are published occasionally as an ARS service to the industry. A manuscript that does not qualify for publication according to the above-stated requirements as to subject scope or length, but which nevertheless deserves widespread distribution among jet propulsion engineers, may be printed as an extra part of the Journal or as a special supplement, if the author or his sponsor will reimburse the Society for actual publication costs. Estimates are available on request. Acknowledgment of such financial sponsorship appears as a footnote on the first page of the article. Publication is prompt since such papers are not in the ordinary backlog.

Manuscripts must be double spaced on one side of paper only with wide margins to allow for instructions to printer. Include a 100 to 200 word abstract. State the authors' positions and affiliations in a footnote on the first page. Do not type equations; write them in ink. Identify unusual symbols or Greek letters for the printer. References are to be grouped at the end of the manuscript and are to be given as follows: for journal articles: authors first, then title, journal, volume, year, page numbers; for books: authors first, then title, publisher, city, edition, and page or chapter numbers. Line drawings must be clear and sharp to make clear engravings. Use black ink on white paper or tracing cloth. Lettering should be large enough to be legible after reduction. Photographs should be glossy prints, not matte or semi-matte. Each illustration must have a legend; legends should be listed in order on a separate sheet.

Manuscripts must be accomplished by written assurance as to security clearance in the event the subject matter lies in a classified area or if the paper originates under government sponsorship. Full responsibility rests with the author.

Submit manuscripts in duplicate (original plus first carbon, with two sets of illustrations) to the Editor, Martin Summerfield, Professor of Aeronautical Engineering, Princeton University, Princeton, N. J. Preprints of papers presented at ARS national meetings are automatically considered for publication.

JET PROPULSION is published monthly by the American Rocket Society, Inc., and the American Interplanetary Society at 20th & Northampton Sts., Easton, Pa., U. S. A. Editorial offices: 500 Fifth Ave., New York 36, N. Y. Price: $12.50 per year, $2.00 per single copy. Entered as second-class matter at the Post Office at Easton, Pa. Notice of change of address should be sent to the Secretary, ARS, at least 30 days prior to publication. Opinions expressed herein are the authors' and do not necessarily reflect the views of the Editors or of the Society.

© Copyright 1958 by the American Rocket Society.

RECENT ADVANCES IN CERMETS*

BY ROBERT STEINITZ[1]

American Electro Metal Div. of Firth Sterling, Inc., Yonkers, N. Y.

The author, born in 1909 in Germany, came to this country after completing university training at Goettingen where he obtained a doctorate in physics. Since coming to this country in 1936 he has been intimately associated with problems in solid state physics and metallurgy. As Director of Research of the American Electro Metal Division of Firth Sterling, Inc., Dr. Steinitz has contributed extensively to the powder metallurgy and high temperature material fields. Co-author of several books and contributor of about 20 papers to the scientific literature, Dr. Steinitz now focuses his attention on cermets and problems associated with their practical use.

Introduction
Competition with Superalloys

DURING the last two years, the somewhat vague and wishful thinking of the past about applications of cermets as high temperature materials has come to a more definite conclusion as to where these materials could and should be applied. The shortcomings of cermet materials—either based on mixtures of metals with true oxide ceramics or on combinations of refractory hard metals with so-called binder materials—have, first of all, almost excluded applications below 1700 to 1800 F. The development of special nickel base alloys (1)[2] has stretched the usable range to above 1700 F, with long-time strength properties close to those of the most common cermet material, titanium carbide with nickel. It does not seem worthwhile to struggle with the brittleness and fabrication difficulties of cermet materials, when it is possible to sacrifice only a small amount of strength and to use instead a material which at least can be cast, if not fabricated by rolling and other common forming procedures. However, the limit of the nickel base materials has been reached, as the melting point is being closely approached. The excellent high temperature properties of cermets (2) become more apparent when the temperature considered for their application is so high that no materials based on iron, nickel, or cobalt alloys are usable any longer. The development of molybdenum has to a limited extent influenced the applicability of cermet materials. While molybdenum has phenomenal strength at high temperature, its lack of oxidation resistance is a serious handicap.

At present, the use of cermet materials on the basis of carbides, borides, nitrides and silicides has, therefore, experienced a serious re-evaluation. This is not due to any failure of cermet materials or to any unfulfilled promise by them. Properties of cermets determined earlier are still correct and have even been improved lately, but the development of nickel base materials has forced the cermets into a new field, where they can perform, while all other materials fail. The use of such extremely high temperatures is not yet common practice, as a large number of serious difficulties confront the designer. To be able to make certain highly stressed parts out of cermet materials for use at temperatures above 3000 F, is not sufficient for the designer who has to take the behavior of the complete assembly into account.

Pure Hard Metals for Still Higher Temperatures

The word "cermet" should be somehow re-defined in the light of the above. If titanium carbide with a nickel binder has so far been considered a typical representative of this kind of materials, it should be understood that the material would have only limited applicability in the field of very high temperatures because the melting point of the binder, or rather the eutectic temperature between the metal and the hard phase which is often considerably lower, limits the applications. The useful temperature is even lower than this point. Titanium carbide-nickel cermets cannot be employed much above 2000 to 2200 F. Boride base cermets with a chromium or chromium-molybdenum binder have a somewhat higher range of possible application, but the gain in temperature range is not large.

The range in which these materials presently are being tried lies considerably higher. In such cases, the amount of binder is decreased to a very small minimum, or the refractory hard metals are used by themselves without the addition of another metal. If a liquid phase during sintering is desired, this can in some cases be obtained by the eutectic between two or more hard metals, or by the addition of a lower melting hard metal to the main constituent. Actually these materials no longer deserve the name "cermet"—they contain neither a ceramic nor a pure metal—but common usage right now is to include these pure refractory metallic materials in this category.

The use of temperatures from 2500 to 5000 F requires the highest melting materials known (3). In addition to the refractory metals, such as molybdenum, only two groups of material can be considered at all. The first is that of the ceramic oxides, where melting points around the above mentioned temperatures are quite common. The other group is that of the refractory hard metals, as a number of carbides, borides and silicides melt within this range. Applications include rocket motors and combustion chambers in high speed planes. In addition, the problem of aerodynamic heating in supersonic flight has opened a new field for these materials. At present, cooling of the exposed parts is considered the easier method. New production procedures had to be devised to make it possible to apply the high melting compounds to such parts. These manufacturing procedures or coatings will be discussed later. Another field of application which has just started to open its doors lies in materials for nuclear reactors (4). Some of the hard metal materials have desirable nuclear properties for certain applica-

(Continued on page 68)

[1] Director of Research

[2] Numbers in parentheses indicate References at end of paper.

* This paper is the first of a monthly series of invited articles that will describe new developments in specialized areas of jet and rocket engineering.

MAR 25 1959

CAMERAS RECORD NUCLEAR WEAPONS TEST DROPS

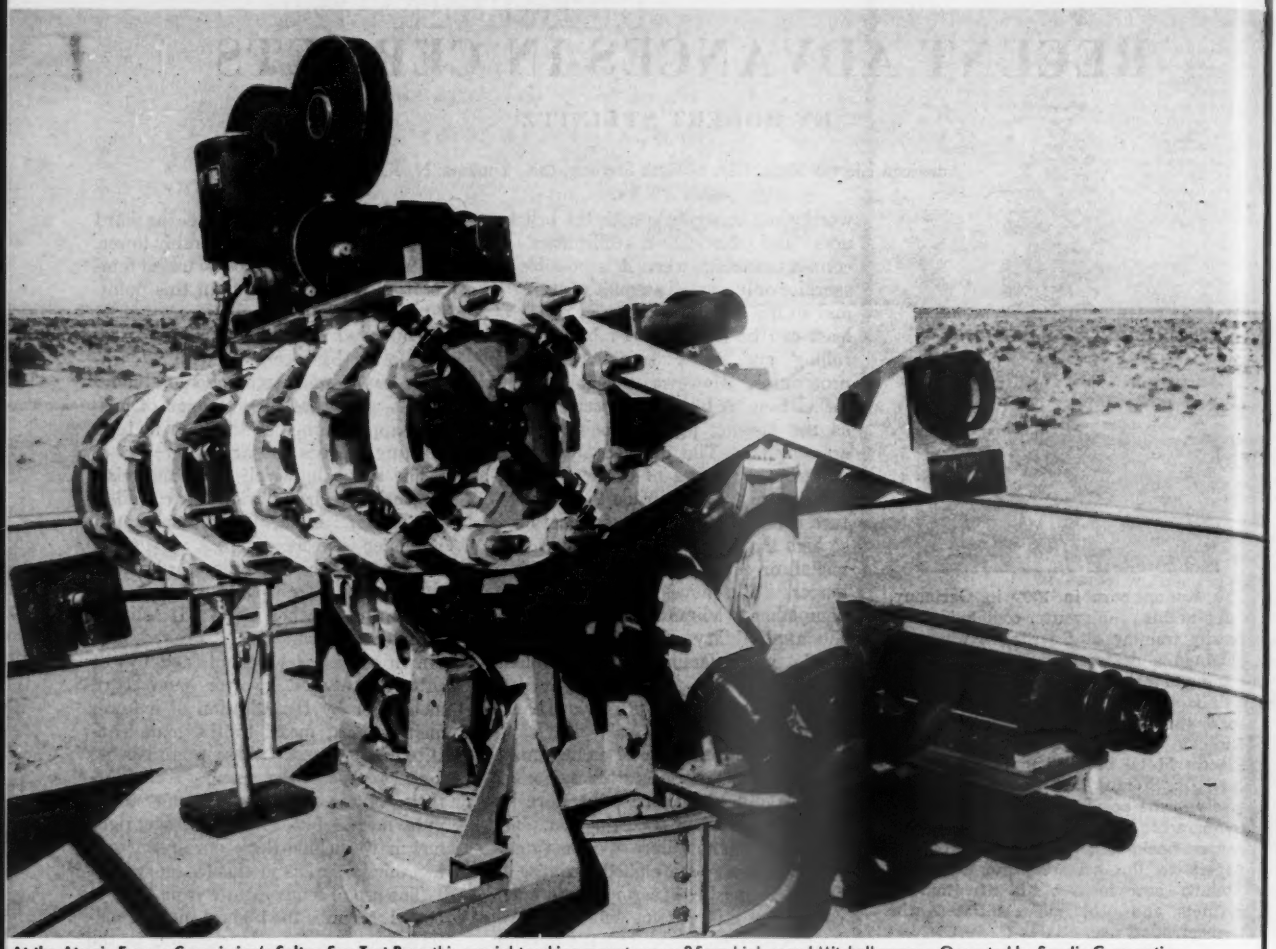

At the Atomic Energy Commission's Salton Sea Test Base this special tracking mount uses a 35mm high speed Mitchell camera. Operated by Sandia Corporation, this base uses Mitchell cameras for recording test operations.

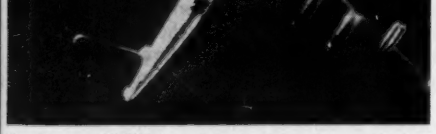

Tracking at 40,000 feet, this film frame from a Mitchell camera operating at 96 frames per second provides an accurate record.

Salton Sea Test Base Uses Mitchell Cameras to Capture High Speed Action of Dummy Bombs

High speed flight and laboratory tests, which hitherto have been difficult or impossible to view with the human eye, are today providing revealing information through high speed film recordings.

Typical example of the widespread use of high speed cameras is the Salton Sea Test Base in Southern California, where drop testing of "dummy" bombs is a major activity. In testing carried on there, by Sandia Corporation for the Atomic Energy Commission, as many as 20 Mitchell high speed cameras may record different angles in the flight of an experimental weapon "shape" from drop aircraft to impact area.

Operating at 48 to 100 frames per second, the Mitchell cameras film accurate, steady images with maximum uniformity—even under difficult and complicated filming conditions.

Mitchell cameras play a growing role in today's research and development—just as 16mm and 35mm Mitchell cameras have become the leading professional motion picture equipment used by industry, television, and film studios throughout the world. Write on your letterhead for further information on the uses of Mitchell cameras in the field of military and industrial research.

High speed Mitchell Camera in operation on tracking telescope mount during test run at Salton Sea.

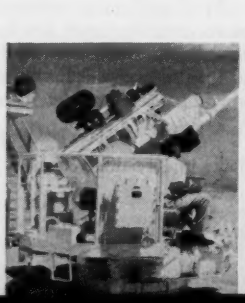

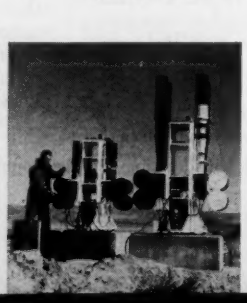

Photogrammetric mounts for 8 Mitchell cameras determine the position in space of a nuclear explosion.

Mitchell Camera
CORPORATION
666 WEST HARVARD STREET
GLENDALE 4, CALIFORNIA
Cable Address: "MITCAMCO"

Inertial Guidance for Rocket-Propelled Missiles[1]

WILLIAM T. RUSSELL[2]

The Ramo-Wooldridge Corp., Los Angeles, Calif.

The basic elements of inertial guidance systems primarily intended for rocket-propelled missiles are explained. Precision gyroscopes, accelerometers and stabilized platforms are described. Guidance schemes appropriate to ballistic missiles are discussed and a trajectory for the German V-2 rocket is presented as an example. The problem of gravity computation is considered and the effect of instrument errors is explored. A missile steering computer and a rocket motor shut-off computer are given for the V-2 rocket which is used as an example. Numerical values of coefficients are calculated for the sample trajectory.

Introduction

PREVIOUS published papers on inertial guidance have considered the problem of navigating at constant altitude over the earth's surface in aircraft, ships or submarines (1–5).[3] Although one of the first applications of inertial guidance was in the German V-2 missile, the use of inertial systems for rocket-propelled missiles has apparently had little discussion. In such missiles, great altitudes may be reached at a rapid rate, making necessary guidance systems which differ considerably from those for constant altitude use. Since most rocket-propelled missiles are weapons, details of specific inertial systems or the performance of the latest instruments are for the most part classified security information. However, the basic ideas and principles of inertial guidance form a rather simple and obvious application of classical mechanics, and are no more classified than are the principles of rocket propulsion or of radar. In this paper, these basic ideas are presented. The operation of typical inertial components is explained, together with some discussion of systems problems. For illustrative purposes, a simple guidance system is conceived for the V-2 rocket.

Inertial navigation is a form of navigation akin to "dead reckoning." The position, velocity, time and orientation of a missile are known at the start of a flight. Subsequent velocity and position is then obtained by measurements made solely within the missile. This fact eliminates all dependence upon clear weather for star-sighting or upon any form of electromagnetic radiation which is subject to interference or possibly to line of sight limitations. On the other hand, inertial navigation is subject to the disadvantage of dead reckoning, that is, the longer the duration of the flight, the greater are the navigation uncertainties.

Basic Elements

The basic principle is extremely simple. The missile acceleration relative to a known reference frame established by an initial orientation is measured inside the missile. This acceleration is then integrated to give velocity and position. A guidance or steering function may be added to the navigation or position determination function by comparing present velocity and position with stored values defining the desired flight. After suitable computation, steering and thrust signals can be sent to the missile control system. The basic conceptual elements of all inertial systems can be identified as an attitude reference, an accelerometer, a clock, a computer, and a memory.

The attitude reference is a device which is oriented at the start of the flight and then maintains or remembers this orientation. In effect, it remembers "which way is up," and which way is North. Philosophically, there are many ways that this can be done, but most practical schemes employ gyroscopes physically mounted on a stable platform. Most accelerometers are single-degree-of-freedom instruments, that is, they are only sensitive to one component of acceleration. For rocket-propelled missiles, accelerations may be large in all three space coordinates and, in general, three accelerometers, one for each coordinate axis, must be used. For submarine, ship or aircraft in essentially constant altitude flight, the accelerometers are usually oriented in the local horizontal plane and only two are required, the vertical component being monitored by an altimeter. The computer and clock are needed for the process of integration to obtain velocity and position, for computation of gravity, for calculation of the earth's rotation and for computation of steering commands. The memory unit stores the vehicle's prescribed path or destination. These five basic elements are conceptually distinct but each element is not usually a separate piece of hardware. For instance, accelerometers may perform integration and contain the memory in addition to measuring acceleration.

Associated with the inertial guidance system is equipment at the missile launch point which is used to orient the attitude reference, to establish initial conditions and to store information in the memory unit. Closely related to the inertial system, but by definition excluded from it conceptually, is the vehicle control system which physically steers and stabilizes the missile, and speeds it up or slows it down.

In the traditional form of shipboard navigation, the attitude reference is given by the position of the sun, moon and stars. The accelerometer becomes a bubble level or the horizon. The clock is a chronometer. The computer is an almanac and a pencil and paper. The memory is written in ship's orders or contained in the brain of the captain. The control system is the wheel and rudder and the throttles on the engines.

Gyroscopes

The heart of an inertial guidance system is the set of gyroscopes and accelerometers. It is only because of recent major improvements in the precision of these instruments that in ertial guidance has become feasible. A leading group in this field is the Instrumentation Laboratory of the Massachusetts Institute of Technology, directed by Dr. C. S. Draper. In particular, he developed the type of single-degree-of-freedom gyroscopes known as HIG gyros (Hermetic Integrating Gyros). Other types of gyros (6) can be used for inertial systems, but precision HIG types are available commercially and therefore will be described and used as examples here. A detailed description with many references is given in (7).

Fig. 1 is a schematic drawing of the HIG type, single-

[1] Presented at the ARS Semi-Annual Meeting, San Francisco, Calif., June 10–13, 1957.

[2] Manager, Inertial Guidance Dept., Space Technology Laboratories.

[3] Numbers in parentheses indicate References at end of paper.

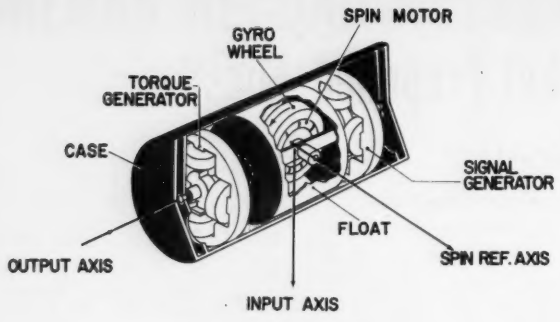

Fig. 1 HIG gyroscope

degree-of-freedom gyroscope originally developed by the Instrumentation Laboratory, MIT. Various commercial versions differ in mechanical detail and in type of signal generator and torque generator. Basically, the gyro consists of a spinning wheel driven by an electric motor, mounted on preloaded ball bearings and contained in a hermetically sealed can or float with shaft extensions. The float is completely submerged in a viscous fluid which has the same average density as the float and shaft. In other words, the float is in neutral buoyancy and no radial forces are carried by the jeweled pivots at either end of the shaft. This serves to reduce friction about the axis defined by the pivots to a negligible value and makes the instrument a rugged design. Coaxial with the shaft is a signal generator which gives a voltage proportional to the angular displacement of the float relative to the case, and a torque generator which can be used to apply torque to the float. Means may be provided for temperature control, for balancing the float and for conducting power to the spin motor.

The basic principle of operation of the gyro can be explained in terms of the three axes shown in Fig. 1. The spin reference axis lies along the angular momentum vector (spin axis) of the wheel when the signal generator output is zero. The output axis is normal to the spin reference axis, and is the axis about which the float is free to turn. The input axis is normal to the output axis and spin reference axis. The input quantity to the instrument is an angular motion of the case, *relative to inertial space*, about the input axis. The resulting output is a movement of the float *relative to the case* which results in a voltage from the signal generator. The operation is explained by the familiar physical fact that when a torque is applied to a spinning wheel so as to change the direction of its spin axis, the spin axis tends to align itself with the torque vector. Conversely, when the axis of a spinning wheel is forcibly precessed or rotated, the wheel through its bearings exerts a torque about an axis perpendicular to the axis of forced rotation. In the HIG gyro, movement of the case about the input axis causes a forced precession of the gyro wheel about this axis. The gyro wheel thus exerts a torque on the float about the output axis. Initially, this torque accelerates the float, but as the float gains angular velocity, the viscous shear torque reduces the acceleration to zero and the float reaches a steady angular velocity. The gyro torque is then balanced by the viscous shear torque and the output angular rate is proportional to the input angular rate.

$$B\omega_o = H\omega_i$$

where

ω_o = output angular rate
ω_i = input angular rate
B = fluid shear coefficient
H = angular momentum

and for small angles

$$\theta_o = \frac{H}{B}\int \omega_i dt = \frac{H}{B}\theta_i$$

The fact that the output signal is proportional to the integral of the input angular rate is the source of the term "integrating gyro." The gyro thus serves as an attitude reference. Once the wheel is spinning, and provided no signals are applied to the torque generator, an angular movement about the input axis results in an output signal. Over its operating range, the instrument is linear, so that a reverse movement about the input axis returns the output signal to a null.

Torques other than the gyroscopic element, viscous drag and float inertia torques can act about the output axis. They may arise from two sources, intentionally applied through the torque generator, and unintentionally applied by various disturbances. These torques result in output signals which are indistinguishable from those caused by input angular rates. They therefore act to change the reference orientation of the gyro at a rate proportional to the torque. If the torques are uncertainties caused by such things as float unbalance, signal generator reaction, fluid convection currents, etc., the resulting output signal looks like an input angular rate which is called the drift rate of the gyro. This drift rate is the basic performance figure of merit for inertial navigational use. The lower the drift rate, the better the attitude reference is maintained, and the more accurate the guidance system can be.

HIG gyros act as precision angular motion sensors, rather than sources of torques to overcome friction or unbalances. Normally, they have an operating range of only a few degrees and to prevent various cross coupling errors, input angles should be kept small. Therefore, for inertial guidance use, gyros are usually mounted on a platform or base which is servo-driven to maintain the gyro output at or near a null. The platform thus remains fixed in orientation relative to inertial space, or is rotated at a rate determined by torque generator input.

Accelerometers

The accelerometer is probably the most critical instrument, in so far as accuracy is concerned, for inertial guidance systems for rocket-propelled missiles. This is in contrast to the constant altitude case in which the gyros are usually the most critical item. For applications considered here, the accelerometers must work over a wide dynamic range with great precision and usually in the presence of severe environments. Fig. 2 is a schematic of a class of accelerometers suitable for inertial systems (8).

The instrument operates by applying force to a mass inside the instrument case so that the mass moves with the case. The mass is termed the seismic or proof mass and

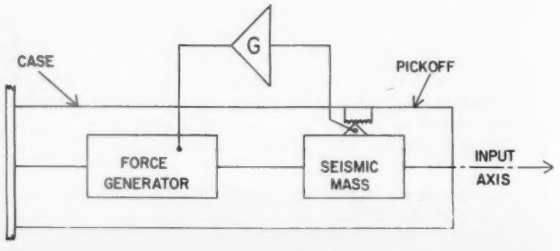

Fig. 2 Basic accelerometer

except for instrument dynamics, its acceleration is equal to the acceleration of the case. The force which is needed to accelerate or move the seismic mass is measured in terms of some physical quantity which is proportional to the force. For instance, if the force generator is a simple spring, the force is measured by the deflection of the spring. A common force generator is obtained by applying current to a coil in a magnetic field. As shown in the figure, the current is obtained by feedback from a pickoff between the seismic mass and the case. The basic equation for the instrument is

$$a_m = \frac{F}{M} + g$$

where

a_m = acceleration of seismic mass along input axis relative to inertial space
F = all nongravitational forces acting on seismic mass along input axis
M = mass of seismic mass
g = component of gravity along input axis

This equation clearly shows that an accelerometer does not measure acceleration itself, but rather the difference between acceleration and gravity. This difference which is equal to the quantity F/M has been called thrust acceleration a_t. This nomenclature stems from the fact that F/M for the accelerometer is equal to the corresponding quantity for the complete missile, that is, to the sum of the nongravitational forces acting on the missile, divided by the instantaneous mass of the missile. Most of the nongravitational force acting on a rocket-propelled missile is thrust, hence, the term, thrust acceleration. To obtain acceleration itself, gravity, which depends upon position, must be calculated in the computer and added to thrust acceleration. It should be noted that when the acceleration itself is accurately known, as it is on the earth's surface, a calibrated special accelerometer can be used to measure gravity, or conversely, gravity can be used to calibrate an accelerometer. It is sometimes convenient to take the viewpoint that an accelerometer measures acceleration relative to a freely falling coordinate frame, that is, to a frame accelerating at the value of g existing at the instrument. It is important, of course, that all the forces acting on the mass along the input axis be measured, and that only these forces be measured. An example of the former type is friction between the seismic mass and the case. An example of the latter is change in geometry caused by distortion so that the instrument becomes sensitive to cross acceleration. The above discussion assumes that the accelerometer is not rotating. If rotation is present, various correction terms must be included.

Fig. 3 is a schematic of a practical type of instrument based on the HIG gyro construction. The seismic mass exists in the

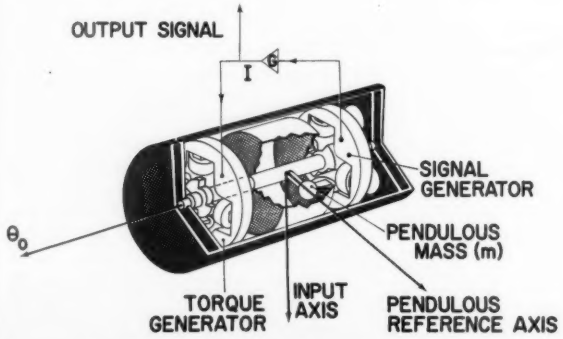

Fig. 3 Constrained pendulum accelerometer

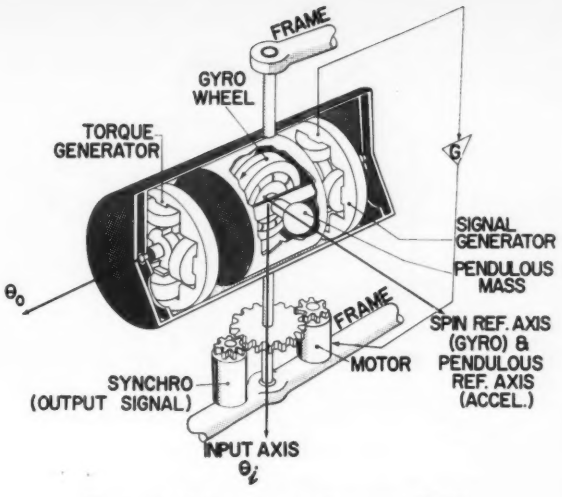

Fig. 4 Pendulous gyro accelerometer (PGA)

form of a pendulum and the force generator is the torque generator. The pickoff is the signal generator. Flotation virtually eliminates uncertainty friction torques at the pivots. Because of the pendulous mass, acceleration of the instrument along the input axis creates a torque about the float pivot axis. This torque causes rotation of the float and a consequent signal generator voltage proportional to θ_o. This voltage is used to generate a current which is applied to the torque generator to give a torque which "constrains" the pendulum and keeps θ_o small. The current, I, is thus proportional to acceleration along the input axis. The gain of the feedback system must be kept quite high so that deflection of the pendulum under high input acceleration is small. Otherwise, a "cross talk" torque is developed which is proportional to the product of the acceleration along the pendulous reference axis and the sine of the deflection angle θ_o. Instruments of this type, called force feedback pendulums or constrained pendulums, are available commercially. They are made with a wide variety of dynamic range and frequency response.

Velocity and position are the quantities of interest in navigation, rather than acceleration. Increased accuracy and reliability may sometimes be obtained by performing integration in the accelerometer. Basically, this is done by making the force acting on the seismic mass proportional to a rate of some kind. For instance, the current fed to the torque generator in Fig. 3 might be applied in pulses of constant area but variable rate. Pulse rate is then proportional to acceleration and total number of pulses to velocity. Another useful device and one used by the Germans in the V-2 is the pendulous gyro accelerometer (PGA). This instrument is a pendulum in which the force generator is a gyroscopic element. Fig. 4 is a schematic of such an instrument based on the HIG gyro construction. The output of the signal generator is fed to the servo motor which rotates the gyro case about the input axis at a rate such that the torque developed by the gyro element just equals the pendulous torque. Omitting dynamics, the torque balance about the float axis is

$$H\dot{\theta}_i = mla$$

where

ml = pendulosity
a = acceleration along input axis

hence

$$\theta_i = \frac{ml}{H}\int a\,dt = \frac{ml}{H}v$$

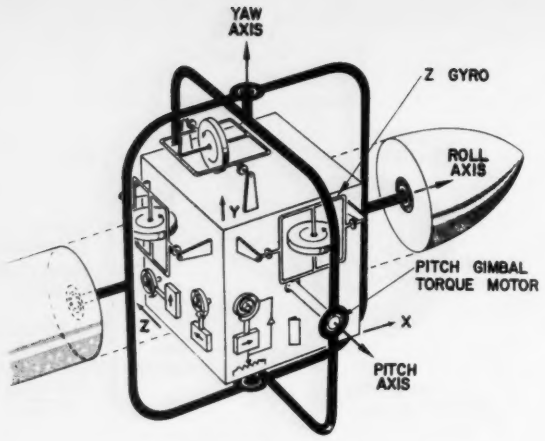

Fig. 5 Stabilized platform

The angular rate of the gyro case is thus proportional to acceleration and the total angle turned by the gyro case is proportional to velocity. As with the instrument of Fig. 3, the gain of the feedback loop must be kept high so that θ_o is very small. The torque generator of the gyro can be used to apply additional torques to the gyro float which add to the pendulous torque. In this way, gravity may be added to the thrust acceleration to give true acceleration and velocity.

System Mechanization

The two basic instruments of inertial guidance systems have been briefly described; namely, gyros to maintain an attitude reference and accelerometers to measure thrust acceleration. These instruments must be related so that the accelerometer orientation relative to the attitude reference is known. A practical method for doing this consists of mounting three gyros on a frame so that their input axes are orthogonal (9). This frame, usually called a stable platform, is mounted in a gimbal structure attached to the vehicle. The gimbal structure serves as a ball and socket joint and allows the vehicle to rotate in any way about the platform. Output signals from the gyros are fed to torque motors on the gimbal axes which serve to overcome gimbal bearing friction and keep the gyro outputs at, or close to, a null value. In doing so, the platform upon which the gyros are mounted maintains its orientation relative to inertial space irrespective of vehicle attitude. Three single-degree-of-freedom accelerometers can be mounted on the platform with their input axes orthogonal but not necessarily parallel to the gyro axes. The accelerometers are thus nonrotating and their input axes define the coordinate system fixed in the attitude reference frame.

For full angular freedom, four gimbals are required and slip rings on the gimbal axes are usually necessary to carry the various signal and power leads. For vehicles, such as the V-2 rocket, which have limited angular motions, three gimbals are sufficient and flexible cabling from the vehicle to the stable platform can be used.

A schematic drawing of a gimbal system with gyros and accelerometers (sometimes called an inertial measurement unit—IMU) is shown in Fig. 5. Any small angular motion of the platform relative to inertial space is sensed by the set of gyros. The gyro output signals are used to generate currents which are applied to torque motors mounted at the gimbal bearings. These rotate the gimbals and platform so as to return the platform gyros to a null position. In the figure, the output of the z axis gyro is always applied to the pitch axis gimbal torque motor. For pitch angles other than that shown in the figure, the x and y axes are not parallel to the gimbal yaw and gimbal roll axes. Therefore, the x and y gyro signals must be resolved through a synchro resolver on the gimbal pitch axis to give proper signals to the yaw and roll gimbal torque motors. There is room for much mechanical ingenuity in the design of gimbals and stable platforms to achieve minimum weight and size and maximum stiffness and environmental protection.

Some means must be provided for orienting the platform at the start of a flight. One possible way is simply to set the three gimbal angles to the required value. This then orients the platform relative to the missile frame. Another more accurate way employs the navigation accelerometers or two separate pendulums to position the platform relative to the launch point horizontal. Accurate azimuth orientation can be done by optically sighting on a mirror mounted on the platform from a theodolite external to the missile.

Computers for inertial guidance systems can be either digital or analog. The former, of course, can be made as accurate as desired at the expense of added weight and complexity. The choice of type of computer and method of computer mechanization depends upon over-all system characteristics such as range, accuracy and rocket thrust characteristics; upon the computing task to be done (called the guidance scheme); and upon available computer hardware. Much can be done in making approximations and in combining computing functions to minimize weight and errors and to maximize reliability and flexibility.

Guidance Schemes

Rather than discuss the broad subject of guidance schemes in general terms, a specific example will be considered. Fig. 6 shows a trajectory for the V-2 missile which is based upon data given in (10).

Fig. 7 details the trajectory during the powered portion of the flight. The missile, under standard conditions, burns for 70 sec and achieves a velocity of 5860 fps. It then follows a ballistic or free-fall path until it impacts on the earth at about 230 miles range. For simplicity in making the calculations, it is assumed that the earth is flat and the gravity field constant. Vertical flight of the rocket lasts 8.5 sec at which time it is assumed the rocket instantaneously acquires an attitude of 10 deg from the vertical. From this time until motor shutoff, the missile follows a gravity turn, i.e., the missile is steered so that the thrust vector is parallel to the velocity vector. In making the calculations the aerodynamic forces were neglected; in any case, they are very small compared to thrust and gravity.

There are many ways in which this missile could be guided to impact at its intended target. The simplest scheme consists of aiming the missile at the target and firing it as a gun is fired. Guidance is then done only while the missile is constrained by the launcher. A scheme which is closer to the usual meaning of the word, guidance, consists of installing a programmer in the missile which generates a missile atti-

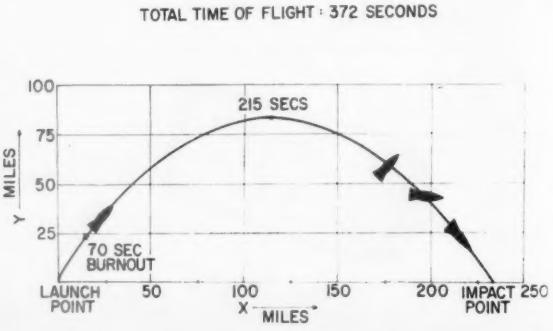

Fig. 6 V-2 trajectory

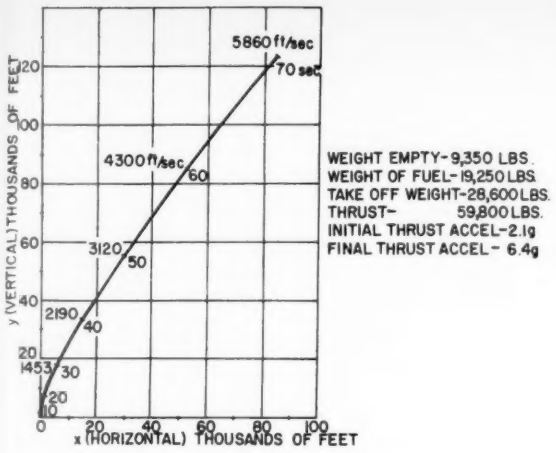

Fig. 7 V-2 powered flight trajectory

tude angle as a function of time. This command signal is then compared with the actual missile attitude as measured by the pitch gimbal angle of an inertial platform such as that shown in Fig. 5. The difference between the command angle and the actual angle is then used as an input to the missile control system to steer the missile in pitch. Yaw and roll angles are similarly held to programmed values which are usually zero. A clock could be used to shut the rocket engine off at 70 sec or, alternatively, enough fuel could be placed in the missile so that it would burn out at 70 sec. This scheme is essentially an extension of the previous one in that the launcher or gun barrel is greatly lengthened. While simple, guidance probably would not be accurate because of uncertainties in missile parameters. For instance, if the rocket engine thrust was, say 10 per cent more than the preplanned or standard value, the missile would accelerate more rapidly than standard and the velocity at 70 sec would be much greater than standard. Furthermore, the missile would be closer to the target than standard at motor shutoff. These effects would cause an impact far beyond the target. Conversely, a rocket engine thrust less than standard would result in an impact short of the target. Other nonstandard flight parameters, such as winds, would also cause target miss.

The guidance scheme actually used by the Germans in the V-2 (11) had an important refinement over the simple scheme just described. A single integrating accelerometer was mounted with its input axis along the missile longitudinal axis, and the motor was shut off when the accelerometer output (thrust velocity) equaled the preset value. For the example shown in Figs. 6 and 7, this would be 5860 fps plus the time integral of the gravity component along the trajectory. The V-2 guidance system essentially measured only one component of velocity. With such a scheme, it is possible to have considerable target miss because the other two components of velocity at motor shutoff may be nonstandard. A further improvement in guidance can be made by using a stable platform and three accelerometers similar to that shown in Fig. 5. In this case, all three components of velocity are obtained.

The guidance schemes just discussed are all of the type which might be labeled gun barrel guidance. They all guide the missile during powered flight and terminate rocket thrust so that the missile follows a ballistic path to the target. After motor shutoff, the only nongravitational forces acting on the missile are aerodynamic. These can be calculated prior to flight for standard conditions and their effects included in the instructions placed in the system memory. Some target miss will be caused by such uncertainties as winds acting on the missile after motor shutoff. The inertial system could be used to measure and correct for these uncertainties, but they might be smaller than the inertial instrument errors. Of course, in this case, guidance after motor shutoff would be a mistake. If no atmosphere whatsoever existed, the missile would be in a free-fall state after motor shutoff and the accelerometers would have zero output. The airborne computer would calculate gravity, velocity and position, based only on the initial values existing at the time of motor shutoff.

For a nonrotating, spherical earth, the missile trajectory lies in a plane. The actual earth does not have a perfectly spherical gravitational field but the variations are negligible for a missile such as our example and will not be considered further here. For inertial guidance applications, it is convenient to visualize trajectories in terms of inertial or nonrotating coordinates. From this viewpoint, the target and launch point are moving eastward over the surface of the earth with a velocity

$$V_e = \omega_e R \cos \lambda$$

where R is the earth's radius, ω_e is earth angular rate and λ is the latitude angle. The missile at launch then has an initial horizontal velocity due to the motion of the launch point. If the launch point and target both lie on the equator, the trajectory will lie in the equatorial plane. If the missile is fired over an earth's pole, the target is moving normal to the trajectory plane and hence the missile must be "aimed" at the location of the target at the predicted time of impact. Furthermore, the missile initial velocity is normal to the trajectory plane. Therefore, the missile must be aimed slightly to the West of the free-fall trajectory plane so that the velocity vector at motor shutoff will be in the trajectory plane. Intermediate latitudes and azimuths, of course, have both lateral and range effects from the earth's rotation.

Gravity

If every missile flight were exactly standard or as precalculated, there would be no reason to calculate gravity during the flight. Instead, the effect of gravity could be precalculated and guidance could be done in terms of thrust acceleration alone. However, nonstandard trajectories will result in gravity accelerations different from standard. To account for this, either the actual value of gravity can be calculated in flight or some correction to the standard preplanned value can be made. The manner in which gravity is handled depends upon the range, accuracy desired, trajectory used, and the method of mechanization.

The components of gravity are a nonlinear function of position, and are somewhat difficult to calculate exactly (12–14). Therefore, if possible, some approximation should be used. Of course, the simplest approximation considers gravity a constant in direction and magnitude. A step more sophisticated is to assume a linear variation of gravity with displacement from some reference point. Consider, for example, a nonrotating coordinate system with origin near the midpoint of the powered flight trajectory, with y axis vertical and with x axis in the trajectory plane. Then linear approximations to the gravity components are

$$g_y \approx -\frac{g_0 R_0^2}{(R_0 + y)^2} \approx -\left[g_0 - \frac{2g_0}{R_0} y\right]$$

where R_0 is the distance from the earth's center to the origin and g_0 is the magnitude of gravity at the origin.

$$g_x \approx -\frac{g_0}{R_0} x$$

These are the first order terms of a Taylor's series representation of the gravity components. Higher order terms could be included if necessary.

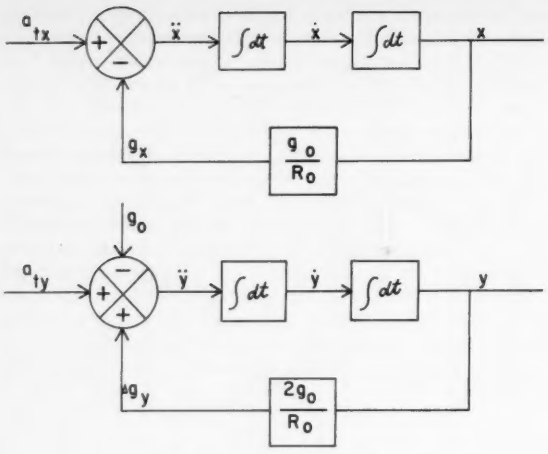

Fig. 8 Gravity computer

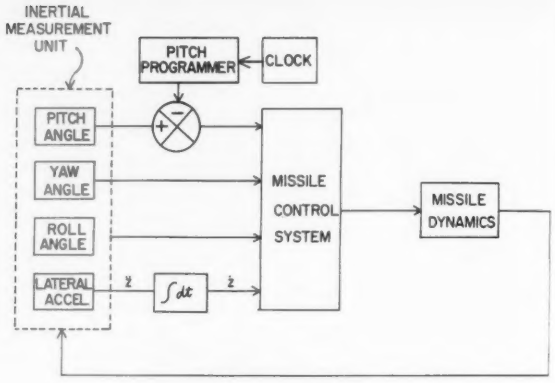

Fig. 9 Steering computer

As stated earlier, the basic vector acceleration equation in coordinate form is

$a_x = a_{tx} + g_x$ $\quad a_i$ = acceleration
$a_y = a_{ty} + g_y$ $\quad a_{ti}$ = thrust acceleration
$a_z = a_{tz} + g_z$ $\quad g_i$ = gravity

Block diagrams for the computation of acceleration assuming linear gravity terms are shown in Fig. 8. No computation for z or lateral direction need be made for a missile such as our example of Fig. 6 because no appreciable z position coordinate develops, i.e., g_z can be considered a constant.

Improved System

The improved V-2 guidance system mentioned earlier will now be considered in more detail for the trajectory of Figs. 6 and 7. For simplicity in explanation, it will be assumed that the earth is spherical and nonrotating. A complete inertial measurement unit as shown in Fig. 5 will be used. The platform and the missile are oriented at the launch point so that the platform z axis is normal to the trajectory plane, the y axis is vertical, and the x axis is horizontal and lies in the trajectory plane. The trajectory plane itself passes through the earth's center, the launch point and the target. Except for gyro drift, the platform will maintain its initial orientation during flight. The missile is roll-stabilized so that the missile pitch axis is parallel to the platform z or pitch axis. By means of a programmer, the missile pitch attitude will be made a function of time. This is identical to the system actually used in the V-2. Any movement of the missile out of the trajectory plane caused by winds or thrust misalignment will give a signal from the z or lateral accelerometer. This signal will be integrated and sent to the missile control system which will steer the missile so that the lateral velocity remains essentially zero. A block diagram showing the essentials of this simple steering scheme is given in Fig. 9. In practice, provision for adequate dynamic stability and response are necessary.

The problem now remains as to how to obtain a motor shutoff signal so that the miss at the target in the plane of the trajectory, called the range miss, M_r, will be zero. What is done is to precalculate the effect on target miss of small displacements in the missile burnout position and velocity from the standard values. The total miss is then the sum of the separate effects. In other words

$$M_r = C_x\Delta x + C_y\Delta y + C_{\dot{x}}\Delta\dot{x} + C_{\dot{y}}\Delta\dot{y}$$

where the C's are constants and the Δ quantities are the difference between the actual and standard values. The above equation is simply the linear approximation to a Taylor's series expansion of range as a function of position and velocity about the standard motor shutoff point.

$$R - R_s = M_r = \frac{\partial R}{\partial x}(x - x_s) + \frac{\partial R}{\partial y}(y - y_s) + \frac{\partial R}{\partial \dot{x}}(\dot{x} - \dot{x}_s) + \frac{\partial R}{\partial \dot{y}}(\dot{y} - \dot{y}_s) + \ldots$$

where R designates range, the s subscript designates standard conditions and the derivatives are evaluated at the standard shutoff point. For the example of Figs. 6 and 7, the values of the coefficient are

$C_x = 1\ \frac{\text{ft}}{\text{ft}}$ $\quad C_{\dot{x}} = 300\ \frac{\text{ft}}{\text{fps}}$
$C_y = 0.7\ \frac{\text{ft}}{\text{ft}}$ $\quad C_{\dot{y}} = 220\ \frac{\text{ft}}{\text{fps}}$

This means, for example, that if the x component of velocity is 1 fps greater than standard, then the range will be 300 ft greater than standard.

A block diagram of a computer which continuously calculates target miss is shown in Fig. 10. The rocket motor thrust is terminated when the value of miss, M_r, becomes zero.

Note that gravity computers similar to Fig. 8 are included. The location of the target is defined by the initial values, x_s, y_s, $\dot{x}_s$, $\dot{y}_s$ and by the values of the C's. These values are constants which are set into the computer prior to launch.

The actual nonstandard missile will have motor shutoff at a point near the standard point. For instance, if thrust is low, the missile position and velocity will not be as high as standard at a given pitch angle (because pitch attitude angle depends upon time only). The missile trajectory will therefore lie below the standard trajectory and motor shutoff will probably occur at a greater x value than standard. The actual trajectory and shutoff point can, of course, be calculated in the same manner as was done for the standard case.

System Errors

The magnitude of target miss due to various approximations and instrument errors can be calculated quite easily, at least in principle. The two principal approximations in our example are found in linearizing the gravity computation, and in linearizing the calculation of target miss. Errors due to these sources will be very small provided that the rocket

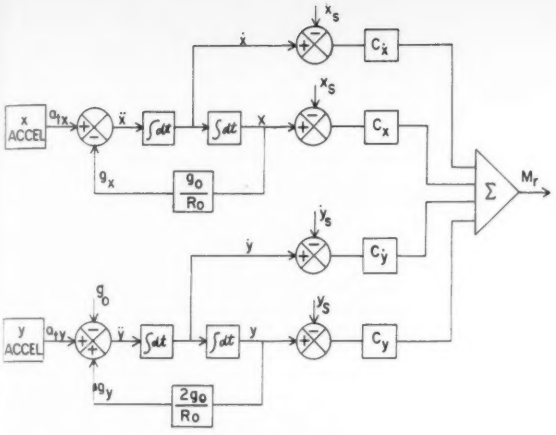

Fig. 10 Motor shutoff computer

thrust and pitch program are reasonably close to standard values. In fact, it is quite possible that the gravity computation itself could be eliminated.

To consider the effects of accelerometer errors and gyro drifts, an important characteristic of the basic acceleration equation must first be explored. A coordinate system identical to that used for Fig. 8 will be considered. The acceleration equations are then

$$\ddot{x} = a_{tx} + g_x$$

where $\ddot{x}$, $\ddot{y}$ are alternate symbols for a_x and a_y

$$\ddot{y} = a_{ty} + g_y$$

Now a small change or perturbation in the value of $\ddot{x}$ is equal to a perturbation or error in the value of thrust acceleration plus an error in the computed value of gravity. The gravity error is composed of any computer mechanization errors and error due to using an erroneous position in calculating gravity. In what follows, only the latter will be considered. We thus have

$$\Delta\ddot{x} = \Delta a_{tx} + \Delta g_x$$

$$\Delta\ddot{y} = \Delta a_{ty} + \Delta g_y$$

By taking a differential of the gravity expression, we obtain expressions for the dependence of gravity error on position error.

$$\Delta g_x = -\frac{g_0}{R_0}\Delta x$$

$$\Delta g_y = +\frac{2g_0}{R_0}\Delta y$$

Substituting these expressions into the above leads to the differential equations

$$\Delta\ddot{x} + \frac{g_0}{R_0}\Delta x = \Delta a_{tx}$$

$$\Delta\ddot{y} - \frac{2g_0}{R_0}\Delta y = \Delta a_{ty}$$

The solutions for constant values of thrust acceleration errors (or perturbations) are

$$\Delta x = \frac{\Delta a_{tx}}{g_0/R_0}\left[1 - \cos\sqrt{\frac{g_0}{R_0}}\,t\right]$$

$$\Delta y = \frac{\Delta a_{ty}}{2g_0/R_0}\left[\cosh\sqrt{\frac{2g_0}{R_0}}\,t - 1\right]$$

For positions near the surface of the earth, the numerical value of $\sqrt{R_0/g_0}$ is about 84 min.

These linearized error equations illustrate a basic limitation of pure inertial guidance for long times of flight. That is, errors in the vertical direction increase exponentially with time. Errors in the horizontal direction, however, are oscillatory. This is one reason that inertial systems for aircraft and ships employ altimeters to measure altitude. For powered flight duration of a few minutes, such as that for our example, the equations can be closely approximated by the simple expressions.

$$\Delta x = \Delta a_{tx}\frac{t^2}{2} \qquad \Delta\dot{x} = \Delta a_{tx}t$$

$$\Delta y = \Delta a_{ty}\frac{t^2}{2} \qquad \Delta\dot{y} = \Delta a_{ty}t$$

which are those that would be obtained by ignoring the feedback error from the gravity calculation.

For our example, the x accelerometer, for instance, must have a dynamic range of about 0 to 6 g's (see Fig. 7). A zero offset in this accelerometer of 0.006 g's (0.1%) will produce a velocity error at motor shutoff of about $\Delta\dot{x}$ = (0.006) (32.2) (70) = 13.5 fps. The miss coefficient for $\dot{x}$ was 300 ft target miss per fps variation in x velocity. Hence, the range miss at the target caused by this accelerometer error would be about 4000 ft. The accelerometer error would also cause position error of about 500 ft [$\Delta x = \Delta a_{tx}(t^2/2)$] so that the total miss would be about 4500 ft. If the z accelerometer had a similar zero offset error, the missile would have a lateral velocity error of 13.5 fps at motor shutoff. This would cause a lateral miss of about (13.5 fps) (300 sec) = 4050 ft. In a similar manner, the effects of accelerometer scale factor errors or of integrator errors can be evaluated.

The effect of gyro drift about the pitch axis can be calculated by expressing accelerometer error as a function of attitude reference error. However, gyro drift in the azimuth direction is probably more critical than in the pitch or roll direction. In the azimuth case for instance, a constant gyro drift rate of 0.3 deg/hr would result in about 1 milliradian platform azimuth misalignment at the end of 70 sec of flight. This would cause the missile velocity vector (actual trajectory plane) to point somewhat less than 1 milliradian away from the standard trajectory plane. As an upper bound, this drift could be considered as occurring at the start of flight, i.e., as an initial misalignment of the trajectory plane. It would then lead to a target miss of about (0.001 radian) (230 miles) (5280 ft/mile) = 1300 ft.

It is apparent that to achieve good accuracy, precision components are needed. It is indicative of the state of the art that components with performance better than the hypothetical values assumed here are advertised commercially. Even making allowance for all the other errors in a guidance system, it would appear that these commercial components would give an accuracy better than was obtained by the German V-2 missile of World War II.

References

1 Wrigley, Walter, Woodbury, Roger B. and Hovorka, John,

"Inertial Guidance," Institute of Aeronautical Sciences, IAS Preprint 698, presented Jan. 31, 1957.

2 Slater, J. M. and Duncan, D. B., "Inertial Navigation," *Aeronautical Engineering Review*, Vol. 15, No. 1, Jan. 1956.

3 Klass, Philip J., "Inertial Guidance," *Aviation Week* Special Report, Vol. 64, Nos. 1–4, Copyright 1956.

4 Adams, D. E., "Introduction to Inertial Navigation," *The Journal*, The Institute of Navigation, Vol. IX, No. 3, July 1956.

5 Slater, J. M., "Choice of Coordinate Systems in Inertial Navigation," *Navigation*, Vol. 5, No. 2, June 1956, pp. 58–62.

6 Sommer, A. V., "Missile Guidance. . .Why So Little Progress," *Aviation Age*, Aug. 1954.

Statsinger, Joseph, " 'Absolute' Guidance for Airborne Vehicles," *Aviation Age*, Sept. 1954.

Bishop, R. L., "Inertial System Components Are Here," *Aviation Age*, Oct. 1954.

Litman, Dr. Bernard, "Computers—Brains of the Inertial System," *Aviation Age*, Nov. 1954.

Davenport, C. T., "Dependable Inertial Guidance Systems Can Be Produced," *Aviation Age*, Jan. 1955.

7 Draper, C. S., Wrigley, W. and Grohe, L. R., "The Floating Integrating Gyro and Its Application to Geometrical Stabilization Problems on Moving Bases," Institute of the Aeronautical Sciences, IAS Preprint 503, presented Jan. 25, 1955.

8 Slater, J. M., "Measurement and Integration of Acceleration in Inertial Navigation," The American Society of Mechanical Engineers, Paper 56-A-160, presented Nov. 25–30, 1956.

9 Draper, C. S. and Woodbury, R. B., "Geometrical Stabilization Based on Servo-Driven Gimbals and Integrating Gyro Units," MIT, presented at AGARD Symposium on Guidance and Control, Venice, Italy, Sept. 24–28, 1956.

10 Ley, Willy, "Rockets, Missiles, and Space Travel," New York: Viking Press, 1951.

11 Kooy, J. M. J. and Uytendogaart, J. W. H., "Ballistics of the Future," New York: McGraw-Hill, 1946.

12 Gilvarry, John J., "Einstein's Equivalence Principle and the Problem of Blind Navigation," *Physical Review*, Vol. 73, 1948. Second Series, pp. 1409–1410.

13 Gilvarry, J. J., Browne, S. H., and Williams, I. K., "Theory of Blind Navigation by Dynamical Measurements," *Journal of Applied Physics*, Vol. 21, Aug. 1950, pp. 753–761.

14 Browne, S. H. and Gilvarry, J. J., "Theory of Errors in Automatic Navigation with Integrating Accelerometer Systems," *U. S. Air Force Project RAND*, R-154, May 5, 1952, The Rand Corp.

A Deceleration Probe for Measuring Stagnation Pressure and Velocity of a Particle-Laden Gas Stream[1]

JULES L. DUSSOURD[2]

AiResearch Manufacturing Co., Phoenix, Ariz.

and

ASCHER H. SHAPIRO[3]

Massachusetts Institute of Technology, Cambridge, Mass.

The measurement of the stagnation pressure and, from this, the velocity of the gas phase, in a stream of gas laden with liquid droplets or solid particles is investigated theoretically and experimentally. The three requirements of a successful design are as follows: (i) To prevent flooding of the probe and pressure lines with particles, the rear of the probe must be vented by an orifice of appropriate size. Moreover, pressurized manometers with a special operating technique must be employed. (ii) To minimize the effects of aerodynamic interactions outside the probe, the latter must be made sufficiently small. (iii) To minimize the effects of aerodynamic interactions within the probe, the internal pressure tap must be situated close to the nose of the probe. The phenomena associated with the momentum interchanges between gas and particles are analyzed, and quantitative evaluation is made of the associated error recorded by a total pressure probe. For convenience in design the magnitude of the error is presented graphically in terms of the probe dimensions and the properties of the gas and particle flows. The theoretical findings are checked by the testing of a series of experimental probes of varying geometry in an air stream carrying water droplets. Satisfactory agreement exists between theory and experiment. It is shown that a practical probe can be built to give a negligible error in the measurement of stagnation pressure in the range of variables investigated. Further it is found possible, with simple modifications, to adapt the experimental probe conveniently to the local measurement of other stream properties, namely, the mass rate of flow per unit area of particles, the particle size, and the particle velocity.

Received June 17, 1957.

[1] Based on a doctoral thesis (Ref. 5) submitted by Jules L. Dussourd to the Department of Mechanical Engineering, MIT. The work was supported in part under Contract N5ori-07878 with the Office of Naval Research.

[2] Formerly Research Assistant Department of Mechanical Engineering, MIT, Cambridge, Mass.

[3] Professor of Mechanical Engineering.

Nomenclature

A	=	cross-sectional area
c_D	=	drag coefficient of spherical particle, based on relative velocity
d	=	diameter of droplet
D	=	characteristic diameter of probe or tube
e	=	local collection efficiency: ratio of actual capture rate of particles to capture rate if trajectories were straight lines
i	=	$\sqrt{-1}$
K	=	ratio of average gas velocity inside probe to free stream velocity
m	=	droplet mass
M	=	Mach Number
p	=	static pressure
R	=	probe radius, $D/2$
Re_y	=	local Reynolds number of droplet in gas stream (Eq. 9b)

$Re_{f_0} = \rho_{a0} V_{w\infty} d/\mu_{a\infty}$
$Re_{f_\infty} = \rho_{a\infty} V_{w\infty} d/\mu_{a\infty}$
V = velocity
V_{ax} = component of gas velocity in x-direction
V_{ay} = component of gas velocity in y-direction
$V_{a\infty}$ = gas velocity at upstream infinity, assumed in x-direction
V_{wx} = component of water droplet velocity in x-direction
V_{wy} = component of water droplet velocity in y-direction
$V_{w\infty}$ = water droplet velocity at upstream infinity
w = mass rate of flow
x, y = Cartesian coordinates
x = distance measured downstream from probe inlet in axial direction
y = distance measured normal to axis of symmetry
μ = coefficient of dynamic viscosity
ρ = mass density

Subscripts

a = refers to gas
av = average value
meas = measured quantity
0 = true stagnation condition of gas phase
stag = stagnation point
stat = static
w = refers to particle flow
x = component parallel to x-direction
y = component parallel to y-direction
∞ = at upstream infinity

Introduction

IN SEVERAL fields of technology one encounters the problem of measuring the velocity and total pressure of an aerosol. This aerosol may consist of liquid droplets in a gas as in atomization and combustion problems, water injection, flow of wet stream, etc.; or it may consist of solid particles, as in smokes, pneumatic conveyors, dust separators; or mixtures of solid and liquid particles as found in connection with washing and scrubbing equipment.

This paper considers the case when the size of the particle is small compared with that of the measuring probe. It endeavors (1) to offer a solution to the practical difficulties associated with the physical presence of the particles in the stream such as probe plugging, and (2) to rationalize and evaluate, both theoretically and experimentally, the dynamic interaction taking place between the particles and the gaseous stream. The ultimate objective is to present a measuring probe of practical operation and capable of measuring the gas phase total pressure of the aerosol with a known degree of accuracy.

The experimental work was conducted with an air stream laden with small (i.e. in the range of 5 to 50 microns diam) water droplets. Accordingly, the particular case of water droplets will hereinafter be discussed. The solutions found, however, are also valid for small solid particles in a gas stream.

Preliminary Consideration of Problems of Probe Design

The use of an impact tube gives rise to two basic difficulties. Firstly, the instrument and the pressure transfer passages may rapidly become fouled with the accumulation of captured particles. Secondly, the measured reading will be influenced by the momentum interchanges between gas and particles both upstream of and within the instrument.

The Plugging Problem

Flooding of the probe may be circumvented by venting the interior through a suitably-proportioned purging orifice at the downstream end. Fig. 1 is typical of the arrangement. For water air mass-flow ratios up to 0.25, a smoothly tapered exit passage of throat area between three and five per cent of the

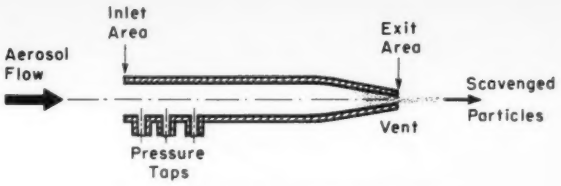

Fig. 1 Schematic of experimental probes

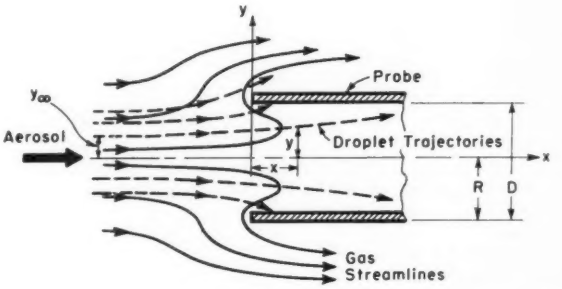

Fig. 2 Gas streamlines and droplet trajectories near probe mouth

inlet area was found to scavenge the captured water successfully and yet introduce a stagnation pressure error of 0.25 per cent, at most, of the free stream dynamic pressure. With the experimental arrangement shown, internal static pressures are recorded through wall taps.

Fouling of the pressure transfer lines is avoided by using pressurized manometers. The manometer pressure is initially held above the probe pressure and equilibrium is achieved by flow *from the manometer to the tube*, thus circumventing the entrance of water into the pressure transfer passages.

Dynamic Interacting External to the Probe

There exists in front of the probe a complex three-dimensional gas-flow field (Fig. 2). A droplet, by virtue of its comparatively great inertia, tends to continue in a straight-line trajectory with unchanged speed. Upon crossing the gas streamlines, however, the droplet is subject to a drag force (owing to the vector difference in velocities), and, to a lesser degree, to a buoyancy force (owing to the pressure gradient). Thus there are imposed on the droplet both a retarding force and a radially outward force. The droplet not only decelerates, but also migrates away from the axis, with the resulting trajectory lying between a straight line and the gas streamline (Fig. 2). The significant effects of these disturbances in the droplet motion are two in number:

First, because of the divergence of the trajectories, the *capture* or *collection* efficiency of the probe is less than one.

Second, any momentum change of the droplets as the latter traverse the gas streamlines must cause the gas pressure in the probe to be different from what it would have been if the gas had been decelerated without aerodynamic forces having been exerted on it by the droplets. Generally, the water loses momentum ahead of the probe, and this causes a rise in gas pressure over and above that which would occur if the particles were absent.

For fixed properties of the gas and particle flows, the dimensionless error (i.e., the *overpressure* ratio) depends only on the probe diameter D. Some insight into what is important in the probe design is gained by considering the two limiting cases of very small and very large probe diameters, respectively:

(a) When the probe is very small. ($D \rightarrow 0$), the extent of the

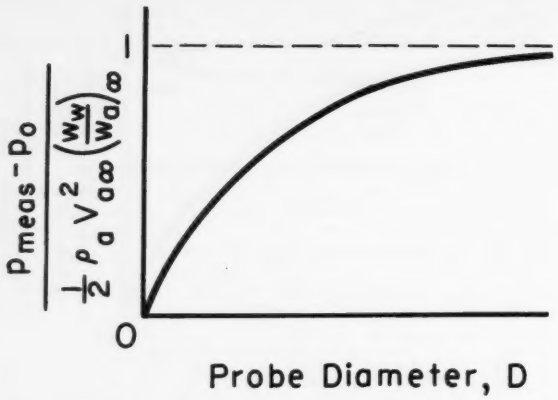

Fig. 3 Illustrates schematically the effect of probe diameter on error in measured stagnation pressure

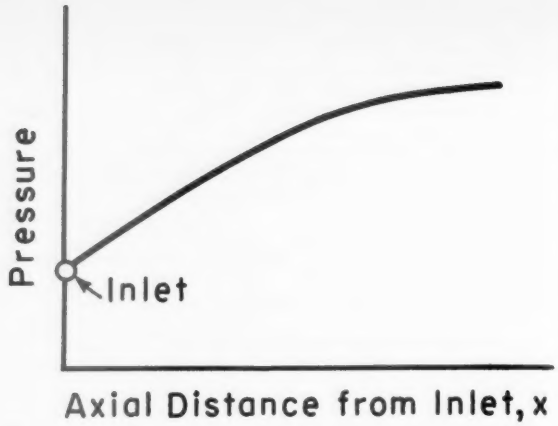

Fig. 4 Longitudinal pressure distribution inside probe (schematic)

probe disturbance field is correspondingly small. Therefore the droplets are exposed to aerodynamic forces for only a very short time; accordingly, they suffer only small changes in momentum; from momentum considerations, consequently, the gas pressure is then relatively unaffected by the droplets. Hence, as the probe becomes very small, the error in mouth pressure tends to vanish.

(b) When the probe is very large ($D \rightarrow \infty$), the size of the disturbance field is correspondingly large. Because of the long time during which aerodynamic forces can act on the droplets, the latter tend to follow closely the motion of the gas, and the capture efficiency tends toward zero. In the limit the gas-droplet mixture may then be thought of as a quasi-homogeneous fluid having the average density $\rho_{a\infty}[1 + (w_w/w_a)_\infty]$. Bernoulli's equation applied to the stagnation streamline of an incompressible flow then gives, for the case of very large probe diameter

$$p_{meas} - p_0 \rightarrow \frac{\rho_{a\infty} V_{a\infty}^2}{2} \left(\frac{w_w}{w_a}\right)_\infty \quad \ldots\ldots\ldots\ldots [1]$$

From the foregoing considerations it follows that the effect of probe size on probe error must be generally as portrayed in Fig. 3. Although one may conceive of interpreting the probe reading at either extreme of such a curve, in practice it seems easier to strive for a design in which the probe is so small that it reads the gas stagnation pressure directly, with negligible error. For design purposes, then the important question is, how small must the probe be (for specified free-stream properties) in order that the error may indeed be negligible?

Later it is shown that the overpressure curve of Fig. 3 depends not of course on D alone, but on two dimensionless groups (the Reynolds Number and Obedience Number) which involve as well the properties of the gas and particle flows.

Dynamic Interactions Within the Probe

After entering the probe, the droplets find themselves moving through relatively stagnant air, and they decelerate rapidly. Momentum considerations necessitate a concurrent rise in pressure in the gas (Fig. 4), with maximum pressure at the point where the velocity of the droplets is reduced to that of the gas. For this reason the pressure tap used for measuring stagnation pressure must be located as near the inlet as feasible, provided that gas stagnation conditions prevail at that point. How near this must be is analyzed quantitatively later.

A Practical Design for a Stagnation-Pressure Probe

Reviewing the requirements outlined previously, a successful design requires the following features:

(a) The captured liquid should be disposed of by some such means as a vent.

(b) The external dynamic interactions should be minimized by making the outside diameter small and by suitably designing the supporting shank and the shape of the inlet.

(c) The internal dynamic interactions should be minimized by placing the internal pressure tap very close to the inlet.

A practical design for meeting requirements (a) and (c) is illustrated in Fig. 5. The probe is self scavenging. Its inlet is smaller than the maximum diameter, thus tending to minimize external dynamic effects. The ring-shaped pressure pickup located near the inlet is protected against water intake by a small projecting lip. The outside diameter must of course be compatible with the requirements of accuracy. Such probes have been built and tested with excellent results (3).[4]

Theoretical Studies

We turn now to the quantitative analysis of the droplet motions in the neighborhood of the inlet of a test probe. A theoretical study of these events will indicate the orders of magnitude to be expected as well as the relative importance of the significant parameters.

Model for Theoretical Analysis

Exact calculation of the trajectory of a droplet is quite a formidable undertaking. It requires accurate knowledge of drop size distribution and shape; accurate knowledge of the viscous and compressibility effects on the gaseous velocity fields and on the interactions between gas and droplets. To make the theoretical problem manageable, we adopt rather an approximate but simple model which, it is believed, incorporates the leading physical phenomena. The assumptions are as follows:

(a) The gas flow is incompressible (Ref. 2 indicates that the effects of compressibility are small), non-viscous, and irrotational.

(b) The gas flow pattern is unaffected by the presence of the droplet.

(c) The droplets behave like solid spheres with no mutual interaction.

[4] Numbers in parentheses indicate References at end of paper.

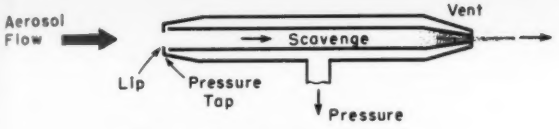

Fig. 5 Working design of probe

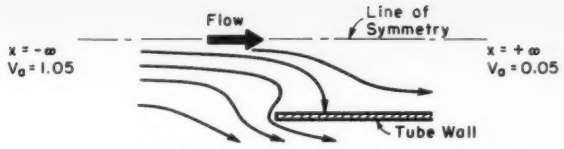

Fig. 6 Fluid streamlines of two-dimensional flow, for $ID/OD = 1$

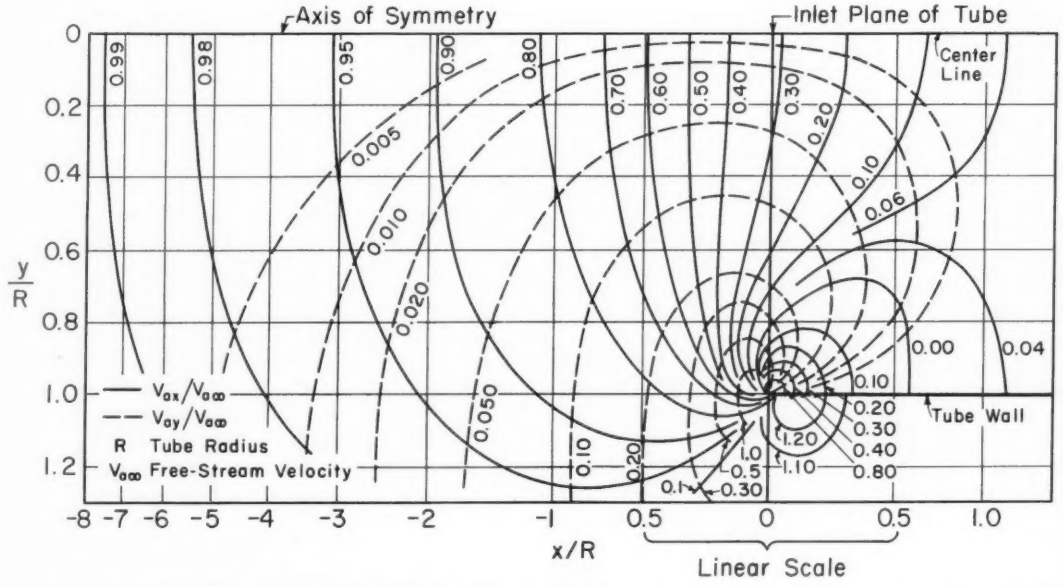

Fig. 7 Contours of constant fluid velocity components, for axisymmetric tube with $ID/OD = 1$. Internal tube velocity equal to 5 per cent of free-stream velocity

(d) The droplets are very small compared to the probe.

(e) The drag coefficient of the droplets is a function only of the Reynolds Number relative to the fluid and varies according to (6).

(f) The drag forces are the only significant forces acting on the droplet. Other forces, namely, virtual mass, gravity, and buoyancy can be shown to be small (1 and 5).

(g) Droplet and gas have the same velocity far upstream.

Internal and External Gas Velocity Fields

The problem to be solved here deals with the mapping of the incompressible, irrotational, three-dimensional flow field near the entrance of an open-end cylindrical tube, the axis of which is aligned with the flow (Fig. 1). The effect of tube-wall thickness was considered by studying the two extreme cases in which the ratio of internal to external diameter is respectively unity (tube with very thin wall) and zero (solid cylinder with very small stagnation hole). In addition, venting considerations call for the former one to have an internal velocity equal to 5 per cent of the undisturbed flow velocity.

Thin-Walled Cylindrical Tube. Approximate construction of the flow field within and around a thin-walled tube is based on a modification of the potential flow solution for the corresponding two-dimensional channel as obtained from (7). Super-position of a uniform velocity 1.05 times as large as and opposite in sign to the channel velocity yields the solution to the two dimensional problem (Fig. 6).

Approximation to the three dimensional problem was obtained by making use of the fact that the relationship between the two-dimensional flow and its axi-symmetric counterpart is similar to that between a circular cylinder and a sphere. Applying correction factors derived from these well-known solutions, the field of Fig. 7 for the flow about a thin-walled axisymmetric tube was obtained.

Thick-Walled Cylindrical Tube ($ID/OD = 0$). In a similar manner the velocity field for a square-ended, round tube, with a very small pressure hole may be derived by modifying the solution for the two-dimensional flow past a two-dimensional step of height $(D/2)$, (6). For the case $ID/OD = 0$, we are interested only in the velocity distribution on the axis of symmetry. The two-dimensional solution of this is shown by a dashed line in Fig. 8.

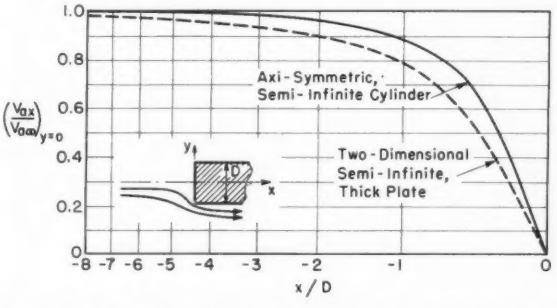

Fig. 8 Fluid velocity distribution on center line, for $ID/OD = 0$ Dashed curve is for two-dimensional flow; solid curve for three-dimensional flow

By applying the correction factors previously mentioned to the dashed curve, the solid curve of Fig. 8 is obtained, representing the desired center-line velocity distribution for a semi-infinite cylinder with $ID/OD = 0$.

The External Motions of the Droplets

According to the previously made simplifying assumption, of the several forces acting upon a droplet, only the aerodynamic drag is of consequence in the practically useful ranges of the controlling parameters. Equating the drag force to the mass-acceleration product, the equations of droplet motion in the x- and y-directions may be written respectively as

$$c_D \frac{\rho_a}{2} [(V_{ay} - V_{wy})^2 + (V_{wx} - V_{ax})^2] \frac{\pi d^2}{4} \cos \alpha = -\frac{\pi d^3}{6} \rho_w \left(V_{wx} \frac{\partial V_{wx}}{\partial x} + V_{wy} \frac{\partial V_{wx}}{\partial y} \right) \quad [2a]$$

$$c_D \frac{\rho_a}{2} [(V_{ay} - V_{wy})^2 + (V_{wx} - V_{ax})^2] \frac{\pi d^2}{4} \sin \alpha = \frac{\pi d^3}{6} \rho_w \left(V_{wx} \frac{\partial V_{wy}}{\partial x} + V_{wy} \frac{\partial V_{wy}}{\partial y} \right) \quad [2b]$$

where

$$\sin \alpha = \frac{V_{ay} - V_{wy}}{\sqrt{(V_{ay} - V_{wy})^2 + (V_{wx} - V_{ax})^2}}$$

$$\cos \alpha = \frac{V_{wx} - V_{ax}}{\sqrt{(V_{ay} - V_{wy})^2 + (V_{wx} - V_{ax})^2}}$$

Now, for a good probe design, the capture and momentum efficiencies should be nearly unity, and the droplet trajectories are, accordingly, nearly straight. On the right-hand sides of the equations of motion, therefore, we may drop the terms involving $V_{wy}\partial V_{wx}/\partial y$ and $V_{wy}\partial V_{wy}/\partial_y$ without sensible error in the ranges of practical interest. Making this approximation, and reforming the equations in dimensionless form, we obtain

$$c_D \left(\frac{3}{4} \frac{\rho_a D}{\rho_w d} \right) \left(\frac{V_{wx}}{V_{a\infty}} - \frac{V_{ax}}{V_{a\infty}} \right) \sqrt{\left(\frac{V_{ay}}{V_{a\infty}} - \frac{V_{wy}}{V_{a\infty}} \right)^2 + \left(\frac{V_{wx}}{V_{a\infty}} - \frac{V_{ax}}{V_{a\infty}} \right)^2} = -\frac{V_{wx}}{V_{a\infty}} \frac{\partial (V_{wx}/V_{a\infty})}{\partial (x/D)} \quad [3a]$$

$$c_D \left(\frac{3}{4} \frac{\rho a D}{\rho_w d} \right) \left(\frac{V_{ay}}{V_{a\infty}} - \frac{V_{wy}}{V_{a\infty}} \right) \sqrt{\left(\frac{V_{ay}}{V_{a\infty}} - \frac{V_{wy}}{V_{a\infty}} \right)^2 + \left(\frac{V_{wx}}{V_{a\infty}} - \frac{V_{ax}}{V_{a\infty}} \right)^2} = -\frac{V_{wx}}{V_{a\infty}} \frac{\partial (V_{wy}/V_{a\infty})}{\partial (x/D)} \quad [3b]$$

Droplet trajectories are defined by the equation

$$\frac{d(y/D)}{d(x/D)} = \frac{V_{wy}/V_{a\infty}}{V_{wx}/V_{a\infty}} \quad [4]$$

In Equations 3, the drag coefficient c_D depends on the relative Reynolds Number of the droplet

$$\text{Rey} = \frac{\rho_a d \sqrt{(V_{ay} - V_{wy})^2 + (V_{wx} - V_{ax})^2}}{\mu_a} \quad [5]$$

A study of the form of Equations 3 then shows that two dimensionless parameters (apart from the probe geometry) control the droplet motion, namely, (i) the characteristic Reynolds Number $\text{Rey}_\infty = \rho_a V_{w\infty} d/\mu_a$ and (ii) the obedience Number, $3\rho_a D/4\rho_w d$, so named because its magnitude is a measure of how closely the droplet trajectories obey the gas motion.

Simultaneous solution of Eq. [3–4] using the drag-coefficient data of (6), yields a complete description of the motions of the droplets. These solutions were carried out numerically with the method of isoclines. Extensive numerical results are presented in (5). Typical results of practical significance are illustrated in Fig. 9 (for $ID/OD = 1.0$) and Fig. 10 (for $ID/OD = 0$).

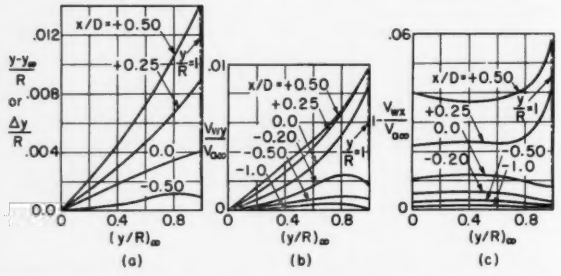

Fig. 9 Typical results of droplet trajectory calculations, for axi-symmetric flow, with $\frac{ID}{OD} = 1$, Reynolds Nubmer $\frac{\rho_a V_{a\infty} d}{\mu_a} =$ 300 and Obedience Number $\frac{3}{4} \frac{\rho_a D}{\rho_w d} = 0.10$

(a) Lateral deflections of trajectories (see Fig. 2 for nomenclature) from location at upstream infinity.
(b) Lateral velocities of droplets in y-direction.
(c) Reduction in longitudinal velocities of droplets.

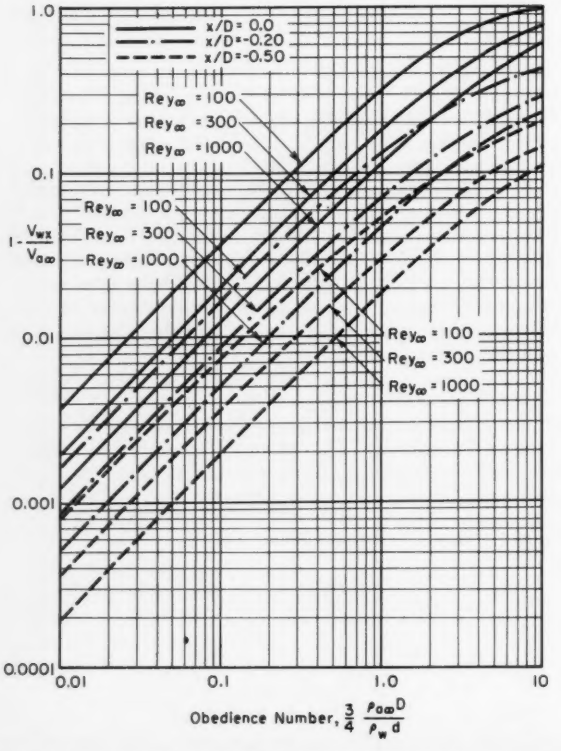

Fig. 10 Decrease in center-line droplet velocity for axi-symmetric probe with $ID/OD = 0$

Capture Efficiency

Thin-Walled Tube. From the data of Fig. 9a it is an easy matter to compute the capture efficiency for the thin-walled

tube with $ID/OD = 1.0$. The fraction of *uncaptured* water is shown in Fig. 11a as a function of Reynolds Number and Obedience Number. For $(x/D) = 0$, the curves show the fraction of the water in the capture area $\pi D^2/4$ which escapes entering the probe mouth. For positive values of x/D (corresponding to stations *within* the probe), the ordinates show the fraction of water in the capture area which is no longer in the gas stream at the abscissa x/D; this fraction is accounted for by the amount escaping the mouth of the probe plus the amount impinging on the internal walls from $x = 0$ to $x = x$.

Thick-Walled Tube. In the case of the thick-walled tube in which $ID/OD \to 0$, the capture efficiency at the stagnation point cannot be calculated from an analysis involving the central streamline only. An indeterminate condition is present there. Removal of the indeterminacy, yields the following expression for the capture efficiency

$$e_{(y/R)_\infty = 0} = \left[\frac{1}{1 + \left[\frac{d(\Delta y/R)}{d(y/R)_\infty} \right]_{(y/R)_\infty = 0}} \right]^2$$

It is assumed here that the droplet behavior along the central streamline will be closely similar for the cases of $ID/OD = 0$ and $ID/OD = 1.0$. This assumption enables us to obtain the desired information from charts like Fig. 9a. The results for capture efficiency are shown in Fig. 11b.

Overpressure in Tube Mouth

The average overpressure in the tube mouth, which is probably a good interpretation of the reading of a static tap very close to the mouth, depends on both the momentum efficiency and capture efficiency. Consequently, from the considerations leading to Figs. 9 and 10, we may expect the dimensionless overpressure

$$\frac{p_{meas} - p_0}{(1/2)\rho_a V_{a_\infty}{}^2 (w_w/w_a)_\infty}$$

to be a function of the probe geometry, the Reynolds Number, and the Obedience Number.

Thick-Walled Tube ($ID/OD = 0$) In this case we need consider only the center-line stream tube. Applying the momentum equation to an infinitesimal length of this stream tube, we have

$$-dp = \rho_a V_{ax} dV_{ax} + \left(\frac{w_w}{A} \right) dV_{wx}$$

which may be rearranged in dimensionless form as

$$-d\left(\frac{p}{\rho_{a_\infty} V_{a_\infty}{}^2} \right) = \frac{\rho_a}{\rho_{a_\infty}} \frac{V_{ax}}{V_{a_\infty}} d\left(\frac{V_{ax}}{V_{a_\infty}} \right) + \left(\frac{w_w}{w_a} \right)_\infty e d\left(\frac{V_{wx}}{V_{a_\infty}} \right) \quad \ldots [6]$$

The first term on the right-hand side represents the contribution from the change in momentum of the gas (assumed to be the same as when the droplets are not present); the second, that of the droplets. When Eq. 6 is integrated from $x = -\infty$ to $x = 0$, the integral of the term in dV_{ax} yields the difference between p_0 and p_∞, the former representing the true stagnation pressure of the gas phase alone. The integral of the term in dV_{wx} gives the overpressure in the tube mouth due to the droplets. Thus we have

$$\frac{p_{meas} - p_0}{\frac{1}{2}\rho_a V_{a_\infty}{}^2 \left(\frac{w_w}{w_a} \right)_\infty} = 2 \left[1 - \frac{(V_{wx})_{x=0}}{V_{a_\infty}} \right] \bar{e} \quad \ldots [7]$$

where $\bar{e}$ is an average value of e over the interval of integration, from $x = -\infty$ to $x = 0$

When the Obedience Number is very small (e.g., very large

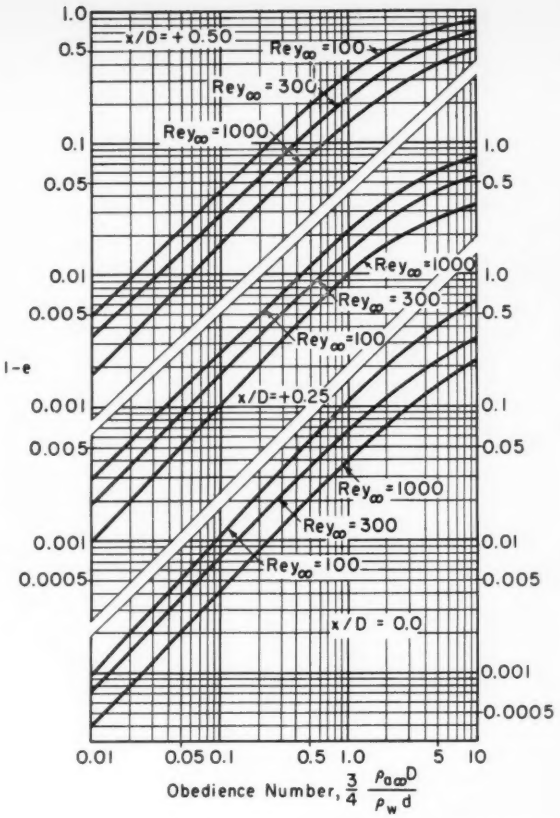

Fig. 11a Uncaptured fraction of droplets for probe with $ID/OD = 1$. Curves for $\frac{x}{D} = 0$ show amount of water escaping probe mouth. Curves for positive values of $\frac{x}{D}$ show amount of water escaping probe plus amount impinging on internal probe walls

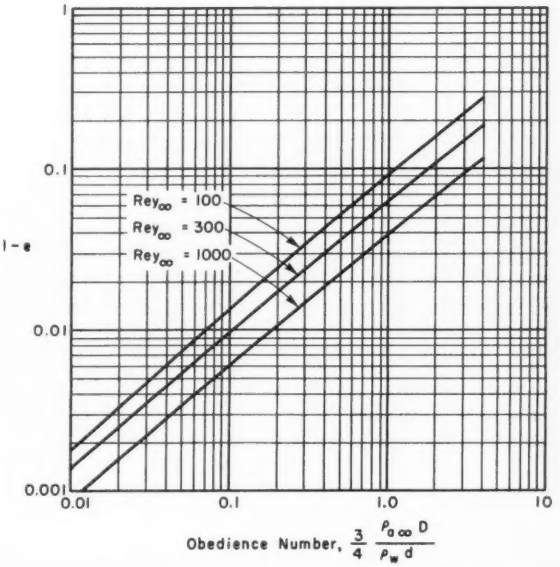

Fig. 11b Uncaptured fraction of droplets on center line for probe with $ID/OD = 0$ in plane $x/D = 0$

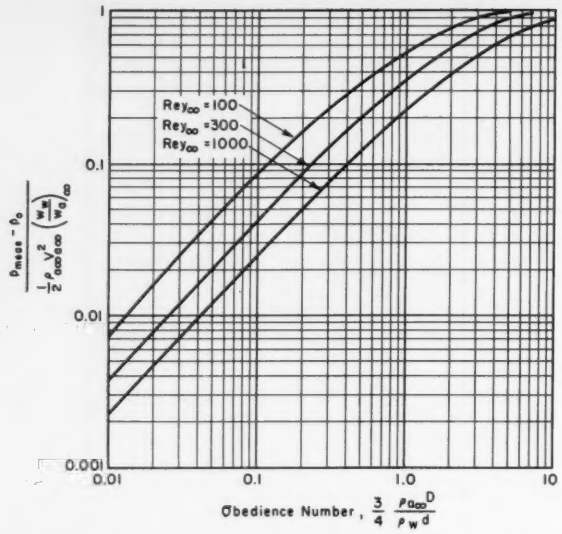

Fig. 12 Overpressure in mouth of thick-walled probe, for $ID/OD = 0$

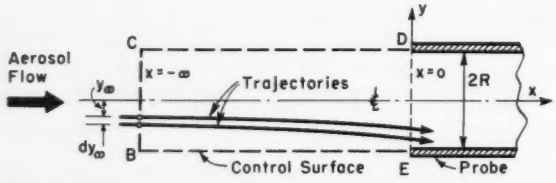

Fig. 13 Control surface for calculation of average overpressure in probe mouth for $ID/OD = 1$

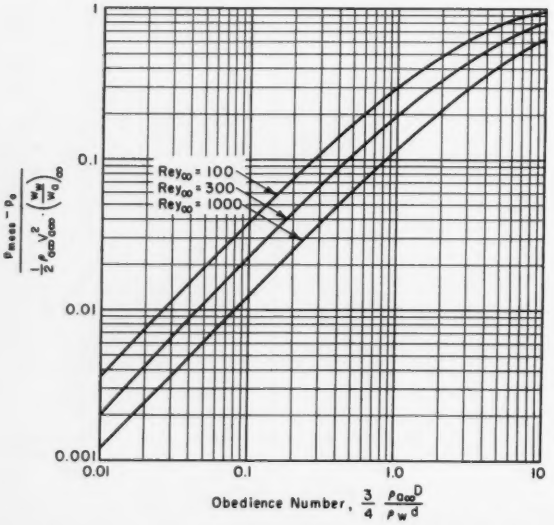

Fig. 14 Average overpressure in mouth of thin-walled probe, for $ID/OD = 1$

droplets, or very small probe), the droplets move with unchanged velocity. Consequently the right-hand side of Eq. 7 vanishes, and the probe error is zero.

When the Obedience Number is very large (e.g., very small droplets, or very large probe), the droplets have the same motion as the gas. Consequently the mixture behaves as a quasi-homogeneous fluid with the effective density $\rho_a[1 + (w_w/w_a)_\infty]$. In Eq. 7, $(V_{wx})_{x=0} = 0$ and the dimensionless overpressure is equal to $2\bar{e}$. For this case, however, the dimensionless over-pressure is equal to unity (Eq. 1), and consequently $\bar{e} = 0.5$. The latter is the mean value between 1.0 (at $x = -\infty$) and 0 (at $x = 0$).

For arbitrary Obedience Numbers and Reynolds Numbers, Eq. 7 may be used in conjunction with Fig. 11b to give the results shown in Fig. 12 for the dimensionless overpressure.

Thin-Walled Tube ($ID/OD = 1.0$). Assuming that the gas motion is unaffected by the droplets, we may compute the average overpressure in the probe mouth by application of the momentum theorem to the droplets passing through the control surface shown in Fig. 13

$$\pi R^2(p_{meas} - p_0) = \left(\frac{w_w}{A}\right)_\infty V_{a\infty}\pi R^2 - \int_{y=0}^{y=R}(V_{wx})_{x=0}\,(dw_w)_{x=0} - \int_{x=-\infty}^{x=0}(V_{wx})_{y=R}(dw_w)_{y=R}$$

The first term on the right-hand side represents the incoming flux of droplet momentum through BC; the second term the outgoing flux through DE; and the third term the outgoing flux through the cylindrical surface represented by CD and BE.

In evaluating the first integral, we consider the elementary flow through an annular-shaped control volume which far upstream is bounded by y_∞ and $y_\infty + dy_\infty$. Then

$$(dw_w)_{x=0} = \left(\frac{w_w}{A}\right)_\infty 2\pi y_\infty dy_\infty$$

Similarly, the elementary flow for the second integral may be written as

$$(dw_w)_{y=R} = \left(\frac{w_w}{A}\right)_\infty 2\pi y_\infty dy_\infty$$

Substituting the latter two expressions into the momentum equation, rearranging in dimensionless form, and taking due note of the necessary changes in limits of integration when we change from y and x as variables to y_∞, we get

$$\frac{p_{meas} - p_0}{\frac{1}{2}\rho_a V_{a\infty}^2\left(\frac{w_w}{w_a}\right)_\infty} = 2\int_0^{\left\{\left(\frac{y_\infty}{R}\right)^2 \text{ for } \frac{y/R=1}{x=0}\right\}}\left(1 - \frac{V_{wx}}{Va_\infty}\right)_{x=0} d\left(\frac{y_\infty}{R}\right)^2 + 2\int_{\left\{\left(\frac{y_\infty}{R}\right)^2 \text{ for } \frac{y/R=1}{x=0}\right\}}^1\left(1 - \frac{V_{wx}}{V_{a\infty}}\right)_{y=R} d\left(\frac{y_\infty}{R}\right)^2 \quad \ldots [8]$$

for the overpressure ratio.

If the momentum-defect curves of Fig. 9c are replotted against $(y/R)^2_\infty$ then the dimensionless overpressure given by Eq. 8 is simply twice the area under the curve formed by the line $x = 0$ joined to the line $(y/R) = 1.0$. Thus Eq. 8 has a simple physical significance: The overpressure is equal to the momentum loss of all the water originally in the projected cross section of the probe.

By carrying out the indicated integrations in Eq. 8, the over-pressure curves of Fig. 14 are obtained. These curves also approach an asymptote of 1 as the Obedience Number becomes very large or the Reynolds Number very small.

Figures 12 and 14 give working curves for design use. They

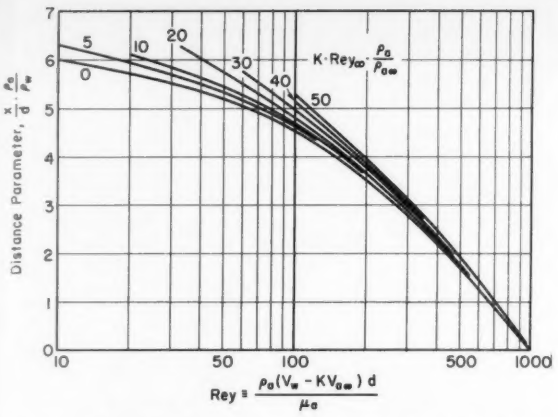

Fig. 15 Universal curves for determining deceleration distance of droplet within probe. Difference in ordinates corresponds to distance required to reduce droplet velocity from the value corresponding to initial Reynolds Number to that corresponding to final Reynolds Number

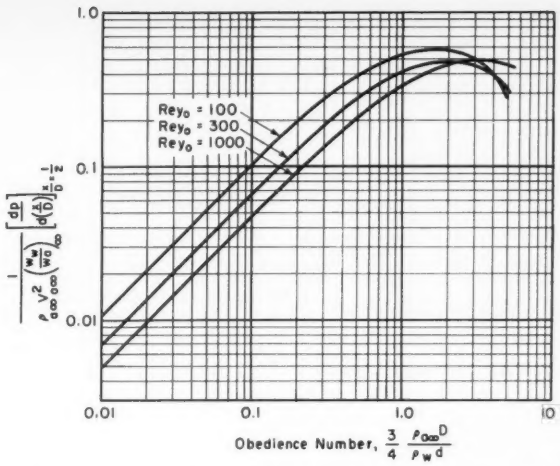

Fig. 16 Longitudinal pressure gradient within probe, reckoned at $x/D = 0.5$, for thin-walled probe with $ID/OD = 1$

show directly and quantitatively the influences of the probe dimensions and of the gas and particle streams on the error in reading at the probe mouth. A study of Figs. 11a, 12 and 14 show that the error in probe reading may be reduced by using a thin-walled probe. Moreover, the error decreases and the capture efficiency increases when the probe diameter, the gas density and the gas viscosity decrease or the gas velocity, the droplet diameter and the droplet density increase.

The Internal Motions of the Droplets

Having crossed the complex flow field outside the probe inlet, the captured droplets enter a zone of comparatively low and uniform velocity. It is of considerable interest to study this region inside the probe for two reasons: First, some indication may be had as to the magnitude of the error recorded by a tap situated too far from the entrance. Secondly, the particle size may be determined by a novel method involving the measurement of the longitudinal pressure gradient within the probe, together with measurement of local droplet-velocity and local water-air ratio.

One-Dimensional Analysis of Internal Droplet Motion. The three-dimensional aspects of the internal droplet dynamics have already been presented in Fig. 9. For many purposes, however, particularly with a well-design probe of high capture efficiency, the gas and droplet motions may be considered one-dimensional. For this simplified model the equations of motion may be written as

$$C_D \frac{\rho_a(V_w - KV_{a\infty})^2}{2}\frac{\pi d^2}{4} = -\frac{\pi d^3}{6}\rho_w V_w \frac{dV_w}{dx} \quad \ldots [9a]$$

where KV_∞ is the average gas velocity in the probe.

Separating variables in this equation, introducing the two Reynolds Numbers

$$\text{Rey} \equiv \frac{(V_w - KV_{a\infty})\rho_a d}{\mu_a};\ \text{Rey}_\infty \equiv \frac{V_{a\infty}\rho_{a\infty} d}{\mu_a} \quad \ldots [9b]$$

and integrating from $x = 0$ to $x = x$, we obtain

$$\frac{\rho_{a\infty}\, x}{\rho_w d} = \frac{4}{3}\int_{Zx=0}^{Zx} \frac{Z\,dZ}{c_D(\text{Rey})^2} \quad \ldots [10a]$$

where

$$Z \equiv \text{Rey} + K\,\text{Rey}_\infty\left(\frac{\rho_a}{\rho_{a\infty}}\right) \quad \ldots [10b]$$

Now, for a specific value of $K\,\text{Rey}_\infty\left(\frac{\rho_a}{\rho_{a\infty}}\right)$, the integral of Eq. 10a is a function of Rey only. Consequently, Eq. 10a, when integrated, gives the distance x required for decelerating the droplets from the speed corresponding to $(\text{Rey})_{x=0}$ to that corresponding to $(\text{Rey})_{x=x}$.

The results of numerical integration, using drag data for incompressible fluids, are shown in Fig. 15. For the lower limit of integration, Rey = 1000 was chosen, so that the curves give directly the distance required to reduce Rey from 1000 to any lower value, however, the curves are also applicable to any initial value of Rey less than 1000. It is merely necessary to take the *difference* in ordinates corresponding to the initial and final Reynolds Numbers.

Pressure Gradient Within Probe. The longitudinal pressure gradient within the probe may be related to the deceleration of the droplets by writing the momentum equation for a cylindrical control volume bounded by the tube walls and of length dx. Thus

$$-A\frac{dp}{dx}\,dx = w_w \frac{dV_w}{dx}\,dx \quad \ldots [11]$$

Now, rearranging and substituting for $\frac{dV_w}{dx}$ the value obtained from Eq. 9a, we get

$$\frac{1}{\rho_{a\infty}V_{a\infty}^2(w_w/w_a)_\infty}\frac{dp}{d(x/D)} = c_D\left(\frac{3}{4}\frac{\rho_a D}{\rho w d}\right)_0 e\left(\frac{V_w}{V_{a\infty}} - K\right)^2\frac{V_{a\infty}}{V_w} \quad \ldots [12]$$

where c_D is a function of $(\text{Rey})_0$, measured at stagnation conditions within the probe.

Equation 12 has two important uses:

(1) It shows how large an error in pressure may be incurred by locating the pressure tap too far from the probe mouth. To illustrate orders of magnitude, calculated results are shown in Fig. 16 for the probe with $ID/OD = 1$, based on the values of e and $\frac{V_w}{V_a}$ computed previously, and reckoned at $x/D = 0.5$

(2) It suggests that the drop size may be inferred from measurements of the pressure gradient near the mouth, the droplet velocity entering the probe, and the droplet flow per unit area entering the probe. Means of measuring these properties by modifications of the present method are indicated in (5).

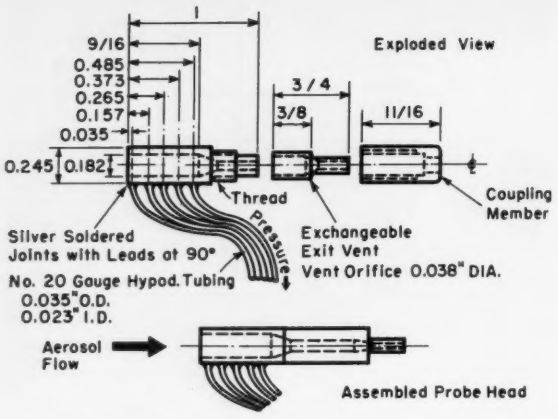

Fig. 17 Details of experimental probe, Configuration V

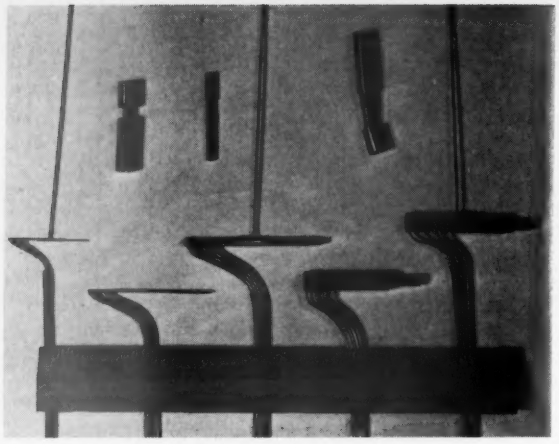

Fig. 18 Photograph of several experimental probes

Experimental Studies

With the object of verifying the results of analysis, an experimental program was undertaken in the form of systematic testing of several probe geometries over a range of free-stream conditions. Of prime interest was the verification of the effects of probe diameter and of the ratio of internal to external diameter on the pressure in the plane of the probe inlet. In addition, measurements of internal pressure gradients were desired, and the effective operation of the venting system was to be demonstrated.

Probe Geometries

Table I summarizes the various geometries investigated. All configurations except VIIA, VIIB, and VIIC were of the type illustrated in Figs. 17 and 18, with internal pressures recorded by wall static taps. In configurations VIIA, VIIB, and VIIC, an effort was made to secure more readings with the help of a static tap installed in a needle traveling parallel to and along the inside wall of the probe proper. All probes incorporated a venting aperture.

Table I Probe Geometries

Probe configuration	Outside probe diam (in.)	ID/OD
I	0.020	0.500
II	0.035	0.657
IIA	0.109	0.211
IIB	0.245	0.0938
III	0.109	0.780
IIIA	0.245	0.347
IV	0.177	0.726
IVA	0.245	0.524
V	0.245	0.746
VI	0.245	0.930
VIIA	0.350	0.838
VIIB	0.350	0.492
VIIC	0.350	0.217

Test Tunnel

Use was made of a test tunnel of transparent lucite, $2^1/_8$ in. in diam and 72 in. long, and located in the Gas Turbine Laboratory at Massachusetts Institute of Technology. The tunnel is subatmospheric, air flow being induced by a downstream steam ejector. Maximum rate of airflow is about one lb per sec, which condition chokes the tunnel and yields a Mach Number of about 0.85 in the test plane near the exit end. A water injection system of 0.350 lb per sec capacity, with parallel downstream injection is installed near the tunnel inlet bellmouth. The atomization is done by the air stream with atomization Mach Numbers up to 0.6. In every case the probe was placed on the axis of the tunnel in the same longitudinal plane, and was carefully aligned with the axis.

Test Procedure and Data Reduction

Comparative testing of the various probe configurations calls for subjecting all instruments to identical Mach Numbers. It may be shown that this condition can be achieved at the test section by maintaining constant (i) the ratio of the static pressure at the test plane to the tunnel inlet pressure (atmospheric); (ii) the water-air ratio; and (iii) the inlet air humidity, air temperature and water temperature. Disturbances of any of these quantities, through energy effects associated with evaporation or condensation of water and heat flow between air and water produce perturbations of the flow properties in the test plane.

Conditions (i) and (ii) were easily achieved in the experimental procedure. Control over humidity and temperatures, however, was not feasible. Instead, theoretical corrections were applied to test data, on the basis of one-dimensional equilibrium flow in the tunnel (5 and 9). Application of the various corrections in general has the effect of reducing the data to some standard condition; this condition is here taken as the one in which thermal energy interchanges between air and droplets are absent.

Reduction to standard conditions further calls for a correction of the error introduced by the presence of the scavenging vent. This requires a calibration of each instrument against a conventional Pitot tube in a dry stream. The smaller the instrument, the more essential this calibration becomes because of the difficulty of controlling the vent area with accuracy. In general, the deviation of the probe reading from that of the standard Pitot tube was within 1 per cent of the free-stream dynamic pressure. The calibration has the further advantage of yielding useful information on the characteristics of each static pressure tap. For example, a tap located too near the inlet may be found to read incorrectly.

In a stream containing water droplets, a great deal of attention must be devoted to the technique of keeping pressure taps free of water. A scheme used successfully involved the use of pressurized manometers. Pressurization followed by

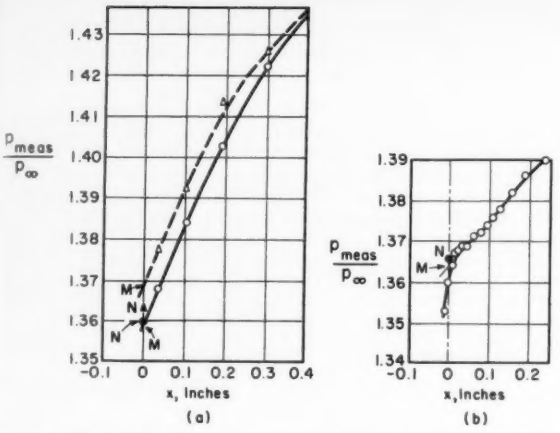

Fig. 19 Typical pressure measurements near probe mouths with $\frac{p_\infty}{p_{atm}} = 0.648$, $\frac{w_w}{w_a} = 0.19$, $M_\infty = 0.675$

	Configuration	Atmospheric pressure	Inlet dry bulb temp	Inlet wet bulb temp	Inlet water temp
Fig. 19a	IV	30.216" Hg	70.5 F	54 F	51 F
	IVA	30.146	72	53	40
Fig. 19b	VIIA	30.180	75	58	56

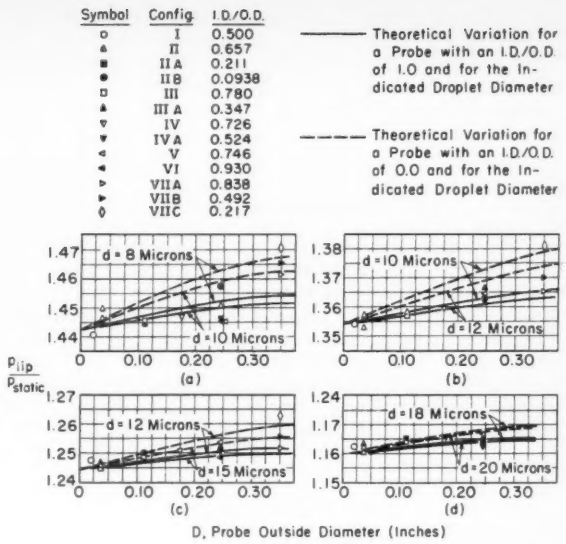
Symbol Config. I.D./O.D.
○ I 0.500
△ II 0.657
■ II A 0.211
● II B 0.0938
□ III 0.780
▲ III A 0.347
▽ IV 0.726
▼ IV A 0.524
◁ V 0.746
◀ VI 0.930
▷ VII A 0.838
▶ VII B 0.492
◇ VII C 0.217
Theoretical Variation for a Probe with an I.D./O.D. of 1.0 and for the Indicated Droplet Diameter
Theoretical Variation for a Probe with an I.D./O.D. of 0.0 and for the Indicated Droplet Diameter
$\frac{p_{tip}}{p_{static}}$
d = 8 Microns
d = 10 Microns
(a)
d = 10 Microns
d = 12 Microns
(b)
d = 12 Microns
d = 15 Microns
(c)
d = 18 Microns
d = 20 Microns
(d)
D, Probe Outside Diameter (Inches)

Fig. 20 Summary of corrected stagnation pressures read by the different probe configurations

Chart	p_∞/p_{atm}	$(w_w/w_a)_\infty$	M_∞
(a)	0.620	0.128	0.744
(b)	0.648	0.204	0.673
(c)	0.734	0.182	0.566
(d)	0.810	0.160	0.469

establishment of equilibrium through a rigidly-enforced one-way flow from manometer to tunnel was the solution to the problem of keeping the pressure-transfer passages free of water.

Test Results

Figs. 19a and 19b show typical static-pressures recorded within two of the experimental probes. The data of Fig. 19a were obtained with probe configurations IV and IVA, having individual pressure taps. Fig. 19b refers to probe VIIA, containing a longitudinally-traversing static tap. Point M represents the extrapolated measured pressure in the plane of the inlet. Point N represents the inlet-plane pressure after correction to standard air flow and water flow conditions.

Data such as those shown in Fig. 19 were obtained for each of the probes of Table I over a range of water-air ratios and air Mach numbers. In each case the stagnation pressure measured by the probe was interpreted to be that found by extrapolating the recorded static pressures to the inlet plane and then correcting to standard corrections (e.g., point N in Fig. 19 is taken as the measured stagnation pressure). A grand summary of all measured stagnation pressure—taken in the foregoing sense—is presented in Fig. 20. Each of the four charts shown in Fig. 20 is for a particular combination of water-air ratio and Mach Number. On each chart may be seen the effects of probe diameter and of the ratio of internal to external diameter.

In general, the data in Fig. 20 fan out in a triangular band from an apex on the vertical axis. Following the reasoning associated with Fig. 3, the position of this apex (on the vertical line $D = 0$) represents the true stagnation pressure. It should be noted that such an *inferred* value of the true stagnation pressure was necessary because there is no absolute method of determining the latter.

Apart from the experimental results, there are shown in Fig. 20 the theoretically predicted error as found from Figs. 12 and 14. In order to employ these charts, it is necessary to know the volume-surface mean diameter of the droplets. The latter was estimated from Fig. 16, using measurements of the internal pressure gradient near the probe mouth (see Fig. 19, for example), together with independent measurements of water flow per unit area. The droplet diameters so found are in reasonably good agreement with those of Nukiyama and Tanasawa (8). The curves in Fig. 20 show the predicted probe errors for the range of droplet sizes in each test found as described, and for the two limiting cases of $ID/OD = 0$ and $ID/OD = 1.0$.

The differences in stagnation pressure measured by the different probe configurations are significant but are not large compared with the experimental accuracy. Consequently a considerable amount of apparent scatter in the data is introduced when these are plotted, as in Fig. 20, on a scale large enough to display differences. It is evident that the theoretical predictions are in general agreement with the test results:

(1) The overpressure increases as the probe size increases.

(2) The overpressure increases as the ratio ID/OD decreases.

(3) The magnitude of the measured error is of the same order as that given by the theory.

Since, in the range of variables tested, the errors in probe are small, it is not considered of practical importance to predict the error with great accuracy. Moreover, the difficulties of precise experimental measurement preclude the possibility of accurately observing such small errors.

Fig. 20 shows finally the feasiblity of constructing a stagnation pressure probe of convenient size and yet of satisfactory accuracy.

Conclusions

1. A simple, practical probe design capable of measuring the stagnation pressure of the gas phase in a droplet-laden

stream has been developed. Its principle of operation has been formulated and verified experimentally.

2. A theory of probe operation is presented, adaptable to any stream carrying suspended bodies of density greater than that of the stream. Generalized curves have been worked out providing design data for any such application.

Acknowledgments

The work described here was supported partly under Contract N5ori-07878 with the Power Branch of the Office of Naval Research and partly by the Procter and Gamble Fellowship at MIT. It was carried out in the MIT Gas Turbine Laboratory with the heplful cooperation of the Laboratory Staff.

It is a pleasure to acknowledge particularly the contributions to this work of Prof. Arthur A. Fowle, Harry Foust, Dalton Baugh and Margaret Tefft.

References

1 Boucher, R. M. G., "Sur le fonctionnement de l'épurateur a microbrouillards Aerojet-Venturi," *Chaleur et Industrie*, no. 328, November 1952.

2 Brun, R. J., Serafani, J. S. and Gallagher, H. M., "Impingement of Cloud Droplets on Aerodynamic Bodies as Affected by Compressibility of Air Flow Around the Body," NACA TN 2903, March 1953.

3 Carpenter, James W. and Martin, W. L., "Construction and Preliminary Test of a Traversing Stagnation Pressure Probe for a Large Scale Aerothermopressor," Thesis for Naval E. Degree, May 1954, MIT, Cambridge, Mass.

4 Cheatham, John B., Jr. "The Photometric Measurement of Particle Size," Thesis for M.E. Degree, September 1954, MIT, Cambridge, Mass.

5 Dussourd, Jules L., "A Theoretical and Experimental Investigation of a Deceleration Probe for Measurement of Several Properties of a Droplet-Laden Air Stream," Sc. D. Thesis, Department of Mechanical Engineering, MIT, 1954.

6 Eisner, "Das Widerstandproblem," Third International Congress of Applied Mechanics, Stockholm, 1930.

7 Milne-Thompson, L. M., "Theoretical Hydrodynamics," McMillan and Co., London, 1938.

8 Nukiyama, S. and Tanasawa, T., "An Experiment on the Atomization of Liquids by Means of an Air Stream," *Transactions ASME*, Japan, vol. 4, Report 1–6, (1938).

9 Shapiro, A. H., "The Dynamics and Thermodynamics of Compressible Fluid Flow," Ronald Press, New York 1953.

Mass-Transfer Cooling of a Laminar Boundary Layer by Injection of a Light-Weight Foreign Gas[1]

E. R. G. ECKERT,[2] P. J. SCHNEIDER,[3] A. A. HAYDAY[4] and R. M. LARSON[5]

University of Minnesota, Minneapolis, Minn.

Analytical predictions are given for the development of the velocity, temperature and concentration fields in a laminar air boundary layer on a flat plate in high-speed dissipative flow, the plate being considered porous and cooled by injection of hydrogen from its surface. The admixture of hydrogen, having a low density and high thermal capacity relative to air, is shown to greatly diminish the skin friction and to markedly relieve the adverse thermal effects of intense aerodynamic heating under conditions of hypersonic flow.

Nomenclature

A = $\frac{1}{4}(\gamma_\infty - 1)M^2{}_\infty$
c_n = integration constants
c_p = constant-pressure thermal capacity
c_v = constant-volume thermal capacity
c_{f_x} = local skin-friction coefficient = $(2\mu_w/\rho_\infty u^2{}_\infty)(\partial u/\partial y)_w$
D_{12} = coefficient of ordinary diffusion
$f(\eta^*)$ = modified stream function
f_w = wall injection parameter = $-2\varphi_{\rho_w}(v_w/u_\infty)\sqrt{Re_x}$
h = unit surface conductance
k = mixture thermal conductivity
M_i = molecular weight of i'th component in mixture
M_∞ = free-stream Mach number
Nu = local Nusselt number = hx/k_∞
Pr_∞ = free-stream Prandtl number = $c_{p\infty}\mu_\infty/k_\infty$
q'' = heat flux per unit area
Re_x = local free-stream Reynolds number = $u_\infty x/\nu_\infty$
Sc = Schmidt number = ν_∞/D_{12}
T = normalized mixture temperature = t/t_∞, ($t_\infty = 392°\mathrm{R}$)
t = local mixture temperature (absolute)
t_r = recovery temperature
u = velocity component parallel to flow (x-direction)
v = velocity component perpendicular to plate surface (y-direction)
W = mass fraction of coolant in binary flow
x = coordinate parallel to plate surface
y = coordinate perpendicular to plate surface
γ_∞ = specific-heat ratio of free-stream fluid = $c_{p\infty}/c_{v\infty}$
η_B = Blasius similarity coordinate = $\frac{1}{2}y(u_\infty/\nu_\infty x)^{\frac{1}{2}}$
η^* = similarity coordinate defined by Eq. [5]
μ = dynamic viscosity of mixture
ν_∞ = kinematic viscosity of free-stream fluid = μ_∞/ρ_∞
ρ = mass density of mixture
σ = recovery factor = $2(T_r - 1)/(\gamma_\infty - 1)M_\infty{}^2$
φ_c = normalized mixture thermal capacity = cp/cp_∞
φ_{c12} = normalized pure-component thermal capacity difference = $\dfrac{c_{p1} - c_{p2}}{c_{p\infty}}$
φ_k = normalized mixture thermal conductivity = k/k_∞
φ_μ = normalized mixture viscosity = μ/μ_∞
φ_ρ = normalized mixture density = ρ/ρ_∞
Ψ = stream function = $\sqrt{\nu_\infty u_\infty x'}\, f(\eta^*)$

Subscripts

1 = foreign component in binary mixture (hydrogen)
2 = primary component in binary mixture (air)
r = recovery
w = wall ($y = 0$)
∞ = free stream ($y \to \infty$)

Primes (′) denote differentiation with respect to η^*

Received June 21, 1957.

[1] Heat Transfer Laboratory, University of Minnesota.
[2] Professor of Mechanical Engineering. Mem. ARS.
[3] Research Associate in Mechanical Engineering.
[4] Graduate Research Assistant in Mechanical Engineering.
[5] Graduate Teaching Assistant in Mathematics.

I. Introduction

THE USE of mass-transfer cooling is being investigated as a means of protecting the surfaces of high-speed aircraft, missiles and satellites exposed to intense aerodynamic heating. The need for cooling such surfaces becomes critical under one of three flight situations: (a) Rapid acceleration at constant or varying altitude, (b) sustained flight at high Mach numbers, and (c) re-entry flight into the earth's atmosphere.

The essential mechanical feature of mass-transfer cooling is represented by injection of a foreign gas into the boundary-layer fluid. This feature distinguishes it from conventional cooling methods which depend on either a high thermal-capacity heat sink within the structure or artificial cooling at the inner surface of the skin. If the injection gas is identical with the boundary-layer fluid, then the method is known as *transpiration cooling*, while if the injection and mainstream fluids are dissimilar the method is called *mass-transfer cooling*. The foreign injection fluid may be a gas, or it may be a liquid which covers the porous surface as a film and evaporates into the boundary layer. An alternate technique is represented by sublimation cooling in which the walls of the vehicle are constructed of a solid material whose surface continuously evaporates into the high-temperature boundary-layer air. In all such processes the heat and momentum transfer are accompanied by a simultaneous diffusion of the injection or generated gas away from the surface. This diffusion process has a marked effect on the boundary-layer development, particularly when the properties of the diffusing foreign gas are widely different from the properties of the main stream.

Results of an exact calculation were reported in (1)[6] for the velocity and concentration fields in a laminar isothermal boundary layer on a flat plate with locally uniform pressure and with injection of a foreign gas from the surface, assuming an uncontaminated coolant reservoir in which no air penetrates the surface into the interior of the plate. In that analysis the fluid properties were allowed to vary with local mixture concentration in the binary isothermal boundary layer, and numerical calculations were performed for injection of hydrogen into air. Hydrogen was selected as a coolant because its properties are widely different from those of air. The results of that study therefore indicated the strong effect of property variations on the mass-transfer process. The purpose of this present paper is to report on similar calculations for a high-velocity boundary layer on a cooled plate. All fluid properties in the non-isothermal case are again considered variable, the dependence now being on both mixture concentration and mixture temperature.

II. Differential Equations and Boundary Conditions

The differential equations for a non-isothermal binary boundary layer with variable fluid properties and in the absence of a pressure gradient are (2)

Continuity
$$\frac{\partial}{\partial x}(\rho u) + \frac{\partial}{\partial y}(\rho v) = 0 \quad \ldots\ldots [1]$$

Momentum
$$\rho u \frac{\partial u}{\partial x} + \rho v \frac{\partial u}{\partial y} - \frac{\partial}{\partial y}\left(\mu \frac{\partial u}{\partial y}\right) = 0 \quad \ldots\ldots [2]$$

Diffusion
$$\rho u \frac{\partial W}{\partial x} + \rho v \frac{\partial W}{\partial y} - \frac{\partial}{\partial y}\left(\rho D_{12} \frac{\partial W}{\partial y}\right) = 0 \quad \ldots\ldots [3]$$

Energy
$$\rho c_p u \frac{\partial t}{\partial x} + \rho c_p v \frac{\partial t}{\partial y} - \frac{\partial}{\partial y}\left(k \frac{\partial t}{\partial y}\right) - \mu \left(\frac{\partial u}{\partial y}\right)^2 + \rho D_{12}(c_{p_2} - c_{p_1}) \frac{\partial t}{\partial y} \frac{\partial W}{\partial y} = 0 \quad \ldots\ldots [4]$$

[6] Numbers in parentheses indicate References at end of paper.

The effect of thermal diffusion (mass diffusion in the presence of a temperature gradient) has been neglected in Eq. [3–4]. The last term in the energy equation is absent in the conventional single-component boundary layer; it represents the diffusion of enthalpy in a binary mixture.

The continuity equation is satisfied by introducing a stream function Ψ. Eq. [2–4] are then reduced to a corresponding set of ordinary simultaneous differential equation through a similarity transformation η^* defined by

$$\eta^* = \frac{1}{2}\sqrt{\frac{u_\infty}{\nu_\infty x}} \int_0^y \frac{1}{\varphi_\mu} dy \quad \ldots\ldots [5]$$

and a modified stream function $f(\eta^*)$. The transformation η^* is related to the familiar Blasius similarity coordinate $\eta_B = (y/2)(u_\infty/\nu_\infty x)^{\frac{1}{2}}$ by the relation

$$\eta_B(\eta^*) = \int_0^{\eta^*} \varphi_\mu d\eta^* \quad \ldots\ldots [6]$$

which is valid for any fixed x. The transformed results corresponding to Eq. [2–4] are

Momentum
$$[(f'/\varphi_\rho\varphi_\mu)']' + f(f'/\varphi_\rho\varphi_\mu)' = 0 \quad \ldots\ldots [7]$$

Diffusion
$$[(\varphi_\rho/\varphi_\mu Sc)W']' + fW' = 0 \quad \ldots\ldots [8]$$

Energy
$$(1/Pr_\infty)(\varphi_k T'/\varphi_\mu)' + (\varphi_\rho\varphi_{c_{12}}/\varphi_\mu Sc)W'T' + \varphi_c f T' + A[(f'/\varphi_\rho\varphi_\mu)']^2 = 0 \quad \ldots\ldots [9]$$

In these equations the primes ($'$) denote differentiation with respect to η^*; all other symbols are defined in the Nomenclature. The mixture properties Sc, φ_ρ, φ_μ, φ_k, φ_c, and $\varphi_{c_{12}}$ depend, in general, on both the local mixture concentration W and local mixture temperature T (Article III).

Equations [7–9] must satisfy a total of seven boundary conditions, all of which are the same as in [1] except for two additional conditions on the energy equation

$$\left.\begin{array}{l} f' = 0 \\ f = f_w = C_2/(1 - W_w) \\ W = W_w \\ T = T_w \end{array}\right\} \eta^* = 0, \left.\begin{array}{l} f' = 2 \\ W = 0 \\ T = 1 \end{array}\right\} \eta^* \to \infty \quad \ldots\ldots [10]$$

The second condition at $\eta^* = 0$ implies that there is no mass flow of air through the wall (1). Although a diffusion of boundary-layer air into the plate occurs because of the finite concentration gradient at the surface, it is assumed that the diffusion velocity of this air is small compared to the convective velocity of the coolant in the porous plate, and that accordingly the mass of air that does enter the plate is negligible. Thus $(1 - W_w)\rho_w v_w = -\rho_w D_{12_w}(\partial W/\partial y)_w$, where $v_w = -[(\varphi_\rho)_w/2](u_\infty\nu_\infty/x)^{\frac{1}{2}} f_w$. Transformation of this to η^* gives the second condition in Eq. [10], with C_2 defined by Eq. [15]. Either the surface injection rate f_w or the surface mass concentration W_w may be chosen arbitrarily.

III. Property Values

Suitable methods for calculating the concentration and temperature dependence of the various transport properties appearing in Eq. [7–9] have been summarized in (3).

1. *Mixture Schmidt number*, $Sc = \nu_\infty/D_{12}$; assumed dependent on T only (4). Values of Sc calculated by Hirschfelder's method (3) are shown in Fig. 1 for $t_\infty = 392$ R, $\nu_\infty = 0.340$ ft²/hr, and $1 \leq T \leq 10$.

2. *Pure-component thermal capacity*, c_{p1} and c_{p2}; selected from (5) for molecular hydrogen and dry air. Calculated values of $\varphi_{c_{12}} = (c_{p_1} - c_{p_2})/c_{p\infty}$ are shown in Fig. 1 with $c_{p\infty} = 0.239$ Btu/lb-R.

3. *Mixture density ratio*, φ_ρ; calculated assuming perfect-gas behavior as

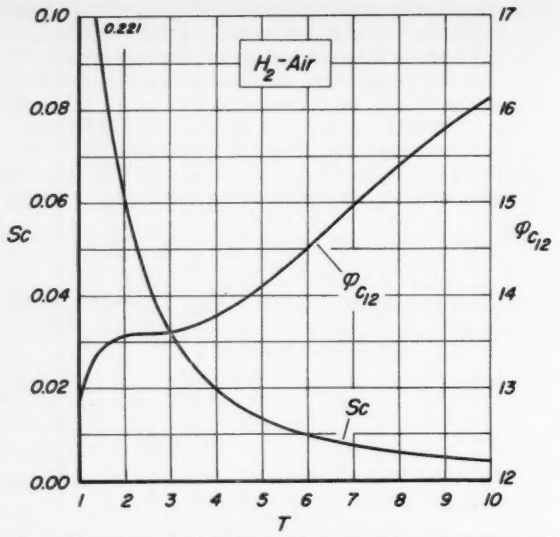

Fig. 1 Variation of Schmidt number Sc and pure-component thermal capacity difference $\varphi_{c_{12}}$ with mixture temperature $T = t/t_\infty$ for hydrogen-air mixture

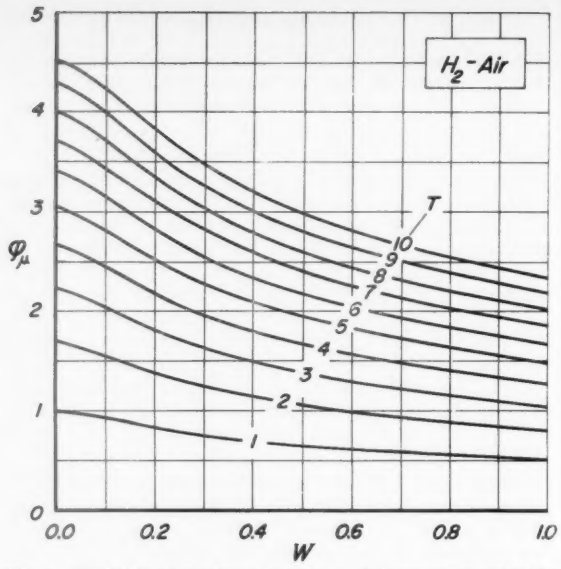

Fig. 2 Variation of mixture viscosity φ_μ with mass concentration W and mixture temperature T for hydrogen-air mixture

$$\varphi_\rho = 1/[1 + (M_2/M_1 - 1)W]T = 1/(1 + 13.5W)T$$

4. *Mixture viscosity ratio, φ_μ;* calculated by Wilke's method (3) as

$$\varphi_\mu = \frac{\mu_1/\mu_\infty}{1 + 0.1296(1 - W)/W} + \frac{\mu_2/\mu_\infty}{1 + 3.9730W/(1 - W)}$$

the pure-component viscosities μ_1 and μ_2 being selected from NBS-NACA tabulations (6), Tables 7.39 and 2.39. Calculated values of $\varphi_\mu = \mu/\mu_\infty$ are shown in Fig. 2 with $\mu_\infty = 0.0345$ lb/hr-ft.

5. *Mixture conductivity ratio, φ_k;* calculated by Enskog's method (3) as

$$\varphi_k = \frac{k_1/\alpha_1 + k_2/\alpha_2 + 0.2890\sqrt{k_1k_2}/\alpha_1\alpha_2}{(1 - 0.0209/\alpha_1\alpha_2)k_\infty}$$

where $\alpha_1 = 1 + 0.1886(1 - W)/W$ and $\alpha_2 = 1 + 14.2280W/(1 - W)$, the pure-component conductivities k_1 and k_2 being calculated by Hirschfelder's method (4). Values of $\varphi_k = k/k_\infty$ are shown in Fig. 3 with $k_\infty = 112.6 \times 10^{-4}$ Btu/hr-ft-R.

6. *Mixture thermal capacity ratio, φ_c;* calculated assuming perfect-gas behavior for each component as

$$\varphi_c = \frac{c_{p_1}}{c_{p\infty}} W + \frac{c_{p_2}}{c_{p\infty}} (1 - W)$$

IV. Method of Solution

Equations [7–9] together with the boundary conditions in Eq. [10] can be transformed into the following system of simultaneous integral equations

Momentum

$$f = f_w + C_1 \int_0^{\eta^*} \varphi_\rho\varphi_\mu \int_0^{\eta^*} e^{-\int_0^{\eta^*} f d\eta^*} d\eta^* d\eta^* \ldots [11]$$

Diffusion

$$W = W_w + C_2 \int_0^{\eta^*} (\varphi_\mu Sc/\varphi_\rho) e^{-\int_0^{\eta^*} (\varphi_\mu Sc/\varphi_\rho) f d\eta^*} d\eta^* \ldots [12]$$

Energy

$$T = T_w + C_3 \int_0^{\eta^*} (\varphi_\mu/\varphi_k) e^{-\int_0^{\eta^*} \lambda(\eta^*) d\eta^*} d\eta^* - \int_0^{\eta^*} (\varphi_\mu/\varphi_k) e^{-\int_0^{\eta^*} \lambda(\eta^*) d\eta^*} \int_0^{\eta^*} g(\eta^*) e^{+\int_0^{\eta^*} \lambda(\eta^*) d\eta^*} d\eta^* d\eta^* \ldots [13]$$

where

$$C_1 = 2/\int_0^\infty e^{-\int_0^{\eta^*} f d\eta^*} d\eta^* \ldots [14]$$

$$C_2 = -W_w/\int_0^\infty (\varphi_\mu Sc/\varphi_\rho) e^{-\int_0^{\eta^*} (\varphi_\mu Sc/\varphi_\rho) f d\eta} d\eta^* \ldots [15]$$

and

$$C_3 = \frac{1 - T_w + \int_0^\infty (\varphi_\mu/\varphi_k) e^{-\int_0^{\eta^*} \lambda(\eta^*) d\eta^*} \left[\int_0^{\eta^*} g(\eta^*) e^{+\int_0^{\eta^*} \lambda(\eta^*) d\eta^*} d\eta^* d\eta^*\right]}{\int_0^\infty (\varphi_\mu/\varphi_k) e^{-\int_0^{\eta^*} \lambda(\eta^*) d\eta^*} d\eta^*} \ldots [16]$$

In these integral equations, the $\lambda(\eta^*)$ and $g(\eta^*)$ are defined as

$$\lambda(\eta^*) = (Pr_\infty/\varphi_k)(\varphi_c\varphi_\mu f + \varphi_{c_{12}}\varphi_\rho\varphi W'/Sc)$$

and

$$g(\eta^*) = AP_{R\infty}[(f'/\varphi_\rho\varphi_\mu)']^2$$

wherein $Pr_\infty = 0.73$ and the A is constant. Of the six imposed boundary conditions, three appear as constants C_1, C_2, and C_3, and the remainder are surface values f_w, w_w, and T_w. The explicit relationship $f_w = C_2/(1 - W_w)$ is obtained directly from Eq. [2, 3, and 12]. If the boundary condition is one of an adiabatic wall $(T')_w = 0$, then Eq. [11–12] remain unchanged and Eq. [13] changes to

$$T = T_w - \frac{\int_0^{\eta^*} (\varphi_\mu/\varphi_k) e^{-\int_0^{\eta^*} \lambda(\eta^*) d\eta^*} \left[\int_0^{\eta^*} g(\eta^*) e^{+\int_0^{\eta^*} \lambda(\eta^*) d\eta^*} d\eta^* d\eta^*\right]}{\int_0^{\eta^*} g(\eta^*) e^{+\int_0^{\eta^*} \lambda(\eta^*) d\eta^*} d\eta^*} \ldots [17]$$

where

$$T_w = 1 + \frac{\int_0^\infty (\varphi_\mu/\varphi_k) e^{-\int_0^{\eta^*} \lambda(\eta^*) d\eta^*} \left[\int_0^{\eta^*} g(\eta^*) e^{-\int_0^{\eta^*} \lambda(\eta^*) d\eta} d\eta^* d\eta^*\right]}{\int_0^{\eta^*} g(\eta^*) e^{-\int_0^{\eta^*} \lambda(\eta^*) d\eta} d\eta^*} \ldots [18]$$

The integral Equations [11–13] or [17] were solved by successive approximations. A reasonable guess at the functions

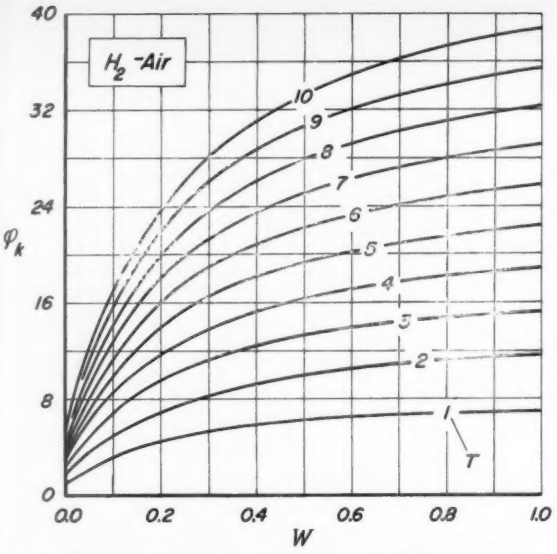

Fig. 3 Variation of mixture conductivity φ_k with mass concentration W and mixture temperature T for hydrogen-air mixture

$f'(\eta^*)$, $W(\eta^*)$, and $T(\eta^*)$ together with a selection of W_w and T_w and an estimated f_w constituted the initial approximation. It was found that rapid convergence of successive iterations could be achieved by first iterating on $f'(\eta^*)$ alone, using Eq. [11] and holding $W(\eta^*)$ and $T(\eta^*)$ fixed. This procedure yields a set of approximations which represent consistant guesses. These generated guesses were then used as first approximations for a complete iterative cycle in which ordered changes in all functions were made simultaneously. The cycle which yielded the most rapid convergence proceeded in the order (W, T, f', f_w) to (W, T, f', T_w).[7]

Machine Calculations. The iterative method described above formed the basis of solution on a Univac Scientific Computer. Operations were performed on groups of numbers stored in the computer, each group representing a column of values for the index $c\Delta\eta^*$. All numbers were in scientific notation with eight significant digits and an exponent being stored. A floating-point interpretative system (FLIP) developed by Convair was used for the basic arithmetic, and a pseudo-interpretative vector-operation library was developed to handle operations on the columns of numbers. These systems greatly simplified the coding. It should be remarked in this connection that early attempts using the conventional Blasius transformation were difficult to code because a perturbation method was required to force convergence. Approximately 65 sec were used to set up the program for a particular case, and 45 sec were required for each iteration and monitoring. Each solution was carried through an average of 10 iterations.

A tabular interval of $\Delta\eta^* = 1$ was used in all solutions. However, repeat solutions were carried out in several cases with $\Delta\eta^* = \frac{1}{2}$ and $\frac{1}{4}$ but no significant changes were noted with the finer subdivisions. Integration of the tabular entries was performed by the trapezoidal rule. The iterative scheme used was such that round-off errors were damped out; thus the sources of error are due only to inaccuracies in property values, the integration formula, and incomplete convergence. An integration of the difference between two consecutive solutions provided a convergence criterion; if this result was less than 10^{-4} for each of the functions f', W, and T, then the solutions were terminated. With this criterion the last two approximations in each solution agreed point-by-point to four significant figures.

[7] The particular transformation Eq. [5] was chosen after attempts to solve the problem with the usual Blasius transformation Eq. [6] failed owing to lack of convergence.

V. Results

Typical results of the calculation are shown in Fig. 4 for injection of hydrogen into air, all results being plotted against the Blasius coordinate $\eta_B = (y/2)\sqrt{u_\infty/\nu_\infty x}$. The upper set of curves represent temperature profiles for $M_\infty = 12$, $T_w = t_w/t_\infty = 2$ and 6, and $W_w = 0.0$, 0.1, 0.2, 0.4, 0.6 and 0.8. The Van Driest curve (7) for $T_w = 6$ and $W_w = 0$ (zero injection) differs from the present results for $W_w = 0$ because of different assumptions on the temperature dependency of pure air. The temperature profiles for finite injection rates indicate that the peak boundary-layer temperatures are substantially reduced by injection of a light-weight gas of high thermal capacity. The surface temperature gradients are seen to be greatly reduced at this high Mach number even with a comparatively low surface mass concentration of $W_w = 0.1$. This corresponds to a high reduction in the rate at which heat must be removed from the plate to maintain the specified surface temperature. The middle set of curves in Fig. 4 show the shapes of the mass concentration profiles for $M_\infty = 12$ and $T_w \doteq 6$. The velocity profiles shown in the lower set of curves in Fig. 4 were determined from the calculated mass-velocity profiles as $u/u_\infty = (\frac{1}{2}\varphi_\rho)df/d\eta_B$.

Results corresponding to those in Fig. 4, but for the case of zero dissipation (designated $M_\infty = 0$), are given in Fig. 5 for $T_w = 2$ and 6. Note that the concentration profiles are not markedly altered by neglect of the frictional heating. The effect of wall temperature on the temperature profiles is shown in Fig. 6 for $M_\infty = 0$ and 8. In contrast to the results of Smith (8), no reversals in the heat flow (surface temperature gradients) were noted in the combination of Mach numbers,

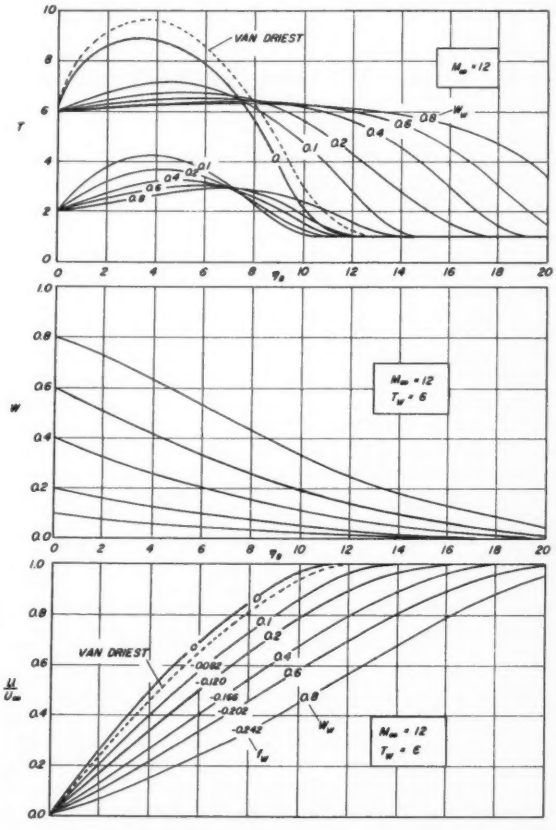

Fig. 4 Temperature, mass concentration and velocity profiles in a laminar hydrogen-air boundary layer as a function of wall concentration W_w for a free-stream Mach number of 12 and a wall-to-free-stream temperature ratio of $t_w/t_\infty = 6$ ($t_\infty = 392$ R)

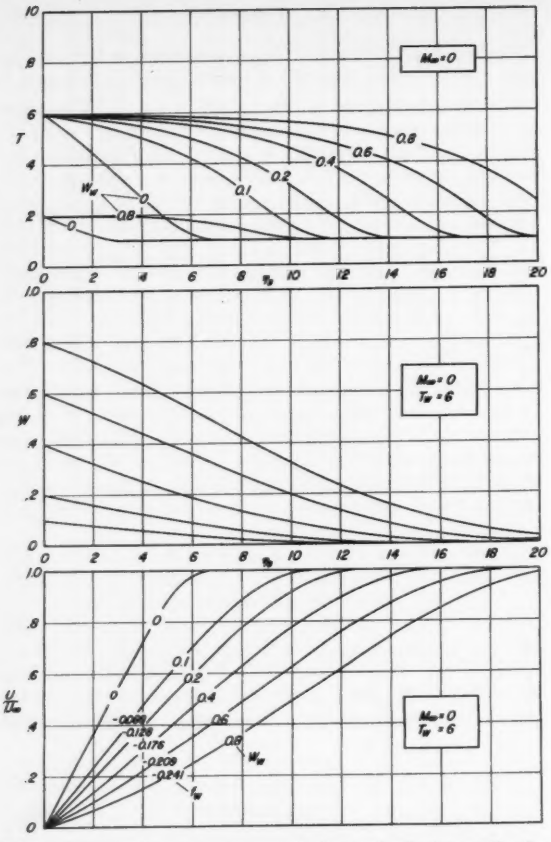

Fig. 5 Temperature, mass concentration and velocity profiles for nondissipative flow

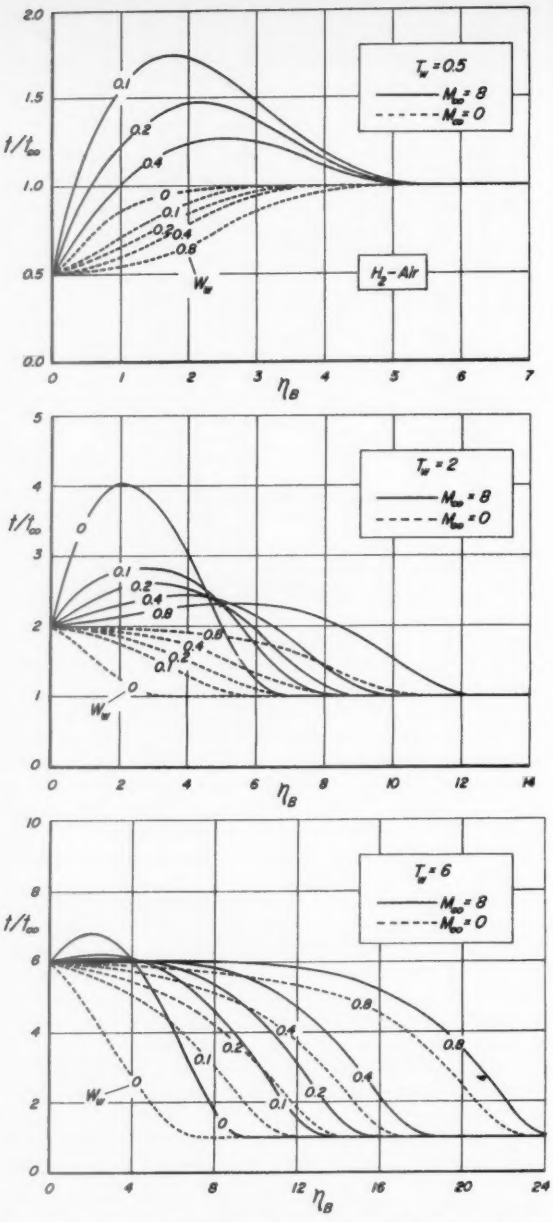

Fig. 6 Temperature profiles for various wall-to-free-stream temperature ratios

wall temperatures, and surface concentrations considered. Results for the adiabatic-wall boundary condition are illustrated in Fig. 7 for $M_\infty = 12$. Note the large increase in η_B. The transport properties at temperature ratios as high as $T = t/t_\infty = 20$ are quite insecure, particularly the mixture conductivity. In practice, the independent parameter may be considered as $f_w = -2\varphi_{\rho_w}(v_w/u_\infty)(\sqrt{Re_x})$ since this fixes the "coolant" flow requirements. The connection between f_w and W_w is given in Fig. 8 for five cases. Evidently the effect of Mach number for a given wall temperature is not very pronounced. Lower injection rates are required at higher Mach numbers to achieve a given surface concentration for the same wall temperature. For constant Mach number the injection rate required for a given surface concentration decreases as the surface temperature increases, the adiabatic wall representing a limiting case.

The local skin-friction coefficients are calculated from the definition $\mu_w(\partial u/\partial y)_w = c_{f_x}(\rho_\infty u^2_\infty/2)$ as $c_{f_x}\sqrt{Re_x} = (\varphi_\mu)_w \left(\frac{\partial(u/u_\infty)}{\partial \eta_B}\right)_w$. These results are shown in Fig. 9 for four Mach numbers and three wall-to-free-stream temperature ratios. Again, the effect of Mach number is small for $T_w > 1$. The reduction in skin friction with hydrogen injection is evidently very pronounced. This decrease is due to the reduction in surface velocity gradient resulting from the change in profile shape (Figs. 4, 5, and 7) and the increased boundary-layer thickness accompanying injection and the diffusion process in the binary flow. The skin-friction coefficient for zero injection ($W_w = 0$) is $c_{f_x} = 0.468/\sqrt{Re_x}$ for $M_\infty = 12$ and $T_w = 6$ (7). Hydrogen injection under the same conditions and at the highest wall concentration in Fig. 9 is seen to reduce this value by approximately 90 per cent.

The local Nusselt numbers required for the calculation of heat transfer $q'' = h(t_r - t_w)$ are derived from the surface temperature gradients as $Nu/\sqrt{Re_x} = (-\varphi_k)_w(dT/d\eta_B)_w/-2(T_w - T_r)$. For $M_\infty = 0$ the recovery temperature is t_∞. The recovery temperature $T_r = t_r/t_\infty$ for $M_\infty = 12$ is shown in Fig. 10 as a function of the injection parameter f_w. The recovery factor may be calculated from these results as $\sigma = 2(T_r - 1)/(\gamma_\infty - 1)M^2_\infty$. Also shown in Fig. 10 are the local Nusselt numbers for three cases. An examination of the results for $M_\infty = 12$ shows that a hydrogen mass concentration of ½ at the surface reduces the local Nusselt number by nearly 70 per cent of its value for pure air at the surface. The hydrogen injection is expected to influence the heat transfer in two ways. Although the higher thermal conductivity of hydrogen relative to air might be expected to increase the heat transfer to the surface at low injection rates, an increase in boundary-layer thickness caused by injection and the

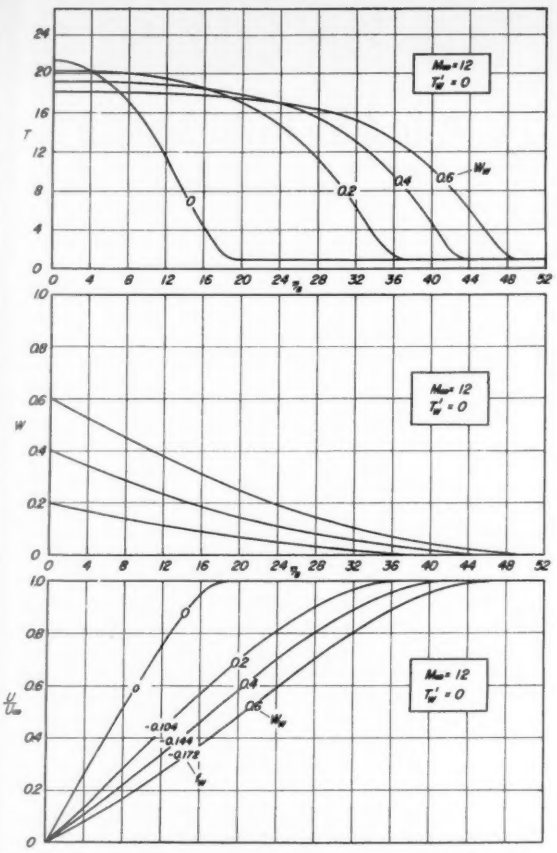

Fig. 7 Temperature, mass concentration and velocity profiles for adiabatic-wall case

higher thermal capacity of hydrogen tend to markedly decrease the heat transfer. The results in Fig. 10 suggest that the last two effects coupled with the lowered density at the surface with hydrogen injection strongly overshadow the conductivity effect.

The use of helium injection, although more attractive from the point of view of application, is known to be more effective than pure air-to-air injection but somewhat less effective than hydrogen-to-air injection. This is a reflection of its higher density and lower thermal capacity relative to hydrogen.[8]

References

1 Eckert, E. R. G., and Schneider, P. J., "Effect of Diffusion in an Isothermal Boundary Layer," *Journal of the Aeronautical Sciences*, Readers' Forum, vol. 23, no. 4, April, 1956, pp. 384–387.

2 Hall, N. A., "Flow Equations for Multicomponent Fluid Systems," *University of Minnesota A.F. Tech. Rept.*, no. 2, August, 1955.

3 Carlson, W. O., and Schneider, P. J., "Transport Properties for Binary Gas Mixtures," *University of Minnesota A.F. Tech. Rept.*, no. 7, January, 1956.

4 Hirschfelder, J. O., Curtis, C. F., and Bird, R. B., "Molecular Theory of Gases and Liquids," *Wiley*, New York, 1954.

5 Keenan, J. H., and Kaye, J., "Gas Tables," Wiley, New York, 1948.

6 Hilsenrath, J., et al., "Tables of Thermal Properties of Gases," *National Bureau of Standards—Circular 564* (U.S. Dept. of Commerce), Nov. 1, 1955.

7 Van Driest, E. R., "Investigation of Laminar Boundary Layer in Compressible Fluids Using the Crocco Method," *NACA TN* 2597, January, 1952.

8 Smith, J. W., "Effect of Diffusion Fields on the Laminar Boundary Layer," *Journal of the Aeronautical Sciences*, vol. 21, no. 3, March, 1954, pp. 154–162.

[8] These investigations are part of a program of theoretical and experimental studies of mass-transfer cooling being carried out at the University of Minnesota under the auspices of the *Air Research and Development Command*, Air Force Contract No. AF-18(600)-1226. The authors also acknowledge their gratitude to Remington Rand Univac Division, St. Paul, Minn., for use of their 1103 facility, and to W. J. Minkowycz for assistance in the numerical calculations.

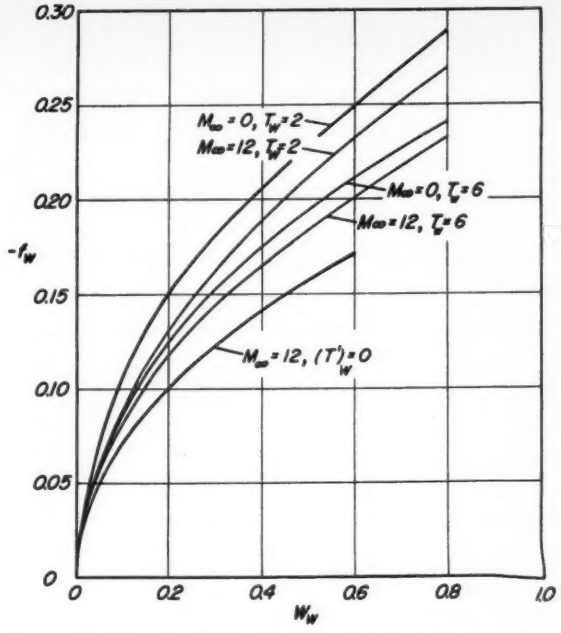

Fig. 8 Variation of wall injection parameter f_w with surface mass concentration W_w

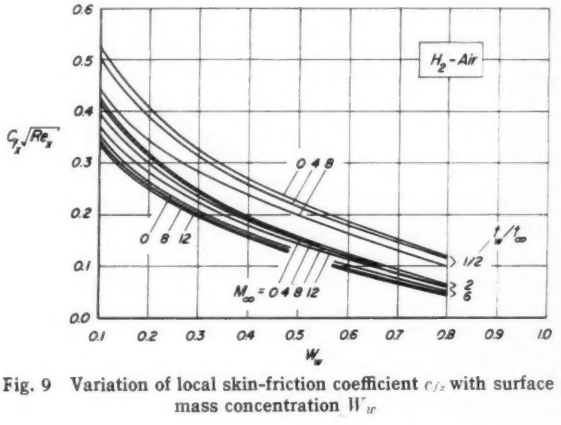

Fig. 9 Variation of local skin-friction coefficient c_{fx} with surface mass concentration W_w

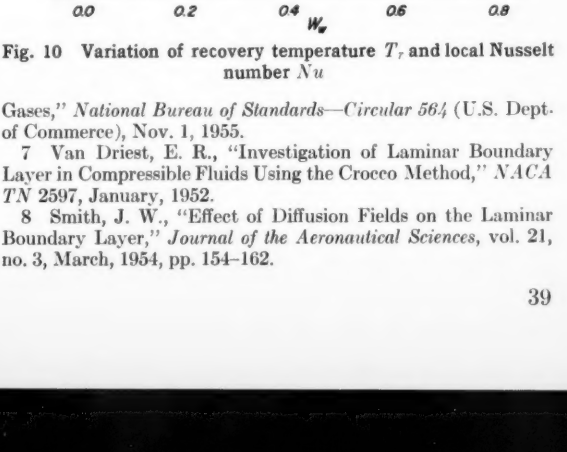

Fig. 10 Variation of recovery temperature T_r and local Nusselt number Nu

The Temperature History in a Thick Skin Subjected to Laminar Heating During Entry into the Atmosphere

GEORGE W. SUTTON[1]

General Electric Company, Philadelphia, Pa.

During high speed entry into the earth's atmosphere, a vehicle can be afforded thermal protection for the short period of entry heating by a thick outer skin, sometimes called a "heat sink." The temperature distribution in such a heat sink has been found by integrating the product of the laminar aerodynamic heating rate and the appropriate Green's function for a finite-thickness wall over the generalized trajectory for a vehicle entering the earth's atmosphere at high speeds. The result is given in closed form, thus solving completely the one dimensional heat conduction problem for laminar heating. The maximum surface temperature that occurs during the generalized entry trajectory for any combination of wall thickness and thermal properties is obtained. This maximum temperature is given by a single dimensionless curve, from which the performance of any material can be found, provided that the average thermal properties may be used. As an example of the use of the solution, the performance of copper, graphite, molybdenum and tungsten are compared.

Nomenclature

a = a constant, taken as 13/4
A = reference area of vehicle
B = a constant, taken as 20,800 Btu/ft-sec °F
C_D = hypersonic drag coefficient
C_{ph} = specific heat of heat sink material
C = constant
G = Green's function
g = 32.2 ft/sec²
H = 21,400 ft
h = stagnation enthalpy of air, Btu/lb
h_e = stagnation enthalpy of air at edge of boundary layer, Btu/lb
k_h = thermal conductivity of heat-sink material, Btu/ft²-sec
L = heat sink thickness
q = heat transfer rate, Btu/ft²-sec
Q_T = total heat pulse per unit area, Btu/ft²
r = dummy of integration
R = radius of curvature of vehicle at stagnation point, ft
V = velocity, ft/sec
V_s = sea level satellite velocity, ft/sec
V_e = entry velocity, ft/sec
T = temperature, deg F
t = time, sec
w = weight of heat sink per square foot of exposed area
W = weight of entry vehicle, lb
x = distance from heat sink outer surface, ft
y = altitude, ft
Z = $y - y_m$, ft
α_h = thermal diffusivity of heat sink material, ft²/sec
β = $H\rho_0 g C_D A/2W \sin\theta$
γ = $\pi\sqrt{\alpha_h H}/L\sqrt{V_e \sin\theta}$
ϵ_h = emissivity of heat sink surfaces
θ = entry flight path angle, measured from horizontal
σ = Stephan-Boltzmann constant
ϕ = $(T - T_0)\sqrt{k_h\rho_h C_{ph} V_e \sin\theta}/q_m\sqrt{H}$
ρ = density of air, slug/ft³
ρ_0 = sea level density of air, slug/ft³
ρ_e = 0.00363 slug/ft³
ρ_h = weight density of heat sink material, lb/ft³
τ = dimensionless time, $(V_e \sin\theta)t/H$

Subscripts

h = heat sink material
m = maximum

Received July 5, 1957.

[1] Research Engineer, Missile and Ordnance Systems Dept.

Introduction

WHEN a vehicle enters the earth's atmosphere at high speed, it is necessary to protect the vehicle structure from the intense aerodynamic heating that exists for a short period of time. One possible protection scheme is the use of a thick outer skin on that portion of the vehicle that is subjected to the intense heating, thus allowing the heat energy to be absorbed by the temperature rise of the skin. This thick skin, sometimes called a "heat sink," is thermally insulated from the vehicle structure.

In principle, the maximum energy that such a heat-sink can absorb is just

$$Q_T = \int_{T_0}^{T_m} L\rho_h C_{ph}(T)dt$$

per unit area, if the problem of heat conduction is ignored. However, this cannot be achieved in practice, because the heat energy takes a finite time to be conducted from the heated face of the heat sink to the insulated back face; hence during the heating cycle, the temperature of the former will be greater than that of the latter. This problem was originally considered by Wagner (1),[2] but was limited to two simple cases: Constant velocity with a finite wall, and an approximate trajectory with a semi-infinite wall thicknesses. Mason and Gazley (2) have also considered this problem.

Herein, a method will be developed for determining the temperature profile in a heat sink of arbitrary thickness, and the maximum surface temperature that will be reached during a complete entry trajectory. Numerical results are presented in the form of a single curve which relates the maximum wall temperature to the maximum heating rate, and which also includes the effect of trajectory, material properties and wall thickness. The heat sink capabilities of several materials are calculated from this curve.

The following assumptions were made: The material properties are represented by their average values; the wall thickness is small in comparison to the radius of curvature of the outer contour of the heat sink; and the meridional variations of heat sink thickness and heating rate are small, so that the heat flow is essentially one-dimensional from the heated front face to the insulated backface.

Entry Trajectory

During the entry into the earth's atmosphere of a high speed vehicle, the deceleration is large in comparison to gravity.

[2] Numbers in parentheses indicate References at end of paper.

Hence gravity can be neglected. With this assumption, the flight path angle during entry will remain constant while the actual trajectory is slightly curved. Also, the calculated values of time will have an error which increases with decreasing altitude. However, at the time of maximum wall temperature, which is the region of interest, these errors are small and are within the accuracy of analysis. The equation of motion of the vehicle along the flight path is then

$$-\tfrac{1}{2}C_D A\rho V^2 = \frac{W}{g}\frac{dV}{dt} \quad \ldots [1]$$

Since the flight path angle is taken constant

$$\frac{dV}{dt} = \frac{dV}{dy}\cdot\frac{dy}{dt} = \frac{-\sin\theta}{2}\frac{d}{dy}(V^2) \quad \ldots [2]$$

The density can be approximated by an exponential, that is

$$\rho = \rho_e e^{-y/H} \quad \ldots [3]$$

For $\rho_e = 0.00363$ slugs/ft^3 and $H = 21{,}400$ ft, the maximum error in ρ is six per cent compared to the standard atmosphere, but this is well within the experimental error of density determination at high altitudes, for altitudes up to 200,000 ft.

Since at hypersonic velocities C_D is a constant, Equation [1] can be integrated to obtain the vehicle velocity V as a function of altitude by use of Equations [2 and 3] as follows

$$V = V_e e^{-\beta e^{-y/H}} \quad \ldots [4]$$

where

$$\beta = \frac{H\rho_e g C_D A}{2W\sin\theta} \quad \ldots [5]$$

To obtain time as a function of altitude, note that $V = -(dy/dt)/\sin\theta$ and integrate [4] to obtain

$$t = \frac{H}{V_e\sin\theta}\left[\frac{-y}{H} + \beta^{-y/H} + \frac{\beta^2 e^{-2y/H}}{2\cdot 2!} + \frac{\beta^3 e^{-3y/H}}{3\cdot 3!} + \cdots\right]_{y_m}^{y} \quad \ldots [6]$$

where $t = 0$ is chosen to correspond to that altitude y_m at which the convective heat transfer is a maximum. Equations [4] and [6] are derived in (1); however, later in this analysis, it will be convenient to neglect terms in the series higher than $\beta\exp(-y/H)$. At the altitudes of greatest heating, the error so introduced is negligible; at lower altitudes, where the heating rate is 10 per cent of maximum, the error in time is less than 20 per cent. The net effect of this assumption is negligible.

Heat Transfer Rate

In the vicinity of the stagnation point of a blunt-nosed hypersonic vehicle the boundary layer will be laminar, in which case the convective heat transfer rate at the stagnation point may be approximated by (3)

$$q = B\left(\frac{R_0}{R}\frac{\rho}{\rho_0}\right)^{1/2}\left(\frac{V}{V_e}\right)^a\left(1 - \frac{h_w}{h_e}\right) \quad \ldots [7]$$

Equation [7], when compared to the results of a similarity solution of the laminar boundary layer equations, is accurate to within five per cent for the following values of the constants: $B = 20{,}800$ btu/ft^{2}sec, $R_0 = 1$ ft, and $a = 13/4$, according to (3). At points on the body other than at the stagnation point, the heating rate at large Mach numbers is given by

$$q = Cq_{st\,pt} \quad \ldots [8]$$

Methods for determining C, which is primarily a function of geometry, are contained in (4). However, in the following analysis, the heating cycle to a point on the body will be normalized to the maximum heating rate at that point and, hence Equation [8] will have no effect upon the results. Thermal radiation from the shock layer to the vehicle will be neglected; this is permissible if the vehicle skin is plated with a material of low absorptivity, or if the convective heat transfer is much larger than the shock layer radiation.

In the relations to be derived, it is assumed that $h_w/h_e \approx 0$; the results, however, are applicable for cases where ϵ_h and h_w/h_e are not negligible, by calculating q_m as follows

$$q_m = \left[B\left(\frac{R_0}{R}\frac{\rho}{\rho_0}\right)^{1/2}\left(\frac{V}{V_e}\right)^a\left(1 - \frac{h_w}{h_e}\right) - \sigma\epsilon_h T_w^4\right]_m \quad \ldots [9]$$

This approximation is valid when the correction to q_m is small; this is true because the heating cycle including radiation from the surface, when normalized against q_m as given by Equation [9], is virtually the same as the heating cycle given by Equation [7], when $h_w/h_e \approx 0$. Hence q_m is obtained by iteration on the value of T_w, for which an expression is derived later.

Heating Cycle

When Equations [3 and 4] are substituted into [7], the heating rate as a function of altitude is obtained

$$q = B\left(\frac{R_0}{R}\frac{\rho_e}{\rho_0}\right)^{1/2}\left(\frac{V_e}{V_e}\right)^a e^{-(y/2H + a\beta e^{-y/H})} \quad \ldots [10]$$

By differentiating [10] with respect to y, the altitude, y_m, at which the heating rate is a maximum is obtained

$$y_m = H\ln(2a\beta) \quad \ldots [11]$$

which corresponds to a velocity of

$$V = V_m = V_e e^{-1/2 a} \quad \ldots [12]$$

If $a = 13/4$, then $V = 0.858V_e$. Thus the maximum heating rate occurs before the vehicle has slowed down appreciably. The maximum heating rate is obtained from the substitution of Equation [11 and 5] into [10]

$$q_m = B\left(\frac{R_0}{\rho_0}\cdot\frac{W}{C_D A R}\cdot\frac{\sin\theta}{age H}\right)^{1/2}\left(\frac{V_e}{V_e}\right)^a \quad \ldots [13]$$

To simplify the equations, normalize [10] by dividing it by [13] and by measuring altitude from the altitude of maximum heating; that is, let

$$y - y_m = Z \quad \ldots [14]$$

The following expression for the normalized heat transfer is then obtained

$$\frac{q}{q_m} = e^{-1/2(Z/H - 1 + e^{-Z/H})} \quad \ldots [15]$$

Hence the normalized heat transfer rates in terms of Z are identical and are independent of the value of a. This same result has been obtained (5) for $a = 3.0$. It is instructive to determine whether a similar relation exists for time. The substitution of Equations [11 and 14] into [6] yields

$$\tau = \frac{V_e\sin\theta}{H}t = -\frac{Z}{H} - \frac{1 - e^{-Z/H}}{2a} - \frac{1 - e^{-2Z/H}}{2\cdot 2!(2a)^2} - \frac{1 - e^{-3Z/H}}{3\cdot 3!(2a)^3} - \ldots [16]$$

Thus, time scales proportionally to the vertical component of the entry velocity, where for convenience a dimensionless time is defined as

$$\tau = \frac{V_e\sin\theta}{H}t \quad \ldots [17]$$

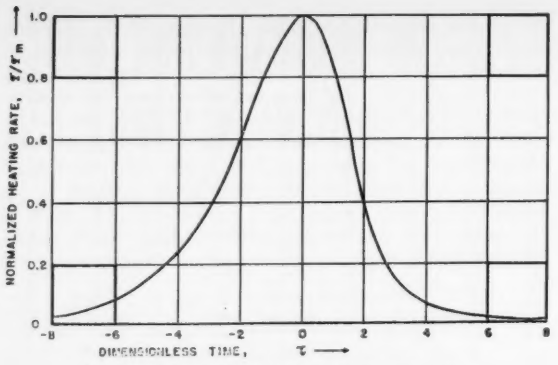

Fig. 1 Convection heating rate during entry

Equations [15] and [16] are a parametric representation of q/qm vs. τ, which is independent of missile weight, drag, or trajectory. This is shown in Fig. 1, for $a = 13/4$.

The ratio of the total heat transfer to the maximum heat transfer rate can be obtained from an integration of Equation [15]

$$\frac{Q_T}{q_m} = \int_{-\infty}^{t} \frac{q}{q_m}\, dt = \int_{\infty}^{-y_m} \frac{q}{q_m} \cdot (Z)\, \frac{dt}{dZ}\, (Z) dZ \ldots . [18]$$

Note that $dt/dZ = -1/V \sin \theta$, and substitute Equations [4 and 5] into [16] to obtain

$$\frac{Q_T}{q_m} = \frac{H}{V_e \sin \theta} \left(\frac{2ae\pi}{a-1} \right)^{1/2} \cdot \operatorname{erf}[\beta(a-1)]^{1/2} \ldots . [19]$$

Since $\beta > 1$, erf $[\beta(a-1)]^{1/2} \approx 1$. As an example, a vehicle with an entry velocity of 30,000 fps, and flight path angle of 80 deg has a ratio of Q_T/q_m of 3.60. The following explicit expression for Q_T is obtained by substitution of Equation [13] into [19]

$$Q_T = \frac{B}{V_e} \left(\frac{2\pi}{a-1} \cdot \frac{H}{\sin \theta} \cdot \frac{R_0}{\rho_0} \cdot \frac{W}{C_D A} \cdot \frac{1}{gR} \right)^{1/2} \left(\frac{V_e}{V_s} \right)^a \ldots [19a]$$

Maximum Temperature for Back Radiation

Before proceeding to the calculation of the heat conduction into the skin of the vehicle, one may inquire as to whether it is possible to radiate all of the convective heating from the vehicle skin. As a first approximation, the heat capacity of the skin is neglected. Then q_m as given by Equation [13] may be equated to $\sigma \epsilon_h T_w^4$. This procedure neglects h_w/h_e; thus the calculated values of T_w will be somewhat too high. The resulting dependence of T_w on $W/C_D AR$ and entry angle is shown in Fig. 2. It may be seen that a small entry angle which decreases the convective heating, and a refractory material which increases the radiation, are highly desirable. Note that relatively heavy entry bodies with large entry bodies can back-radiate the convective heat transfer if the outer shell is made of a refractory material with very high temperature stability.

For a given body and trajectory one may obtain a more precise value of T_w by correcting the convective heating with the factor $1 - \frac{h_w}{h_e}$, see Equation [9]. The value of h_e may be obtained from normal shock calculations (6) for the value of V_m and y_m of that trajectory; the value of h_w may be obtained from the value of the stagnation pressure behind the shock and, as a first approximation, the value of T_w as obtained from Fig. 2. The corrected value of q_m is then equated to $\sigma \epsilon_h T_w^4$ and solved for T_w.

Back radiation appears to be practical only for light bodies with shallow entry angles. In the remainder of this paper, back radiation will be neglected, but the thermal capacity of the skin will be included; this corresponds to large entry

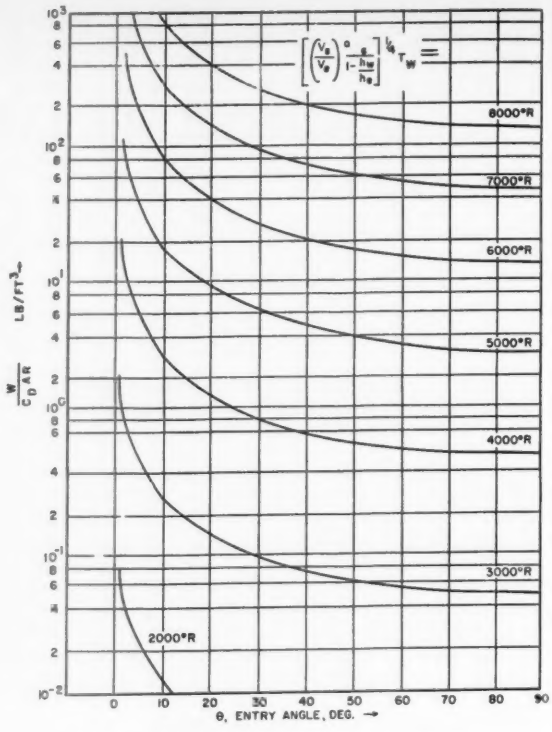

Fig. 2 Surface temperature for back radiation

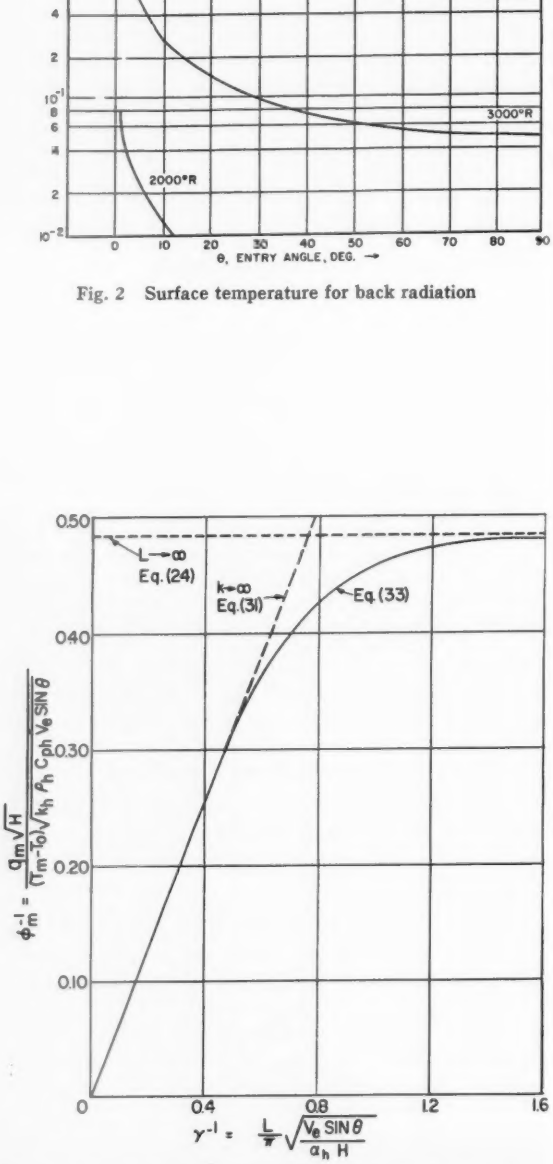

Fig. 3 Effect of trajectory and heat sink properties on heat sink maximum temperature

angles, high entry velocities, and temperature rises which are much smaller than that required for back radiation. As an introduction to the method, two limiting cases are derived: The temperature rise of a very thin wall, and the temperature rise of a semi-infinite wall.

Maximum Temperature of a Thin Wall

The calculation for the temperature of a thin walled heat sink is simple, for as $L \to 0$, $T(x, t) \to T_w$, hence

$$T_m - T_0 = Q_T / L\rho_h C p_h \quad [20]$$

Substitution of Equation [19] into [20] yields

$$T_m - T_0 = \frac{q_m H}{L\rho_h C p_h V_e \sin\theta}\left(\frac{2ae\pi}{a-1}\right)^{1/2} \quad [21]$$

It is convenient to define a new independent variable, which reflects the wall thickness, as

$$\gamma = \frac{\pi}{L}\left(\frac{\alpha_h H}{V_e \sin\theta}\right)^{1/2} \quad [22]$$

and a new dependent variable which is a measure of the temperature rise of the wall as

$$\phi(\gamma, Z) = \frac{T(Z) - T_0}{q_m}\left(\frac{k_h \rho_h C p_h V_e \sin\theta}{H}\right)^{1/2} \quad [23]$$

Then equation [21] becomes

$$\phi_m(\gamma) = \gamma\left[\frac{2ae}{\pi(a-1)}\right]^{1/2} \quad [24]$$

for a thin wall. Equation [24] is shown in Fig. 3, as "$k \to \infty$."

A thin wall usually does not have sufficient heat capacity to absorb the aerodynamic heating without surface melting. To prevent surface melting, the heat sink must be sufficiently thick, in which case the thin-wall approximation is inadequate. The limiting case occurs when the back face experiences zero temperature increase; this corresponds to semi-infinite thickness, which is considered next.

Maximum Surface Temperature of a Semi-Infinite Wall

The heat sink that can absorb the aerodynamic heating with the least surface temperature rise is sufficiently thick so that the back insulated side experiences little or no temperature rise. Hence, for the purpose of mathematical analysis, it is permissible to let $L \to \infty$; then calculated the temperature response of this wall and also the value of x for which the temperature rise is negligible when the surface temperature passes through its maximum. This value of x is called the semi-infinite thickness.

The surface temperature is calculated as follows: consider a unit amount of heat transferred to the wall at $x = 0$ at time t_1; the temperature distribution at some later time t is given by the following Green's function (7)

$$G(x, t - t_1) = \frac{e^{-x^2/4\alpha_h(t-t_1)}}{\sqrt{k_h\rho_h C p_h \pi (t - t_1)}} \quad [25]$$

Since the heat conduction equation is linear, the temperature T_w at $x = 0$ due to a heating rate $q(t)$ is given by

$$T_w = \frac{1}{\sqrt{k_h\rho_h C p_h \pi}}\int_{-\infty}^{t} \frac{q(t_1)}{\sqrt{t - t_1}}\, dt_1 \quad [26]$$

The factor $t - t_1$ is obtained from Equations [6 and 11] by taking only the first two terms as follows

$$t - t_1 = \frac{H}{V_e \sin\theta}\left[\frac{\zeta}{H} - \frac{Z}{H} + \frac{1}{2a}\left(e^{-Z/H} - e^{-\zeta/H}\right)\right] \quad [27]$$

where $Z = y - y_m$, and ζ is the altitude corresponding to t_1. By use of the relationship $\frac{dy}{dt} = -V \sin\theta$ and Equation [4], dt_1 becomes

$$dt_1 = -\frac{e^{\frac{1}{2}ae^{-\zeta/H}}}{V_e \sin\theta}\, d\zeta \quad [28]$$

and from Equation [15]

$$q(t_1) = q_m e^{-\frac{1}{2}(\zeta/H - 1 + e^{-\zeta/H})} \quad [29]$$

To simplify notation, let

$$\zeta/H - Z/H = r \quad [30]$$

Substitution of Equations [27–30] into Equation [26] and the definition of [23] yield

$$\phi = \frac{e^{\frac{1}{2}\frac{1}{2}(1 - Z/H)}}{\pi^{1/2}}\int_0^{\infty} \frac{e^{-\left[\frac{r}{2} + \frac{a-1}{2a}e^{-(Z/H + r)}\right]}}{\sqrt{r + \frac{1}{2a}e^{-Z/H}(1 - e^{-r})}}\, dr \quad [31]$$

where $r = \zeta/H$ is the dummy of integration.

The independent variable γ does not appear in Equation [31] because $\gamma \to 0$ as $L \to \infty$. The integral in Equation [31] has been evaluated by means of a digital computer. The maximum value ϕ_m is 2.06 for $a = 13/4$, and occurs when $Z/H = -0.80$. This value of $\gamma = 0$ gives the maximum amount of energy that a given material can absorb for a given temperature rise. Equation [31] is shown in Fig. 3 as "$L \to \infty$."

Since it is usually desirable to have as thin a heat sink as possible in order to conserve weight, the wall thickness may be less than the semi-infinite thickness. The limitation on L depends on the maximum allowable temperature rise. In the next section, this dependence is derived.

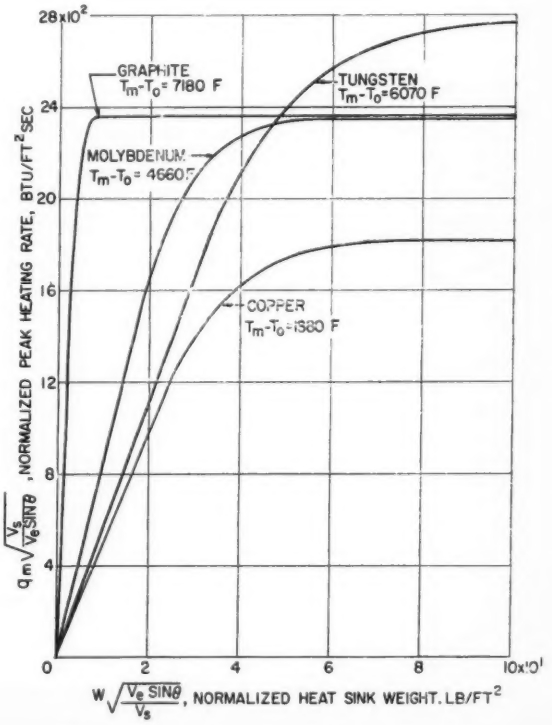

Fig. 4 Heat sink capacities of several materials

Maximum Temperature of a Heat Sink of Arbitrary Thickness

Although it is possible to correct Equation [31] for the case of a finite wall thickness by considering "reflections" of the heat at the insulated back face, the problem can be solved directly by using the Green's function for a wall of thickness L. It is easily shown that the Green's function is given by

$$G(x, t - t_1) = \frac{1}{\rho_h C p_h L}\left[1 + 2\sum_{n=1}^{\infty} \cos\frac{n\pi x}{L}\, e^{-n^2\pi^2\alpha_h^2(t-t_1)/L}\right] \quad \ldots\ldots\ldots\ldots\ldots\ldots [32]$$

The temperature rise is obtained in a similar manner to Equation [31]. By the use of the definitions of ϕ and γ and Equations [22, 23], this becomes

$$\phi(x, \gamma, Z) = \frac{T(x, Z) - T_0}{q_m}\sqrt{\frac{k_h\rho_h C p_h V_e \sin\theta}{H}} = \gamma\sqrt{\frac{2ae}{\pi(a-1)}} \times \operatorname{erf}\sqrt{\frac{a-1}{2a}}\, e^{-Z/H} + \frac{2\gamma}{\pi}\, e^{\frac{1}{2}(1-Z/H)} \times \int_0^{\infty} e^{-\left[\frac{r}{2} + \frac{a-1}{2a}e^{-(Z/H+r)}\right]} \times \sum_{n=1}^{\infty} \cos\left(\frac{n\pi x}{L}\right) e^{-n^2\gamma^2\left[r + \frac{1}{2a}e^{-Z/H(1-e^{-r})}\right]}\, dr \ldots [33]$$

Because of the complex way in which γ and Z appear in Equation [33], there exists no generalized temperature curve which isolates the effect of γ. Hence $\phi(Z)$ was calculated at $x = 0$ with a digital computer for various values of γ, with $a = 13/4$; and the maximum values $\phi_m(\gamma)$ were obtained.

The results are shown in Fig. 3. It is seen that, if $\gamma < 0.75$, the results correspond to an "infinite" heat sink; while if $\gamma > 2.0$, the heat conduction through the wall can be neglected and only the heat capacity of the heat sink need be considered.

From Fig. 3, the maximum heat sink temperature for any thickness of any material can be found, provided that the thermal properties of that material can be represented by temperature-averaged values. First the value of γ is calculated and from Fig. 3 the value of ϕ_m is obtained. Then, by the use of the value of q_m for that trajectory, $T_m - T_0$ is obtained by means of Equation [23]. On the other hand, if the maximum temperature rise is specified, the required heat sink thickness L can be obtained. A practical upper limit to the thickness corresponds to $\gamma = 0.75$.

To illustrate more fully the use of Fig. 3, the heat absorption capacities of four different materials have been obtained and are shown in Fig. 4. The weight per square foot has been obtained by multiplying L by the weight density of that material. These calculations neglect the effect of surface combustion; this may be permissible if the convective heating rate is much larger than the rate of energy release due to combustion. The thermal properties of the four materials are shown in Table I.

It may be seen from Fig. 4 that tungsten is capable of absorbing the greatest amount of heat. For maximum heating rates which are somewhat less, a shell fabricated of graphite will weigh the least. Copper is limited to a maximum heating rate of 1818 $[V_e \sin\theta/V_*]^{1/2}$ Btu/ft²-sec. The calculated capacity of copper agrees to within 5 per cent of a Dusinberre numerical calculation of the temperature rise, using an actual trajectory.

The altitudes corresponding to the maximum heat sink surface temperatures are shown in Fig. 5. Since $Z = y - y_m$, the maximum temperature always occurs after the maximum heat transfer.

For an actual trajectory, $T_m - T_0$ and q_m are interdependent but the following iteration scheme may be used to find the temperature increase: The zero approximation of q_m is calculated, assuming $T_m - T_0 = 0$. With $q_m(0)$, the zero approximation for $T_m(0)$ is obtained from Fig. 3. Since the $T_m(Z)$ curve is flat in the vicinity of $Z = 0$, assume that the surface temperature at $Z = 0$ is $T_m(0)$. Then $q_m(1)$ is calculated from Equation [9], and the first approximation $T_m(1)$ is again obtained from Fig. 2. This process converges rapidly because of the small dependence of q_m on T_m.

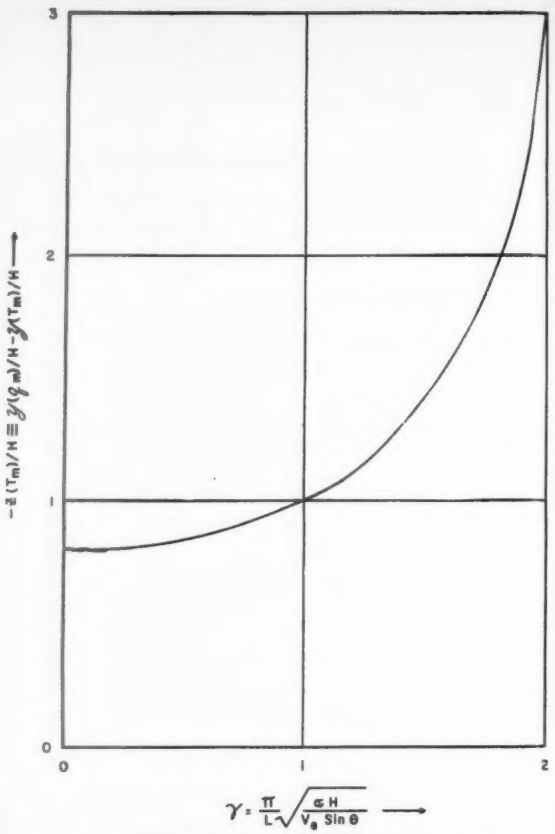

Fig. 5 Altitude of maximum surface temperature

Temperature Profiles

The temperature profiles at various times in a wall for which $\gamma = 1.245$ are shown in Fig. 6. These were obtained from Equation [33]. They illustrate the fact that the back face of

Table I Selected Physical Properties

Material	Temperature at which evaluated deg F	k Btu/ft sec F	ρ lb/ft³	C_p Btu/lb
Copper[1]	1112	0.0567	545	0.1057
Graphite[2]	1472	0.0106	105	0.344
Tungsten[3]	2192	0.0162	1204	0.0377
Molybdenum[4]	2192	0.0189	638	0.075

[1] W. H. McAdams. "Heat Transmission," 3rd Edition, McGraw-Hill, 1954.
[2] Courtesy V. C. Hamister, National Carbon Company.
[3] I. C. T. and "Handbook of Chemistry and Physics," 33rd Edition, p. 1875.
[4] "Metals Handbook," 1948.

the heat sink reaches temperatures almost as high as the heated side. Note that the value of ϕ is 2.30, which is only 10 per cent greater than the infinite-wall value of 2.06 and yet the infinite-wall approximation cannot be used to predict the temperature profiles correctly.

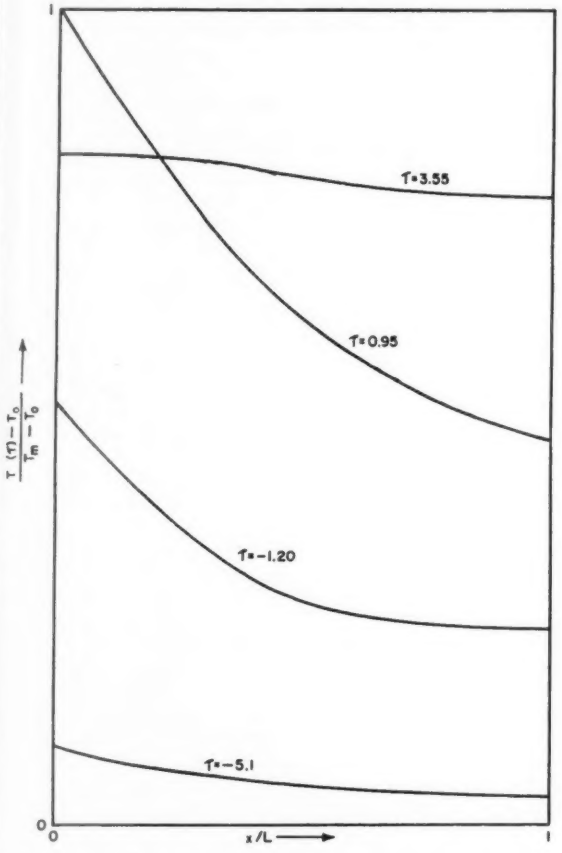

Fig. 6 Heat sink temperature profiles at various times for $\gamma = 1.245$

Conclusions

By use of the Green's function for heat conduction, the temperature distribution in a heat sink has been found in closed form, thus solving completely the one-dimensional heat conduction problem for a laminar boundary layer. The values obtained are five per cent lower than a Dusinberre calculation for an exact trajectory.

The maximum surface temperature has been calculated in dimensionless form for any trajectory. A calculation of a temperature profile history shows the inadequacy of the semi-infinite slab solution. The heat sink capacities, which are easily found from the analysis, have been calculated for several different materials.

The accuracy of the solution depends on the accuracy of the expression for the heat transfer rate. The solution is applicable to a laminar boundary layer and one-dimensional heat conduction. It is possible to extend the method for the case of the turbulent boundary layer and for axially-symmetric heat conduction.

Acknowledgments

The author expresses his appreciation to Sylvan H. Green for formulating the calculation of the various integrals and to the members of the digital computing staff of the Missile and Ordnance Systems Dept. of General Electric Co. for carrying out the computations.

References

1 Wagner, C., "Skin Temperature of Missiles Entering the Atmosphere at Hypersonic Speed," TR 60, Ordnance Research and Development Div., Suboffice (Rocket) Ft. Bliss, Tex., Sept. 1949.

2 Mason, D. J., and Gazley Jr., C., "Surface Protection and Cooling System for High Speed Flight," presented at the National Summer Meeting of IAS June 1956.

3 Kemp, N. H., and Riddell, F. R., "Re-entry Heat Transfer to Satellite Vehicles," Jet Propulsion, vol. 27, part 1, Feb. 1957, pp. 132-137, 147.

4 Lees, L., "Laminar Heat Transfer Over Blunt-Nosed Bodies at Hypersonic Flight Speeds," Jet Propulsion, vol. 26, April 1956, pp. 259–269.

5 Allen, H. J., and Eggers Jr., A. J., "A Study of the Motion and Aerodynamic Heating of Missiles Entering the Earth's Atmosphere at High Supersonic Speeds," NACA RM A53 D28, Aug. 25, 1953, (Unclassified).

6 Logan Jr., J. G., "Normal Shock Calculations in Air," Cornell Aeronautical Laboratories, Jan. 1957.

7 Carlsaw, H. S., and Jaeger, J. C., "The Conduction of Heat in Solids," Oxford 1947.

Factors Which Influence the Suitability of Liquid Propellants as Rocket Motor Regenerative Coolants

D. R. BARTZ[1]

Jet Propulsion Laboratory, California Institute of Technology, Pasadena, Calif.

A brief review of methods of utilizing liquid propellants as rocket-motor coolants is given, and criteria for acceptable cooling are established. Methods of analytical and experimental determination of the pertinent heat-transfer characteristics of propellants are described. The measured maximum rates at which liquid ammonia can satisfactorily accept heat are presented to show typical trends with variations of fluid pressure, temperature and velocity. Measured maximum rates for several propellants are compared with predictions of heat fluxes from the combustion gases of these propellants when producing the same thrust in a hypothetical rocket motor. From this comparison, an insight into the importance of various propellant properties and operating conditions is gained.

Nomenclature

c^*	=	characteristic velocity, ft/sec
Dep	=	deposition
FC	=	forced convection without boiling
I_{sp}	=	specific impulse, sec
L^*	=	characteristic length, in.
NB	=	nucleate boiling
p	=	pressure
q	=	heat flux, Btu/in.^{2} sec
q_{ul}	=	heat flux at the upper limit of nucleate boiling, Btu/in.^{2} sec
r	=	mixture ratio, oxidizer to fuel by weight
t	=	height of coolant-passage annulus, in.
T	=	temperature
V	=	coolant velocity, ft/sec
W	=	coolant flow rate, lb/sec
Δp	=	coolant-passage pressure drop
$\Delta p_{q=0}$	=	coolant-passage pressure drop without heat transfer
μ_w/μ_b	=	ratio of viscosity at the wall to that in coolant-passage free stream

Subscripts

c	=	chamber
L	=	bulk
out	=	coolant-passage outlet
sat	=	saturation
w	=	wall
*	=	at the nozzle throat

Introduction

A MAJOR problem confronting the designers of long-duration liquid-propellant rocket systems is designing motor walls compatible with the extreme temperatures resulting from the combustion. Three methods for achieving the desired resistance to the high temperatures are commonly considered. They are refractory liners, regenerative cooling and film or transpiration cooling. Of the three, regenerative cooling is most commonly utilized in propulsion systems currently in production or development. Regenerative cooling is accomplished by flowing one or both propellants through motor-wall coolant passages on their way from the propellant tanks to the injector. The missile performance penalty of regenerative cooling is the additional turbo-pump weight and power consumption or additional gas pressurization required to overcome the coolant passage pressure drop. In order to select the method best suited for a contemplated design, this penalty must be compared with the additional dead weight and fabricational difficulties associated with refractory liners and with the penalty of additional propellant consumption associated with film or transpiration cooling. The limitations of each of these methods are such that for extremely high-performance motors, optimal combinations of all three methods may be necessary. This paper presents and discusses the factors which determine the suitability of a given propellant as the coolant for a completely regeneratively cooled motor.

The criterion for adequate cooling is simply that the coolant flow must maintain the walls of the motor at temperatures below which failure might occur due to melting and/or stress. For metals commonly used for rocket motor walls, such as stainless steel, nickel, inconel, or mild steel, the limiting combustion side surface temperature is in the region from 1500 to 2000 F. Thus, with combustion temperatures from 3000 to 8000 F, resultant differences between the free-stream gas temperature and the wall temperature are from 1500 to 6000 F. The consequence of such high driving potentials are heat fluxes to the wall, which, in units of Btu/in.^{2} sec, range from about 1 to 20. Such fluxes are orders of magnitude higher than those encountered in conventional heat exchange equipment and even significantly higher than encountered in most nuclear reactors.

These high levels of heat flux in conjunction with conditions of coolant velocity, temperature, and pressure are such that, over most of the cooled surface, heat is transferred by boiling when the pressure of the system is below the critical pressure of the coolant. Some coolants, however, are necessarily operated at pressures above their critical pressure; hence, both the boiling and supercritical heat-transfer characteristics of a wide variety of liquids are of interest in connection with rocket-motor regenerative-cooling applications. A qualitative description of the characteristics of the various pertinent regimes of heat transfer and the methods utilized for theoretical and experimental evaluation of these characteristics will serve to define terms and to introduce the problems involved. Such descriptions are best illustrated by a plot of heat flux as a function of wall temperature for constant pressure bulk temperature, and velocity, Fig. 1.

Considering first a liquid at a pressure below its critical pressure, and a bulk temperature well below its saturation temperature, the line segment A-B represents the range of heat fluxes which can be sustained without boiling. The wall temperature at B exceeds the saturation temperature by anywhere from 10 to 100 F, which constitutes superheating of the liquid. At heat fluxes slightly higher than B, a few bubbles are formed at favored nucleation spots on the hot wall, and they grow rapidly out into the cold-liquid stream. They continue to grow until condensation at the cold-liquid surface

Presented at the ARS Spring Meeting, Washington, D. C., April 4–6, 1957.

[1] Research Group Supervisor, Power Plant Research Section.

begins to exceed the rate of vaporization at the base of the bubble, whereupon the bubbles begin to collapse. The inertia of the fluid following the collapsing bubble is responsible for completely collapsing the bubble. This process, which occurs at exceedingly high frequencies, is called nucleate or surface boiling. As still higher heat fluxes are encountered in the region *B-C*, an increasing number of nucleation sites are brought into play, thus increasing the bubble population. This is accomplished with only slight increases in wall temperature. The resulting increase in heat-transfer coefficient represented by the near vertical part of the curve (*B-C*) is believed by many, although not unanimously (1),[2] to be the result of increasing turbulent mixing or stirring created by the growth and collapse of the bubbles. Unfortunately, this favorable situation has a limit. At this limit *C*, a slight increase in the heat flux leads to such a dense bubble population that the bubbles coalesce into a vapor film with an attendant large decrease in heat transfer coefficient. The resulting shift in wall temperature, *C-D*, is for many liquids so high that failure of commonly employed metal surfaces occurs. Hence, this transition from nucleate to film boiling has been used synonymously with the term burnout. However, for many other liquids, notably light hydrocarbons and alcohols, the temperature at *D* is not much above 1000 F, and failure does not occur. Thus, the term burnout becomes misleading. To avoid this difficulty, point *C* shall be referred to as the upper limit of nucleate boiling with the symbol q_{ul}. At heat fluxes above *C*, even for liquids which do not cause failure, the wall temperature increases rapidly with increases in heat flux (*D-E*) so that for practical purposes the value of the heat flux at the upper limit of nucleate boiling must be used as the design limit for regenerative cooling systems.

The picture for supercritical pressure liquids is much simpler. Since no boiling can occur, the wall temperature increases monotonically with increasing heat flux (*F-G*), the heat-transfer coefficient remaining essentially constant until the wall temperature reaches the critical temperature. At higher heat fluxes (*G-H*), the heat is transferred through a gaseous layer adjacent to the hot wall, resulting in somewhat lower heat-transfer coefficients. Failure temperatures are usually reached at much lower heat fluxes when a liquid is operated above its critical pressure than when operated below its critical pressure.

Determination of Heat-Transfer Characteristics

Analytical Methods

The relationship between heat flux and wall temperature, i.e., the heat-transfer coefficients, in the nonboiling, subcritical temperature regions of both subcritical and supercritical pressure liquids (*A-B* and *F-G* of Fig. 1) can be predicted with sufficient accuracy for design purposes by the Sieder-Tate equation (2). The data for a wide variety of liquid propellants have been well-correlated by this equation. It has successfully predicted the effects of pressure, velocity and bulk temperature. The principal difficulty in applying this equation to new propellants is the need of values of the transport properties, viscosity and thermal conductivity. They generally cannot be predicted from theory. While measurement of viscosity is a rather simple laboratory procedure, measurement of thermal conductivity of liquids is considerably more difficult.

The wall temperature at which boiling is initiated (*B* of Fig. 1) can usually be predicted to within about 50 F if the relation between saturation temperature and pressure is known for the liquid. The amount of superheat for most liquids is from 10 to 100 F, the higher values corresponding to higher liquid velocities, although no general correlation is known. For design purposes, it is sufficiently accurate to assume the wall

[2] Numbers in parentheses indicate References at end of paper.

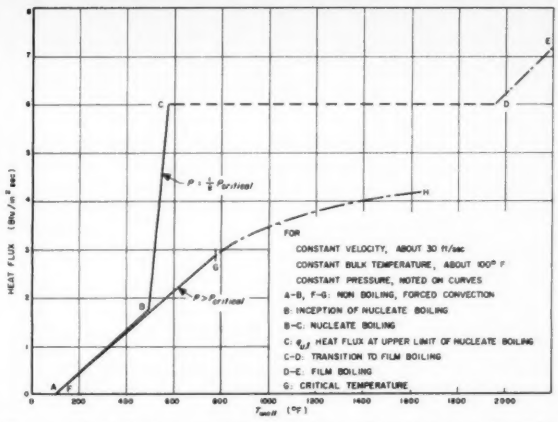
HEAT FLUX (Btu/hr ft² sec)
T_{wall} (°F)
$P = \frac{1}{6} P_{critical}$
$P > P_{critical}$
FOR
CONSTANT VELOCITY, ABOUT 30 ft/sec
CONSTANT BULK TEMPERATURE, ABOUT 100° F
CONSTANT PRESSURE, NOTED ON CURVES
A-B, F-G: NON BOILING, FORCED CONVECTION
B: INCEPTION OF NUCLEATE BOILING
B-C: NUCLEATE BOILING
C: q_{ul} HEAT FLUX AT UPPER LIMIT OF NUCLEATE BOILING
C-D: TRANSITION TO FILM BOILING
D-E: FILM BOILING
G: CRITICAL TEMPERATURE

Fig. 1 Heat flux vs. wall temperature of typical propellant in various heat transfer regimes

temperature at the inception of nucleate boiling is 50 F above saturation temperature. It should be noted that bulk temperature has only a second-order effect on superheat. Saturation temperature curves for most pure liquids are given in the literature. Low-pressure data are best extrapolated by plotting log p vs. reciprocal of absolute temperature. For many multicomponent liquid mixtures, especially those which decompose at elevated temperatures, the saturation temperatures (or more properly the bubble-point temperatures) are not known and, hence, must be measured.

The slope of the heat flux vs. wall-temperature curve in nucleate boiling (*B-C* of Fig. 1) is not correlated for various liquids except that it is generally steeper than the third power of the difference between wall temperature and saturation temperature. Fortunately, this defines the wall temperatures within about 100 F over the range of heat fluxes covered by nucleate boiling of most liquids. It should be noted that the position of the boiling line is independent of either velocity or bulk temperature except through second-order effects on superheat which are probably less than 20 or 30 F in most instances.

The determination of the characteristic curve up into nucleate boiling is thus possible from the considerations mentioned, but this is not of much utility in predicting the limitations of the liquid as a regenerative coolant. This is because the resulting wall temperatures in nucleate boiling are, for most liquids, well below limiting temperatures for successful cooling. The real limitation from a practical viewpoint is the heat flux at the upper limit of nucleate boiling q_{ul} since at heat fluxes above this level, the wall temperatures are generally beyond the limit for successful cooling. Unfortunately, this limiting heat flux cannot be predicted as yet from knowledge of a liquid's physical or transport properties. This is still the unfulfilled goal of a great deal of boiling-heat-transfer research throughout the world. Definite progress has been made toward this goal in recent years through considerations of the dynamics of bubble growth and collapse (1, 3, 4).

The shift in wall temperature (*C-D* of Fig. 1), the heat-transfer coefficients in film boiling (*D-E* of Fig. 1), and the heat-transfer coefficients in the region near the critical temperature (*G* of Fig. 1) are also unpredictable from fluid properties with reasonable accuracy. Prediction of the first two characteristics is not particularly essential if q_{ul} is considered to be the limitation. However, predictions of the supercritical heat-transfer coefficients are essential since they determine the design limitation directly for some coolants. Such predictions are particularly difficult near the critical temperature because of unusual variations of fluid properties with temperature.

Experimental Methods

In order to determine the heat-transfer characteristics of propellants that cannot be predicted by analytical means, a number of experimental programs have been conducted by various organizations on a variety of liquid propellants. An index of references to these data, including ranges of variables investigated and types of data reported, is given in Table 1.

Most of these data were obtained by flowing the propellant through electrically heated tubes or annuli at velocities, pressures, and bulk temperatures common to rocket-motor cooling passages. Generation of heat by use of the tube wall as a resistance element was found to be the most practical means of achieving and controlling the level of heat fluxes required. Measurements required for determination of the desired heat-transfer characteristics are power consumption for computa-

Table 1 Index to measurements of heat transfer to propellants with and without boiling under forced velocity, subcooled conditions

Propellant					Pressure range, psi	Bulk temperature range, °F	Velocity range, ft/sec	
Designation	Nominal composition	Authors	Organization	Reference				Data*
Oxidizers:								
Type III-A RFNA	83% HNO_3, 14% NO_2, 2.5% H_2O, 0.6% HF	Dean	Bell Aircraft	5	100–950	−45–170	5–100	FC, NB, q_{ul}, Dep.
RFNA	92½% HNO_3, 6½% NO_2, 1% H_2O	Bartz, Noel	JPL	6–10	50–500	90–304	15–43	FC, NB, q_{ul}, ΔP, Dep.
SFNA	83% HNO_3, 14% NO_2, 2.5% H_2O, 0.6% HF			11–14	60–500	80–235	30	FC, NB, q_{ul}, Dep.
WFNA	97% HNO_3, 1% NO_2, 2% H_2O				300–900	96–247	30–90	FC, NB, q_{ul}
Type III RFNA	82% HNO_3, 15% NO_2, 3% H_2O, 0.5% HF	Wolfe, Gray, Reese, Graham	Purdue	15–17	90–615	25–95	5–35	FC, NB, Dep., ΔP
WFNA	98% HNO_3, 0.5% NO_2, 1.5% H_2O				65–710	47–160	10–130	FC, NB, Dep., ΔP
WFNA	97.5% HNO_3, 0.5% NO_2, 2.0% H_2O	Ashley	Bell Aircraft	18	65–400	60–90	5–60	FC, NB, q_{ul}
RFNA	92½% HNO_3, 6½% NO_2, 1% H_2O	Hatcher, Bartz	JPL	19	50–500	70–90	10–50	FC, NB, q_{ul}
ClF_3	Commercial grade	Noel	JPL	20	150–860	0–200	15–60	FC, NB, q_{ul}
Liquid Oxygen	.....	Powell	JPL	21	500–1100	−280–340	(3–40)*	FC, subcritical, supercritical
Liquid Oxygen	.....	Banchero, Baner, Ball	Univ. of Michigan	22	....	....	....	....
Liquid Fluorine	.....	....	....	..	....	....	....	....
Fuels:								
Liquid Ammonia	99% NH_3, 1% H_2O	Noel	JPL	23–28	100–1600	50–150	0–137	FC, NB, q_{ul}
Corporal fuel	46% An, 46% FA, 7% N_2H_4, 1% H_2O	Noel	JPL	29	200–400	−10–460	15–45	FC, NB, q_{ul}, ΔP
	80% An, 20% FA	Noel	JPL	6	400	125	30	FC, NB, q_{ul}
	50% An, 50% FA							
	33% An, 67% FA							
	47.5% An, 47.5% FA, 5% N_2H_4							
	45% An, 45% FA, 10% N_2H_4							
	40% An, 40% FA, 20% H_2N_4							
Diacetone Alcohol	Commercial grade	Noel	JPL	6	400	125	30	FC, NB, q_{ul}
Isopropyl Alcohol	Commercial grade	Noel	JPL	6	400	125	30	FC, NB, q_{ul}
DETA (Diethylenetriamine)	90.4% diethylenetriamine 9.6% amino-ethyl-piperazine	Noel	JPL	11, 30	400	10–350	30–40	FC, NB, q_{ul}
Aniline	96% aniline, 4% H_2O	Kreith, Summerfield	JPL	31	35–365	90–135	21–37	FC, NB, Dep.
n-Butyl Alcohol	99.5% *n*-butyl alcohol, 0.5% H_2O	Kreith, Summerfield	JPL	32	50–200	85–100	24–41	FC, NB, ΔP
JP3	Mil-F-5627	Hatcher	JPL	19, 33	50–500	80–150	8–80	FC, NB, q_{ul}, Dep., ΔP
JP4	Mil-F-5624A	Beighley, Dean	Bell Aircraft	34	30–500	75	3–40	FC, NB, q_{ul}
Liquid Hydrogen	.....	Powell	JPL	21	750	−390–700	(0.6–1.9)*	FC, supercritical
Hydrazine	.....	Banchero, Baner, Ball	Univ. of Michigan	22	....	....	....	....
Hydrazine	97% N_2H_4, 3% H_2O	Noel	JPL	35	300–1200	70–320	6–90	FC, NB, q_{ul}

* Units: lb/in.² sec; FC—nonboiling forced convection, NB—forced velocity nucleate boiling; q_{ul}—upper limit of nucleate boiling; ΔP = pressure drop; Dep. = deposition or coking; An = aniline; FA = furfuryl alcohol.

tion of heat flux, flow rate, inlet and outlet pressures and temperatures, and tube-wall temperatures. Because the hydraulic diameters of most rocket motor coolant passages, even up to very large scale, are between $\frac{1}{8}$ and $\frac{1}{2}$ in., tests made with tubes and annuli in this range of sizes suffer little in scaling. Fortunately, from an experimental standpoint, it is not necessary to scale channel length for boiling heat-transfer measurements since uniform heat-transfer conditions are established very close to the entrance of a forced-velocity boiling system. Tubes and annuli of 10 to 20 diam in length are commonly used for such measurements. A necessary but complicating part of some of these experimental investigations has been measurements of such adverse effects as deposition of solids on the heated wall, decomposition of the liquid, and corrosion.

Typical Results of Experimental Investigations

Since there is rather complete experimental confirmation of the methods described for predicting the nonboiling curve, the inception of nucleate boiling, and the wall temperatures in nucleate boiling, the most significant results of experimental investigations are values of q_{ul}, as a function of the three system variables: Pressure, bulk temperature and velocity. Although, as mentioned, no general correlation of this quantity has been achieved, certain trends have been fairly well established. These trends are well represented by data recently obtained by Noel for anhydrous liquid ammonia (23–25).

1. *Effect of pressure on* q_{ul}: It has been found that maximum values of q_{ul} are obtained at pressures which are about 0.4 to 0.6 of the liquid critical pressure for given constant bulk temperatures and velocities. The curve usually slopes quite gently on both sides of the peak. The maximum value for q_{ul} for ammonia at 60 F was obtained at a pressure of about 850 psi or about 52 per cent of critical pressure (Fig. 2).

2. *Effect of bulk temperature on* q_{ul}: It has been found that values of q_{ul} decrease with increasing bulk temperature, reaching a near-zero value at saturation temperature. (The only exceptions to this trend have been observed at bulk temperatures less than about 40 F, where it is believed that viscous effects begin to control the boiling mechanism; (5, 26–29). For some liquids, the decrease is nearly linear with bulk temperature; for others, the values of q_{ul} are greater than for a linear decrease. The data for ammonia (Fig. 3) exhibit this latter trend. Several correlations, notably for water (36, 37) have successfully made use of a correlation variable called subcooling, which is the difference between saturation temperature and bulk temperature. For such correlations, q_{ul} decreases linearly or less than linearly with decreasing subcooling.

3. *Effect of velocity on* q_{ul}: The q_{ul} data for ammonia plotted for constant pressure and various bulk temperatures in Fig. 4 show trends with increasing velocity, which are typical of several propellants investigated. The values of q_{ul} increase linearly with velocity from zero-velocity values which are dependent on pressure and bulk temperature. The slope of the curve is found to be dependent on subcooling with lower slopes at lower subcooling.

4. *Effect of deposition on* q_{ul}: Deposition of carbon by JP3 (33) and deposition of metallic salts by fuming nitric acids (5–14) have been observed to cause rather rapid increases in wall temperatures both with and without nucleate boiling. The effect of such deposition on q_{ul} from these tests is not clear, but the general conclusion drawn from the data of (6–14) is that it did not particularly affect the values of q_{ul} except in the case of SFNA.

Dependence of q_{ul} on System Operating Conditions

Having previously discussed the reasons for considering q_{ul}

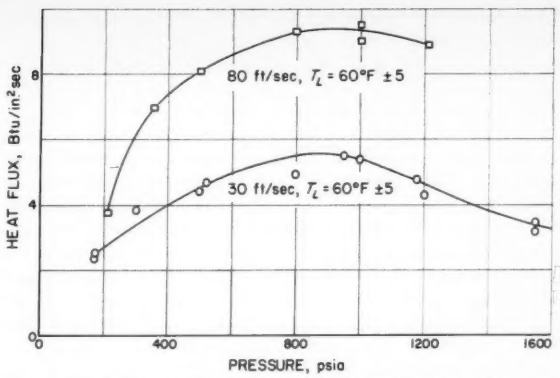

Fig. 2 Heat flux at upper limit of nucleate boiling as a function of pressure for ammonia at bulk temperature 60 F ±5

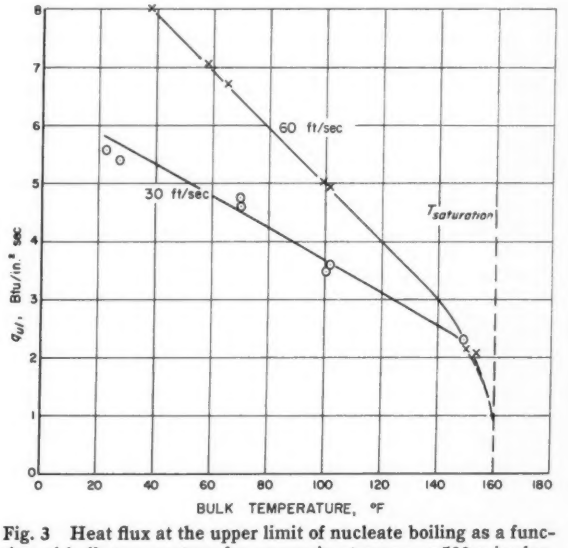

Fig. 3 Heat flux at the upper limit of nucleate boiling as a function of bulk temperature for ammonia at pressure 500 psi velocities of 30 and 60 ft/sec

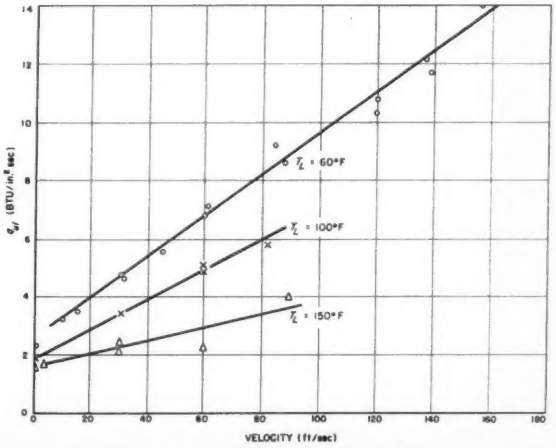

Fig. 4 Heat flux at upper limit of nucleate boiling as a function of velocity for ammonia at pressure 500 psi

as the practical limiting heat flux and having shown the manner in which q_{ul} depends on pressure, bulk temperature, and velocity, it is now of interest to show the effect of the rocket-motor operating conditions on the regenerative cooling problem.

The pressure at the outlet of the coolant system is established by the combustion pressure and the injector pressure drop. It is not generally economical to operate the coolant passage at any higher pressure than necessary. It was noted that pressure affected the value of q_{ul} only slightly over the pressure range from about 0.3 to 0.7 of critical pressure. On the other hand, the net heat flux from the combustion gas to the motor wall is expected to increase with pressure to about the 0.8 power (38) the effect of pressure on nucleate boiling wall temperatures being of second order in determining the heat-transfer driving potential, $(T_c - T_w)$.

The coolant bulk temperature at any point in the coolant passage is simply the sum of the inlet bulk temperature and the temperature rise to that point. The temperature rise is determined by the heat transfer to the wall, the coolant flow rate, and coolant specific heat. Since the higher values of q_{ul} are associated with the lower values of bulk temperature, it is desirable to utilize the largest coolant flow rate possible. For a fixed total propellant consumption, operation at high mixture ratios (O/F) favors cooling with the oxidizer, and operation at low mixture ratios favors cooling with the fuel. Since both propellant consumption and heat flux increases nearly linearly with chamber pressure, bulk temperature rise is not particularly influenced by changes in chamber pressure. Hence, the bulk temperature rise is principally dependent on selection of motor configuration and propellant combination.

With pressure and bulk temperature rise essentially determined by the selection of motor configuration, propellant combination, and combustion pressure, only velocity, of the three parameters affecting q_{ul}, is left for manipulation to gain cooling advantage. Fortunately, q_{ul} can be readily increased by increasing velocity. However, since total coolant flow rate is fixed, velocity can only be increased by decreasing the net flow area of the cooling passage. With axial flow cooling in thin annular passages, it is found that velocity is inversely proportional to the coolant passage height t and that the coolant-passage pressure drop increases with the third power

Table 2 Effect of coolant velocity on value of q_{ul} and on turbopump power requirements

Item	First design	Second design
Coolant velocity at throat (ft/sec)	50	100
Coolant bulk temperature at throat (°F)[a]	100	100
Chamber pressure (psia)	300	300
Injector pressure drop (psia)	75	75
Coolant passage pressure drop (psi)[b]	75	600
Turbopump outlet pressure (psi)	450	975
Pressure at throat in coolant passage (psia)	423	675
Value of q_{ul} at throat (Btu/in² sec)[c]	4.2	7.7
Total propellant consumption required for fuel turbopump (%)[d]	2.0	4.25
Increase in value of q_{ul} (%)	...	83
Increase in total propellant consumption required for fuel turbopump (%)	...	2.25

[a] Calculation for NH_3 cooled motor.
[b] Coolant passage pressure drop proportional to V^3.
[c] Interpolated from Figures 2 and 4.
[d] For constant mass flow rate turbopump power requirement assumed proportional to head; assuming constant efficiency, propellant consumption is proportional to power.

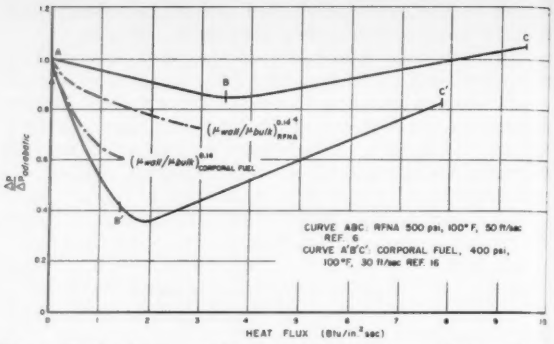

Fig. 5 Ratio of pressure drop to adiabatic pressure drop vs. heat flux for RFNA and for *Corporal* fuel

of velocity for turbulent flow. A sample calculation for a 300-psi chamber pressure, turbo-pump-fed, ammonia-cooled rocket motor (summarized in Table 2) shows the cooling advantage and performance penalty resulting from doubling the coolant velocities. While the calculation is, of necessity, not general, the results are considered to be typical. They show that the value of q_{ul} can nearly be doubled for as little as about 2 per cent increase in propellant consumption (for turbopump) and perhaps a moderate increase in system dead weight. Hence, such changes should receive full consideration during preliminary design of a regeneratively cooled rocket propulsion system.

Dependence of Pressure Drop on Heat Transfer

Considerations of coolant-passage pressure drop such as discussed in the section on Dependence of q_{ul} on System Operating Conditions require knowledge of the manner in which the pressure drop varies with type and magnitude of heat transfer. A convenient method of showing this variation is through the use of the ratio of pressure drop per unit length with heat transfer to that without heat transfer for equal bulk temperature, and mass flow rate. This ratio is plotted vs. heat flux in Fig. 5 from experimental data for two propellants, RFNA and *Corporal* fuel (a mixture of aniline, furfuryl alcohol, and hydrazine). The results for RFNA from (5) showed that $\Delta p/\Delta p_{q=0}$ decreased from 15 per cent over the heat-flux range from zero to the inception of nucleate boiling (point B of Fig. 5). This decrease is somewhat less than would be predicted by the Sieder-Tate friction factor correction $(\mu_w/\mu_b)^{0.14}$ which is usually recommended. Data presented in (16) for WFNA were correlated with this viscosity ratio to the 0.12 power.

Pressure-drop data measured in the nonboiling region for *n*-butyl alcohol (32) and the *Corporal* fuel (26–29) decreased with increasing heat flux to a much greater extent than would be predicted by the factor $(\mu_w/\mu_b)^{0.14}$, the resultant exponents being 0.3 and 0.2, respectively. Curve $A'B'C'$ (Fig. 5) drawn from data for the latter fuel at 100 F bulk temperature shows experimental values of the pressure-drop ratio as low as about 0.4 at the inception of nucleate boiling.

With heat fluxes increasing into the nucleate boiling range, the values of the ratio level off, then increase. Maximum values of the pressure-drop ratio at the upper limit of nucleate boiling both above and below unity have been observed, depending upon particular conditions of bulk temperature and pressure. The amount of pressure-drop data measured during the programs referenced was insufficient to achieve a correlation. Since the total pressure drop is an integration of friction on the cool wall under adiabatic conditions and on the hot wall both with and without boiling the general conclusion drawn from the data was that a calculation based on the adiabatic

conditions would be high by less than about 10 per cent for the acid cooling and 25 per cent for the *Corporal* fuel cooling.

Unfortunately, very little data on pressure drop have been reported from which to establish correlations or draw general conclusions. This is partially due to the fact that pressure-drop measurements must be made over short sections since at nucleate boiling heat fluxes the bulk temperature rise per unit length is quite large. Such pressure-drop measurements are difficult to make with acceptable accuracy. Additional measurements are definitely needed to settle the questions concerning coolant-passage pressure drops.

Operational Comparison of Cooling Capabilities of Several Propellants

Having discussed various aspects of the utilization of propellants as regenerative coolants, it is still not possible to calculate a parameter which will characterize the potentialities of a particular propellant as a coolant relative to other propellants. This situation is a result of (1) the apparently complex relation between q_{ul} and liquid properties and (2) the variables which are closely related to the selection of the combustion system, motor configuration, and combustion pressure. Although the final evaluation of the merits of a particular coolant must await a detailed design analysis, some measure of comparison between propellants can be achieved by considering several propellants as potential coolants for a hypothetical motor of given configuration and computing the margin between the local values of q_{ul} of the coolant and the heat flux to the wall in a critical region such as the throat.

Such a comparison was made using the propellants listed in the first column of Table 3 as the coolants. The propellants listed in the second column were considered to react with the coolant-propellant at peak-performance mixture ratios with resulting values of c^* which were 95 per cent of theoretical values, based on equilibrium composition expansion. The propellant consumption was such as to produce 50,000 lb of thrust at chamber pressure near 300 psia with each combination burning in the same motor.

The pertinent configurational parameters of the motor selected were L^* 40 in., throat area 117 in.^{2}, 2:1 contraction area ratio, 7:1 expansion area ratio, 30-deg contraction half angle, 15-deg expansion half angle, and throat radius of curvature equal to throat diameter. The motor was assumed to have an annular coolant passage of height t which was constant along the whole length of the motor. The value of t was allowed to vary from coolant to coolant so as to result in a 75-psi coolant-passage pressure drop for the appropriate flow rate of each particular coolant. Since the manner in which the friction factor for each coolant varies with heat flux is unknown, the adiabatic value was used for this comparison, using values of viscosity and density which were the average between inlet and outlet bulk temperatures.

An inlet bulk temperature of 100 F was assumed for each of the coolants except liquid ammonia, which it was assumed could be reduced to 32 F by venting the tank prior to flight. The bulk-temperature rise of the coolant from the nozzle exit end to the throat and over-all bulk temperature rise were calculated from the coolant flow rate, specific heat and heat flux to the wall, computed with the following assumptions. Chamber gas temperatures 90 per cent of theoretical equilibrium combustion chamber temperature were assumed, the fraction being the result of assuming c^* to be 95 per cent of its theoretical value. Wall temperature was 50 F (superheat) above coolant saturation temperature at 410 psi, the average coolant-passage pressure. This wall temperature results from assuming the combustion side wall to have negligible thermal resistance, and assuming the mechanism of heat transfer along the whole passage to be nucleate boiling. The local heat flux was computed by multiplying the difference between chamber gas temperature and wall temperature by heat-transfer coefficients computed by the methods of (38). For reasons discussed in (38, 39), the values of the computed heat flux are expected to be generally too high in the chamber, and throughout the nozzle as well, for carbonaceous systems which deposit carbon on the gas side walls during combustion. On the other hand, computed heat flux values are expected to be too low for systems burning either with appreciable dissociation or with unstable combustion or both. These complicating factors cannot be accounted for analytically at present, but it is believed that values predicted on the basis of pure convection are still useful for the comparison of this report; however, in drawing specific comparative conclusions between systems calculated, qualitative allowances should be made for these uncertainties.

With these assumptions, it was possible to compute the

Table 3 Comparison between calculated convective throat heat flux and throat values of q_{ul} for ten propellant systems

	Coolant	Reactant	1 r	2 c^*, ft/sec	3 T_c, ° R	4 q^*, Btu/in.^{2} sec	5 $W_{coolant}$, lb/sec	6 t, in.	7 V^*, ft/sec	8 $T_L{}^*$, ° F	$q_{ul}{}^*$ value Btu/in.^{2} sec	Reference	T_{sat}, ° F, at 375 psi	T_{Lout}, ° F
a	RFNA	UDMH	2.5	5083	4796	5.85	158.0	0.109	60.8	179	8.8	6–14	355†	242
b	Corporal fuel	SFNA	3.0	4763	4938	5.07	59.3	0.0716	49.3	243	8.20	26–29	580†	358
c	DETA	SFNA	3.0	4930	4808	5.02	57.3	0.0724	58.6	214	7.20*	26–29	740	306
d	50 An-50 FA	SFNA	3.0	4740	4955	4.90	59.6	0.0719	50.0	236	5.40*	6	680†	346
e	JP-3	N_2O_4	3.0	5069	5206	4.91	55.8	0.0712	63.4	238	5.25*	33	670†	349
f	NH_3	RFNA	2.2	4997	4224	5.58	70.7	0.0614	72.5	92	5.30	23–25	140	140
g	Isopropanol	SFNA	3.3	4757	4744	5.24	55.3	0.0744	63 0	207	4.50*	6	550	293
h	NH_3	O_2	1.41	5499	4882	6.52	85.3	0.0688	78.0	92	5.80	23–25	140	135
i	JP-3	O_2	2.25	5593	5577	6.00	62.2	0.0762	67.1	276	5.15*	33	670†	376
j	ClF_3	N_2H_4	2.50	5546	5881	5.83	145.0	0.0912	57.8	213	4.25	20	258	304

* Extrapolated from lower velocity and lower bulk temperature values.

† Estimated from nucleate boiling wall temperature measurements.

COLUMN NOTES: 1. Approximately peak performance (I_{sp} @ 300 psi) mixture ratio, oxidizer/fuel. 2. 95 per cent of theoretical value based on equilibrium expansion. 3. 90 per cent theoretical value. 4. Computed from $q^* = h_g{}^*(T_c - T_w)$: $h_g{}^*$ computed from Ref. 25 C_p based on constant composition value from thermochemical performance calculation, T_w taken to be 50 F higher than saturation temperature of the coolant at throat pressure, 410 psia. 5. Value based on total utilization of propellant for regenerative cooling. 6. Computed coolant passage height for 75 psi coolant passage pressure drop, using isothermal friction factor values, and average values of density and viscosity between inlet and outlet temperatures. 7. Coolant velocity of throat. 8. Coolant bulk temperature at throat, based on 100 F inlet bulk temperature for all coolants except NH_3 where 32 F was used.

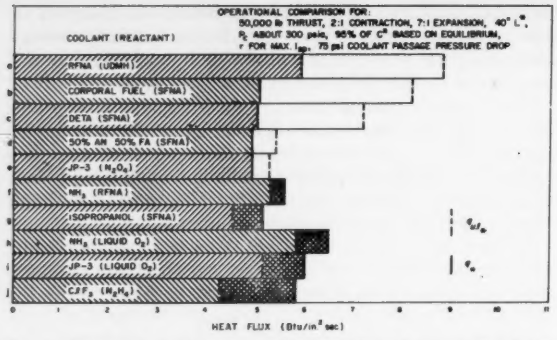

Fig. 6 Comparison between calculated throat convective heat flux and throat values of q_{ul} of ten propellant systems (see Table III for performance and mixture ratio)

values of pressure, velocity and bulk temperature of each coolant at the throat. Values of q_{ul} at these conditions, (q_{ul}*), were determined from experimental data and compared with computed values of throat heat flux, q*. These results are presented in Table 3 and Fig. 6.

It is most significant to note that the computed bulk temperature rise with the ClF_3 system, is such that the saturation temperature is exceeded by the bulk temperature within the coolant passage, and saturation temperature is nearly reached with the NH_3 systems. Successful cooling even in the chamber under such conditions is extremely unlikely since values of q_{ul} drop well below 1 Btu/in.² sec when bulk temperature reaches saturation temperature. This is a good point at which to start a proposed regenerative cooling design.

Of the systems calculated, it appears that the RFNA, the *Corporal* fuel and DETA coolants offer the best margins for cooling, the values of q_{ul}* being comfortably above throat heat flux values. It must be remembered that the expected throat heat flux for the JP3-O_2 system would probably be as much as 50 per cent lower than predicted because of expected effects of carbon deposition. Hence, in practice, this system would also have a satisfactory but very unpredictable margin for cooling. Systems *d*, *e*, and *f* were predicted to be marginal within the uncertainties in predictions of heat flux to the wall. For most fuel-cooled systems, shifts toward lower mixture ratios, and for most oxidizer cooled systems, shifts toward higher mixture ratios, could be made to gain cooling advantage with only negligible penalties in performance.

As indicated by the calculation in Table 2, even a coolant with apparently poor cooling capabilities such as isopropanol could be employed successfully if significantly greater coolant passage pressure drop is allowed in order to increase coolant velocity.

Conclusions

From such calculations and comparisons as presented in this report, some general conclusions can be drawn relative to liquid physical and chemical properties and to motor-operating conditions which are favorable for regenerative cooling.

In order to achieve successful regenerative cooling in a rocket motor with propellants below their critical temperature and pressure, sufficient coolant flow must be provided to achieve local values of the heat flux at the upper limit of nucleate boiling q_{ul} which, everywhere throughout the motor, exceed corresponding local heat fluxes from the combustion gases to the wall.

The total heat rate that can be absorbed by a coolant at bulk temperatures below saturation temperature is equal to the product of flow rate, specific heat and difference between saturation temperature and coolant inlet temperature. This total heat rate must be safely above the total expected heat-rejection rate from the combustion gases to the motor wall since values of q_{ul} decreases sharply as bulk temperatures approach saturation temperature, becoming too low for successful cooling even back near the injector. For this reason a high specific heat, and/or a saturation temperature at least about 300 F is desirable. However, higher saturation temperatures than about 700 F allow wall temperatures to climb too high before being limited by nucleate boiling. Even this temperature would prohibit the use of aluminum as a wall material and would significantly reduce the allowable stresses of steel materials.

A liquid critical pressure such that coolant passage pressures are from about 0.3 to 0.7 of critical pressure is desirable. Liquids operating in this pressure range usually exhibit a maxima in values of q_{ul} for given velocity and bulk temperature. Fluids which must be used at pressures above their critical pressure are usually poorer coolants than those operated below critical pressure, especially if the bulk temperature goes from subcritical to supercritical somewhere in the coolant passage.

A low viscosity is a favorable liquid physical property, since it permits higher coolant velocities for a given pressure drop at a given mass flow rate. Furthermore, increasing viscosity is believed to be the explanation for the two cases mentioned where q_{ul} was observed to decrease with decreasing bulk temperature, contrary to the normal trend.

Liquids which decompose either at limited rates, or explosively, which deposit salts or carbon on the hot wall, or which corrode the wall are generally inferior to liquids which are essentially chemically inert under coolant-passage conditions.

The cooling of a motor with the oxidizer is best accomplished by operating the motor at high-oxidizer-to-fuel mixture ratios. Conversely, cooling with the fuel is best accomplished at low mixture ratios. For many systems, significant changes in mixture ratio from the peak performance value can be made to gain cooling advantage with but little sacrifice in performance.

The only design parameter that is available to the designer to improve cooling conditions once the propellants, mixture ratio, combustion pressure, and motor configuration are selected is the coolant velocity which may be advantageously increased by decreasing coolant passage flow area with an attendant increase in coolant passage pressure drop. For some systems cooling with both propellants may be required.

References

1 Bankoff, S. G., Colahan, W. J. and Bartz, D. R., Summary of Conference on Bubble Dynamics and Boiling Heat Transfer Held at the Jet Propulsion Laboratory, June 14–15, 1956, Memorandum 20-137. Pasadena: Jet Propulsion Laboratory, Dec. 10, 1956.

2 Sieder, E. N. and Tate, G. E., "Heat Transfer and Pressure Drop of Liquid in Tubes," *Industrial and Engineering Chemistry*, vol. 28: 1936, pp. 1429–1436.

3 Ellion, M. E., "A Study of the Mechanism of Boiling Heat Transfer," Memorandum 20-88. Pasadena: Jet Propulsion Laboratory, March 1, 1954.

4 Forster, H. K. and Zuber, N., "Dynamics of Vapor Bubbles and Boiling Heat Transfer," *Journal American Institute of Chemical Engineers*, vol. 1, 1954, p. 531.

5 Dean, L. E., "Heat Transfer Characteristics of RFNA," Report 117-982-004. Buffalo: Bell Aircraft Corporation, July 1956.

6 Combined Bimonthly Summary No. 36 (April 20 to June 20, 1953). Pasadena: Jet Propulsion Laboratory, July 20, 1953 (Confidential).

7 Combined Bimonthly Summary No. 37 (June 20 to Aug. 20, 1953). Pasadena: Jet Propulsion Laboratory, Sept. 20, 1953 (Confidential).

8 Combined Bimonthly Summary No. 38 (Aug. 20 to Oct. 20, 1953). Pasadena: Jet Propulsion Laboratory, Nov. 20, 1953 (Confidential).

9 Combined Bimonthly Summary No. 39 (Oct. 20 to Dec. 20, 1953). Pasadena: Jet Propulsion Laboratory, Jan. 20, 1954 (Confidential).

10 Combined Bimonthly Summary No. 40 (Dec. 20, 1953 to Feb. 20, 1954). Pasadena: Jet Propulsion Laboratory, March 20, 1954 (Confidential).

11 Combined Bimonthly Summary No. 41 (Feb. 20 to April 20, 1954). Pasadena: Jet Propulsion Laboratory, May 20, 1954 (Confidential).

12 Combined Bimonthly Summary No. 42 (April 20 to June 20, 1954). Pasadena: Jet Propulsion Laboratory, July 20, 1954 (Confidential).

13 Combined Bimonthly Summary No. 43 (June 20 to Aug. 20, 1954). Pasadena: Jet Propulsion Laboratory, September 20, 1954 (Confidential).

14 Combined Bimonthly Summary No. 50 (Oct. 1 to Dec. 1, 1955). Pasadena: Jet Propulsion Laboratory, December 15, 1955 (Confidential).

15 Wolf, H., Gray, F. L. and Reese, B. A., "Heat Transfer and Friction Characteristics of Red and White Fuming Nitric Acid," JET PROPULSION, vol. 26, Nov. 1956, p. 979.

16 Reese, B. A. and Graham, R. W., "Experimental Investigation of Heat Transfer and Fluid Friction Characteristics of White Fuming Nitric Acid," Technical Note 3181. Washington: NACA, May 1954.

17 Reese, B. A., and Graham, R. W., "Heat Transfer and Friction Pressure Drop Characteristics of White Fuming Nitric Acid," JET PROPULSION, vol. 24, no. 4, July-Aug., 1954, p. 228.

18 Ashley, E., "Heat Transfer Measurements for White Fuming Nitric Acid, Report No. 56-982-016. Buffalo: Bell Aircraft Corporation, Feb. 1953.

19 Hatcher, J. B. and Bartz, D. R., "High Flux Heat Transfer to JP-3 and RFNA," External Publication No. 119. Pasadena: Jet Propulsion Laboratory, November 1951.

20 Combined Bimonthly Summary No. 56 (Oct. 7 to Dec. 1, 1956). Pasadena: Jet Propulsion Laboratory, Dec. 15, 1956 (Confidential).

21 Powell, W. B., "Heat Transfer to Fluids in the Region of the Critical Temperature," Progress Report No. 20-285. Pasadena: Jet Propulsion Laboratory, April 1956.

22 Banchero, Baner and Ball, "Heat Transfer Characteristics of Boiling Oxygen, Fluorine, and Hydrazine," Report 51-11. Ann Arbor: University of Michigan Engineering Research Institute.

23 Combined Bimonthly Summary No. 52 (Feb. 1 to April 1, 1956). Pasadena: Jet Propulsion Laboratory, April 15, 1956 (Confidential).

24 Combined Bimonthly Summary No. 53 (April 1 to June 1, 1956). Pasadena: Jet Propulsion Laboratory, June 15, 1956 (Confidential).

25 Combined Bimonthly Summary No. 54 (June to Aug. 1, 1956). Pasadena: Jet Propulsion Laboratory, Aug. 15, 1956 (Confidential).

26 Combined Bimonthly Summary No. 44 (Aug. 20 to Oct. 20, 1954). Pasadena: Jet Propulsion Laboratory, Nov. 20, 1954 (Confidential).

27 Combined Bimonthly Summary No. 45 (Oct. 20 to Dec. 20, 1954). Pasadena: Jet Propulsion Laboratory, Jan. 20, 1955 (Confidential).

28 Combined Bimonthly Summary No. 46 (Dec. 20, 1954 to March 31, 1955). Pasadena: Jet Propulsion Laboratory, April 1, 1955 (Confidential).

29 Combined Bimonthly Summary No. 47 (April 1 to June 1, 1955). Pasadena: Jet Propulsion Laboratory, June 15, 1955 (Confidential).

30 Combined Bimonthly Summary No. 51 (Dec. 1, 1955 to Feb. 1, 1956). Pasadena: Jet Propulsion Laboratory, Feb. 15, 1956 (Confidential).

31 Kreith, F. and Summerfield, M., "Heat Transfer From an Electrically Heated Tube to Aniline at High Heat Flux," Progress Report No. 4-88. Pasadena: Jet Propulsion Laboratory, Feb. 1949.

32 Kreith, F. and Summerfield, M., "Investigation of Heat Transfer at High Heat Flux: Experimental Study of Heat Transfer and Friction Drop with *n*-Butyl Alcohol in an Electrically Heated Tube." Progress Report No. 4-95. Pasadena: Jet Propulsion Laboratory, May 1949.

33 Hatcher, J. B., "High Flux Heat Transfer and Coke Deposition of JP-3 Fuel Mixture," Progress Report No. 20-157. Pasadena: Jet Propulsion Laboratory.

34 Beighley, C. M. and Dean, L. E. "Study of Heat Transfer to JP-4 Jet Fuel," JET PROPULSION, vol. 24, No. 3, May-June 1954, p. 180.

35 Combined Bimonthly Summary No. 57 (Dec. 1, 1956 to Feb. 1, 1957). Pasadena: Jet Propulsion Laboratory, Feb. 15, 1957 (Confidential).

36 Gunther, F. C., "Photographic Study of Surface-Boiling Heat Transfer to Water with Forced Convection," Transactions of the American Society of Mechanical Engineers, vol. 73, 1951, pp. 115–123.

37 Rohsenow, W. M. and Clark, J. A., Technical Report No. 4, DIC Project No. 6627. Cambridge: Massachusetts Institute of Technology, 1952.

38 Bartz, D. R., "A Simple Equation for Rapid Estimation of Rocket Nozzle Convective Heat Transfer Coefficients," JET PROPULSION, vol. 27, Jan. 1957.

39 Bartz, D. R., "An Approximate Solution of Compressible Turbulent Boundary Layer Development and Convective Heat Transfer in Convergent-Divergent Nozzles," Progress Report No. 20-234. Pasadena: Jet Propulsion Laboratory, July 1954 (also *Transactions of the American Society of Mechanical Engineers*, vol. 77, no. 8, Nov. 1955, p. 1235).

Technical Notes

Criteria for Orbital Entry

LOUIS G. VARGO[1]

The Ramo-Wooldridge Corporation

THE PROBLEM of entry into a circular orbit has been investigated using the concept of characteristic velocity (1).[2] We may regard use of the characteristic velocity as a definition of an optimization criterion. With this criterion, an important result shown in Fig. 3 of (1) is that the characteristic velocity reaches a maximum value at a finite distance from the departure point when the Hohmann ascent method (2) is employed. This note gives a corresponding result for a different criterion, viz., the radial distance at which the payload reaches a minimum for a fixed initial weight.

Consider the final stage(s) of total initial weight w_0 boosted to an initial tangential velocity v_0 at a radial distance r_0. Equations [1 and 2] give the initial and final velocity increments required to achieve circular velocity at a radial distance r_s.

$$\Delta v_0 = \sqrt{\frac{\gamma}{r_0}}\sqrt{\frac{2\sigma}{1+\sigma}} - v_0 \quad \ldots\ldots [1]$$

$$\Delta v_s = \sqrt{\frac{\gamma}{r_0}}\left[\frac{1}{\sqrt{\sigma}} - \frac{1}{\sigma}\sqrt{\frac{2\sigma}{1+\sigma}}\right] \quad \ldots\ldots [2]$$

Here $\sigma = r_s/r_0$ and γ is the constant of the gravitational field under consideration. The characteristic velocity, $\Delta v_0 + \Delta v_s$, may be differentiated to obtain the cubic equation

$$\sigma^3 - 15\sigma^2 - 9\sigma - 1 = 0 \quad \ldots\ldots [3]$$

which has the positive root $\sigma \approx 15.6$. This is the aforementioned result of (1). Let $\bar{w}$ denote the payload weight. The relationship between the over-all payload ratio $\bar{w}/w_0$ and σ takes two forms depending on whether or not weight is jettisoned after Δv_0 is added. Equations [4 and 5] give this relationship for the two cases.

$$\text{no jettisoning} \qquad \frac{\bar{w}}{w_0} = \frac{\exp\left(-\frac{\Delta v_0}{c_0} - \frac{\Delta v_s}{c_s}\right) - k}{1-k} \quad \ldots [4]$$

$$\text{jettisoning} \qquad \frac{\bar{w}}{w_0} = \frac{\left[\exp\left(-\frac{\Delta v_0}{c_0}\right) - k_0\right]\left[\exp\left(-\frac{\Delta v_s}{c_s}\right) - k_s\right]}{(1-k_0)(1-k_s)} \quad \ldots [5]$$

In Eq. [4], k is the empty weight factor relative to $w_0 - \bar{w}$; in [5], k_0 and k_s denote the empty weight factors relative to the gross weights of the two steps which total $w_0 - \bar{w}$. c_0 and c_s are the exhaust velocities of the propulsion systems producing the two velocity increments.

Received August 29, 1957.

[1] Member of the Technical Staff, Preliminary Design Group, Space Technology Laboratories. Mem. ARS.

[2] Numbers in parentheses indicate References at end of paper.

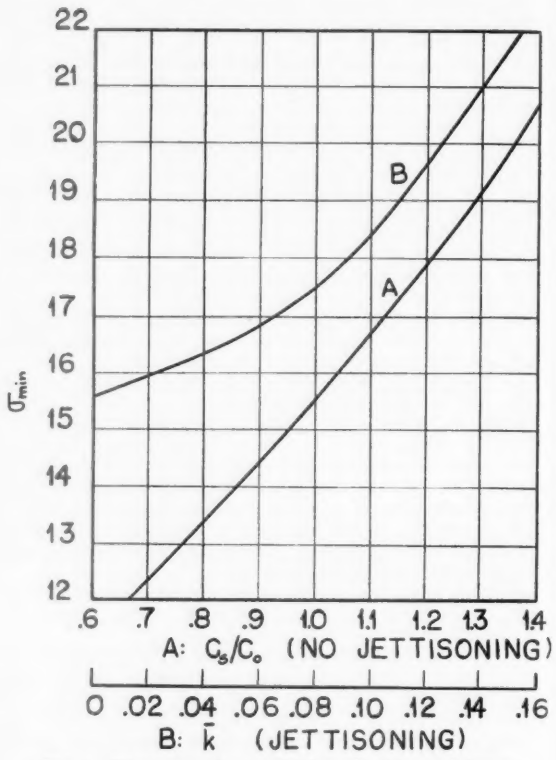

Fig. 1 Distance ratios at which payload is a minimum

From an inspection of [4] we see that the payload ratio is monotonically related to the expression $\Delta v_0/c_0 + \Delta v_s/c_s$. The minima of $\bar{w}/w_0$ occur at points $(\sigma_{min},\ c_s/c_0)$ which satisfy

$$\sigma^2 - \left[2\left(\frac{c_s}{c_0}+2\right)^2 - 3\right]\sigma^2 - \left[4\left(\frac{c_s}{c_0}+2\right) - 3\right]\sigma - 1 = 0 \quad \ldots [6]$$

Fig. 1 shows the essentially linear dependence of σ_{min} on c_s/c_0 for a range of exhaust velocity ratios of interest. Thus, for the case of no jettisoning, the two criteria give identical results only if $c_s = c_0$.

If weight is jettisoned, Eq. [5] can be differentiated to obtain

$$\frac{\exp\left[-af_1(\sigma) - abf_2(\sigma) + d\right] - k_s \exp\left[-af_1(\sigma) + d\right]}{\exp\left[-af_1(\sigma) - abf_2(\sigma) + d\right] - k_0 \exp\left[-abf_2(\sigma)\right]} = bf_3(\sigma) \quad \ldots [7]$$

$$a = \sqrt{\frac{\gamma}{r_0 c_0^2}},\ b = \frac{c_0}{c_s},\ d = \frac{v_0}{c_0}$$

$$f_1(\sigma) = \sqrt{\frac{2\sigma}{1+\sigma}},\ f_2(\sigma) = \frac{1}{\sqrt{\sigma}} - \frac{f_1}{\sigma},\ f_3(\sigma) = \frac{\sqrt{\sigma}+f_2}{f_1} - 2$$

EDITOR'S NOTE: This section of JET PROPULSION is open to short manuscripts describing new developments or offering comments on papers previously published. Such manuscripts are published without editorial review, usually within two months of the date of receipt. Requirements as to style are the same as for regular contributions (see masthead page of this issue).

As an example of the use of Eq. [7] consider the numerical case $a = d = 3$, $b = 1$ and $k_0 = k_s = \bar{k}$. Fig. 1 shows a plot of σ_{min} as a function of $\bar{k}$.

The above results point out the necessity for separate analyses of orbital entry problems when both vehicle and trajectory criteria are considered.

References

1 Lawden, D. F., "Entry into Circular Orbits—I," *Journal of the British Interplanetary Society*, vol. 10, January 1951, pp. 5–17.

2 Hohmann, W., "Die Erreichbarkeit der Himmelskörper," R. Oldenbourg, Munich, 1925.

Minimality for Problems in Vertical and Horizontal Rocket Flight

STANLEY ROSS[1]

Lockheed Missile Systems Division, Palo Alto, Calif.

Nomenclature

t = time
x = instantaneous range
y = instantaneous height
v = instantaneous velocity
m = instantaneous mass
g = gravitational acceleration, assumed constant
c = relative exhaust velocity, assumed constant
m_1 = payload
ξ = gx/c^2 nondimensional range
η = gy/c^2 nondimensional height
ν = v/c nondimensional velocity
μ = m/m_1 nondimensional mass
φ = μe^{ν}
Ω = $\dfrac{W_0 c^2}{m_1 g}$ where W_0 is proportional to C_D, the drag coefficient
D = modified drag function, assumed dependent on ν and η only
λ = Lagrange multiplier function

Introduction

ROCKET thrust programs for stationary values of fuel consumption have been investigated by several authors. In particular, vertical motion of the sounding rocket has been studied (1–3),[2] as has the case of purely horizontal flight (4). These treatments have employed some combination of maximum-thrust arcs (boosts), varying-thrust arcs (sustain) and zero-thrust arcs (coasting) to establish an over-all optimum. By a simple artifact, a condition may be found for each case by whose satisfaction that entire trajectory furnishes not only a stationary path, but actually a true local minimum.

Case I: The Sounding Rocket

We define a new dependent variable $\varphi = \mu e^{\nu}$, and seek those functions $\varphi(\eta)$ and $\nu(\eta)$ which minimize $\varphi(0) = \varphi_0$, under the constraint[3]

$$\Psi \equiv \varphi' + \frac{\varphi}{\nu} + D(\nu, \eta) = 0 \quad \ldots\ldots\ldots\ldots [1]$$

such that $\nu(0) = 0$, $\nu(\eta_1) = 0$, $\varphi(\eta_1) = 1$. (Differentiation is with respect to η, here the independent variable.) This may be associated with Mayer's problem (5), for which the following extremals arise

$$(F_{\varphi'})' = F_{\varphi} \qquad \lambda' = \frac{\lambda}{\nu} \quad \ldots\ldots\ldots\ldots [2]$$

$$(F_{\nu'})' = F_{\nu} \qquad 0 = \lambda\left[-\frac{\varphi}{\nu^2} + D_{\nu}\right] \quad \ldots\ldots\ldots\ldots [3]$$

($F = \lambda\Psi$). From Equation [2], $\lambda = \lambda_0 \exp(gt/c)$. Since Equations [2 and 3] are homogeneous in λ and λ', the multiplier may be assigned an arbitrary nonzero[4] value at a particular point of the interval $(0, \eta_1)$. We choose $\lambda(0) = \lambda_0 = 1$, from which it follows that $\lambda \neq 0$. Therefore, on the path indicated by [2 and 3]

$$\varphi \equiv \nu^2 D_{\nu} \quad \ldots\ldots\ldots\ldots [4]$$

When $D = \Omega\nu e^{\nu - \beta\eta}$, i.e., quadratic drag law, condition [4] reduces to

$$\mu \equiv \Omega\nu^2(1 + \nu)e^{-\beta\eta} \qquad \text{in } (0, \eta_1) \quad \ldots\ldots\ldots [5]$$

as has been noted previously (3). The second variation of φ_0 can be shown[5] to be of the form

$$\delta^2\varphi_0 = \frac{1}{\lambda_0}\int_0^{\eta_1} [F_{\varphi\varphi}\delta\varphi^2 + 2F_{\varphi\nu}\delta\varphi\delta\nu + F_{\nu\nu}\delta\nu^2]d\eta \quad \ldots [6]$$

Now,

$$\delta F = F_{\varphi'}\delta\varphi' + F_{\varphi}\delta\varphi + F_{\nu'}\delta\nu' + F_{\nu}\delta\nu = 0$$

and by [1, 3, 2] respectively

$$F_{\nu'} \equiv 0; \qquad F_{\nu} \equiv 0; \qquad (F_{\varphi'})' \equiv F_{\varphi}$$

Thus $(F_{\varphi'}\delta\varphi)' = 0$, in $(0, \eta_1)$. At $\eta = 0$, $\delta\varphi = 0$ for a stationary value of φ_0. And since $F_{\varphi'} = \lambda \neq 0$, we conclude that $\delta\varphi = 0$ identically in $(0, \eta_1)$. Equation [6] becomes

$$\delta^2\varphi_0 = \int_0^{\eta_1} F_{\nu\nu}\delta\nu^2 d\eta$$

A necessary and sufficient condition for a true local minimum is then that $F_{\nu\nu} > 0$, along the trajacetory. In particular, whenever D is of the form $\Omega\nu^p e^{\nu - \beta\eta}$ then

$$F_{\nu\nu} = \lambda\left\{\frac{2\varphi}{\nu^3} + \Omega\nu^{p-2}[(\nu + p)^2 - p]e^{\nu - \beta\eta}\right\}$$

which is positive for all values of p, except perhaps for $0 < p < 1$. Specifically, it is positive for both linear and quadratic drag laws.

Equation [4] determines values of the two end-point velocities, which will be different from zero. Terminal boosts of infinite thrust are therefore introduced in order that the required velocity discontinuities may be achieved at these points. And since φ is continuous across such instantaneous boosts, φ_0 is still minimal over the entire path, including these boosts. However, if the thrust is to be bounded by a zero minimum value (i.e., coasting), it may be necessary to join this "boundary-curve" program to the path defined by Eq. [3 and 4] in such a way that the desired end conditions are attained.[6] The over-all trajectory in such cases is then a constrained minimum,[7] subject to the above thrust limitation.

Received October 7, 1957.

[1] Graduate student, Division of Engineering and Applied Physics, Harvard University, Cambridge, Mass. Now with Lockheed Missile Systems Div. Mem. ARS.

[2] Numbers in parentheses indicate References at end of paper.

[3] Cf. reference (3), Eq. [2.1]. After eliminating time as the independent variable in favor of height from this equation of motion, and nondimensionalizing in terms of φ, ν, η, Eq. [1] assumes its present form.

[4] If $\lambda = 0$ at any point where [2 and 3] hold then it must be zero identically. Then it can be shown that $\delta F = 0$, without $\delta\varphi_0$ necessarily being zero, which is not a legitimate solution.

[5] Cf. reference (5), page 23, Eq. 7.

[6] The Weierstrass-Erdmann First Corner Condition must be satisfied at all junctions between two dissimilar extremals. Here the condition is that λ be continuous across each junction.

[7] Cf. reference (6), page 42.

Case II: Hibbs' Problem of Optimum Horizontal Flight[8]

In this case φ_0 is to be minimized subject to

$$\Psi \equiv \varphi' + K_1 \nu e^{\nu} + K_2 \varphi^2 \nu^{-3} e^{-\nu} = 0 \quad \ldots\ldots\ldots [7]$$

where K_1 and K_2 are constants, and the last term on the left represents the effect of lift-induced drag. (Differentiation is with respect to ξ, here the independent variable.) Analysis following that of the previous case shows that

(a) By the Euler-Lagrange equations

$$\mu = K_3 \nu^2 \sqrt{\frac{1+\nu}{3+\nu}}$$

is the burning program to be followed for a stationary φ_0

(b) $\delta\varphi \equiv 0$, in (ξ_0, ξ_1)

(c) The second variation reduces to the form

$$\delta^2\varphi_0 = \int_{\xi_0}^{\xi_1} F_{\nu\nu} \delta\nu^2 d\xi$$

where $F_{\nu\nu} > 0$ is again a necessary and sufficient condition for a true local minimum.

(d) Here $F_{\nu\nu} > 0$ always, and the burning program indicated in (a) is to be employed, unless physical restrictions dictate the insertion of coasting arcs. Insertion of terminal boosts is also indicated, and the solution again provides either a free, or thrust-restricted, local minimum.

[8] Cf. reference (4).

References

1 Hamel, G., "Über eine mit dem Problem der Rakete zusammenhängende Aufgabe der Variationsrechnung," ZAMM, vol. 7, 1927, pp. 451–452.

2 Tsien, H. S. and Evans, R. C., "Optimum Thrust Programming for a Sounding Rocket," *Journal of the American Rocket Society*, vol. 21, no. 5, 1951, pp. 99–107.

3 Leitmann, G., "Stationary Trajectories for a High-Altitude Rocket with Drop-Away Booster," *Astronautica Acta, II*, fasc. 3, 1956, pp. 119–124.

4 Hibbs, A., "Optimum Burning Program for Horizontal Flight," *Journal of the American Rocket Society*, vol. 22, no. 4, 1952, pp. 204–212.

5 Mayer, A., "Über das allgemeinste Problem der Variationsrechnung bei einer einzigen unabhängigen Variabeln," Leipziger Berichte, *XXX*, 1878, pp. 16–32.

6 Bolza, O., "Lectures on the Calculus of Variations," G. E. Stechert & Co., New York, 1946.

On Turbulent Heat Transfer Through a Highly Cooled Partially Dissociated Boundary Layer[1]

RONALD F. PROBSTEIN,[2] MAC C. ADAMS,[3] PETER H. ROSE[4]

Avco Research Laboratory, Everett, Mass.

IT IS the purpose of this note to present some analytical results regarding the properties of a compressible dissociating turbulent boundary layer in thermodynamic equilibrium. For brevity, detailed derivations are omitted and symbol definitions are given only when it is not clear what is meant.

Received October 13, 1957.

[1] A more detailed version of this paper including experimental results will be published at a later date. "This work was sponsored by the Ballistic Missile Division, Air Research and Development Command, U. S. Air Force, under Contract AF 04-(645)-18."

[2] Consultant. Also Associate Professor of Engineering, Brown University, Providence, R. I.

[3] Deputy Director. Mem. ARS.

[4] Principal Research Scientist.

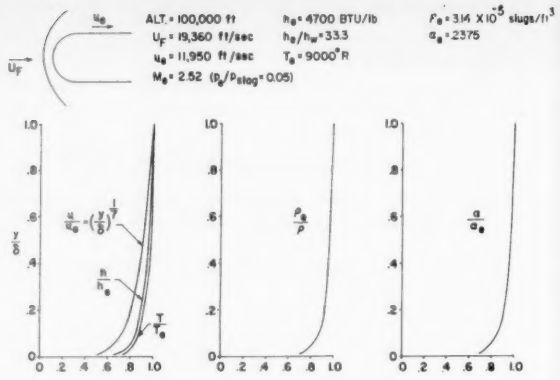

Fig. 1 Fluid property distributions through a highly cooled partially dissociated turbulent boundary layer.

Of interest are the mean continuity, momentum and energy equations for the plane or axisymmetric turbulent boundary layer in thermodynamic equilibrium. These can be derived from the general equations for a dissociating boundary layer (1)[5] by writing the fluid properties as the sum of a time averaged quantity plus a fluctuating quantity (e.g., $u = \bar{u} + u'$). If in addition we assume the Prandtl number $Pr = \bar{c}_p \mu / k = 1$, and the Lewis number, $Le = \bar{c}_p \rho D / k = 1$ (where D is the diffusion coefficient) these equations can be expressed in the usual form (2)

$$(\bar{\rho}\bar{u}r^j)_x + (\bar{\rho}\bar{v}r^j)_y + (\overline{\rho' v' r^j})_y = 0 \quad \ldots\ldots\ldots [1]$$

$$\bar{\rho}\bar{u}\bar{u}_x + (\bar{\rho}\bar{v} + \overline{\rho' v'})\bar{u}_y = -p_x + (\mu \bar{u}_y + \mu_T \bar{u}_y)_y \quad \ldots\ldots [2]$$

$$\bar{\rho}\bar{u}\bar{H}_x + (\bar{\rho}\bar{v} + \overline{\rho' v'})H_y = \left(\frac{k}{\bar{c}_p}\bar{H}_y + \frac{k_T}{\bar{c}_p}\bar{H}_y\right) \quad \ldots\ldots [3]$$

Here, r is the cross-sectional radius of the body with $j = 0$ for plane flow and $j = 1$ for axi-symmetric flow, $\bar{H} = \bar{h}_{ideal} + \bar{h}_{dissoc} + \bar{u}^2/2 = \bar{h} + \bar{u}^2/2$ is the total enthalpy, and $\mu_T = -\bar{\rho}\overline{u'v'}/\bar{u}_y$ is the eddy viscosity. In order to derive Equations [1–3] the additional definitions and assumptions not given in (2) are: (a) The eddy conductivity is defined as $k_T = -\dfrac{\bar{\rho}\overline{v'h'}}{\bar{h}_y/\bar{c}_p}$, and (b) the turbulent Lewis number $Le_T = D_T \bar{\rho} \bar{c}_p / k_T = 1$, with D_T the turbulent diffusion coefficient. Thus analogous to the fact that in a dissociating gas the heat transported by ordinary conduction and diffusion is $\dfrac{k}{c_p} h_y$ only for $Le = 1$, see (1), so too is the rate of energy transported by turbulent conduction and diffusion given by $-\bar{\rho}\,\overline{v'h'} = \dfrac{k_T}{\bar{c}_p}\bar{h}_y$ *only when* $Le_T = 1$. As with the turbulent Prandtl number, Le_T is probably nearer to unity than the laminar Lewis number.

If in addition to $Le = Pr = 1$, we have $Pr_T = \bar{c}_p \mu_T / k_T = 1$, then with $\dfrac{dp}{dx} = 0$, both the mean momentum and energy equations are similar. For either an insulated body or a constant surface enthalpy we immediately obtain the familiar Crocco integral between enthalpy and velocity

$$H = h_w + (H_e - h_w)\frac{u}{u_e} \quad \ldots\ldots\ldots [4]$$

where the bars have now been dropped, and the subscripts w and e represent conditions at the wall and edge of the bound-

[5] Numbers in parentheses indicate References at end of paper.

ary layer respectively. From this relation we note that for a highly cooled boundary layer the enthalpy and temperature distributions will not have a maximum within the layer as in the usual supersonic case with moderate temperature differences. This follows by differentiating Eq. [4] with respect to y and noting that since $u_y > 0$, then $h_y > 0$ if $(H_e - h_w)/u_e > u_e$. For large wall cooling where $h_w/H_e \to 0$, this implies $u_e^2/H_e < 1$ for $h_y > 0$. This condition will in general be satisfied on a blunt body in hypersonic flight where $u_e^2/H_e < 1$. Interpreted in terms of local external Mach number $u_e^2/He = 1$ corresponds to $M_e = 2.24$ for $\gamma = 1.4$ and $M_e = 3.16$ for $\gamma = 1.2$. In general other fluid properties such as density ρ, temperature T, etc., will follow the same trend as the enthalpy and will have no maximum. Some typical distributions of static enthalpy h, temperature, density, and degree of dissociation α, obtained using Eq. [4] are shown in Fig. 1 for the case of a highly cooled turbulent boundary layer in thermodynamic equilibrium with an assumed velocity profile of the form $u/u_e = (y/\delta)^{1/7}$. The nature of the distribution is not critical to the velocity profile so long as it is of the turbulent type, i.e., a full profile.

From Eq. [4] Reynold's analogy between heat transfer and skin friction follows; that is, the Stanton number defined with stagnation enthalpy instead of recovery enthalpy is

$$St = \frac{Nu}{\mathrm{Re}_x Pr} = \frac{q}{\rho_e u_e (H_e - h_w)} = \frac{\tau}{\rho_e u_e^2} = \frac{C_f}{2} \quad \ldots\ldots [5]$$

where Nu is the Nusselt number and Re_x the Reynolds number. For Prandtl numbers different from unity it is usual to apply a correction factor (3–4), which turns out to be approximately the same as for laminar flow, namely $St = \frac{C_f}{2} Pr^{-2/3}$.

Analogous to this laminar Prandtl number correction we may expect that a laminar Lewis number correction for values different from unity should also be applied for a dissociated flow. Such a correction is to be expected since, as indicated in Fig. 1, atom concentrations persist to the extremities of the laminar sublayer. The form of this correction can be seen by considering the heat flux crossing any plane which is

$$q = kT_y + D_A \rho h^\circ (c_A)_y \quad \ldots\ldots [6]$$

where h° is the dissociation energy per unit mass of atomic products, D_A the atomic diffusion coefficient, and c_A the atom mass fraction. From Eq. [6] we find that the heat transfer ratio is

$$\frac{q_{Le \neq 1}}{q_{Le = 1}} = 1 + \frac{(Le - 1)(h^\circ c_A)_y}{[h_{\text{ideal}} + h^\circ c_A]_y} \quad \ldots\ldots [7]$$

Now for the one-dimensional case of no convection in which we have linear distributions between a higher temperature surface and a cold wall Eq. [7] reduces to $(q_{Le \neq 1})/(q_{Le = 1}) = 1 + (Le - 1)h_{De}/H_e$, where h_{De} is the energy in dissociation at the high temperature surface, and $h_e = H_e$ the total enthalpy at this surface. On the other hand for a flat plate highly cooled laminar boundary layer this correction enters approximately as $1 + (Le^{2/3} - 1)h_{De}/H_e$, see (5) and (1), with the change in the exponent resulting from the convection present in the boundary layer. Without going into the detailed reasoning it can be shown that it is logical to assume for a highly cooled turbulent boundary layer where the profiles in the laminar sublayer are nearly linear that

$$\frac{q_{Le \neq 1}}{q_{Le = 1}} = 1 + (Le^\beta - 1)\frac{h_{De}}{H_e}, \quad \frac{2}{3} < \beta < 1 \quad \ldots\ldots [8]$$

with recourse to experiment required for the determination of the exact value of β.

With the previous considerations in mind it is now possible to formulate for a blunt body of revolution, for the practical hypersonic case of high wall cooling, a semi-empirical heat transfer rate theory dissociated turbulent boundary layers in thermodynamic equilibrium. The simplification follows from the fact that for such a case it is not difficult to show that the boundary layer behaves very much as an incompressible turbulent boundary layer (see Fig. 1), and the pressure gradient affects the boundary layer growth, but not markedly the shapes of the profiles. In particular it can be shown that so far as the skin friction coefficient is concerned the boundary layer behaves as if it were an incompressible constant property layer with a pressure gradient, so that it is justified to use the Blasius incompressible relation $C_f/2 = 0.0225\left(\frac{\nu_e}{u_e \delta}\right)^{\frac{1}{4}}$, and a velocity profile represented by a power law. Justification of this is based on the reasoning that: 1. The major changes in fluid properties occur through the laminar sublayer, which transmits the turbulent shear to the wall; 2. the shear is approximately constant through the sublayer; and 3. the boundary layer growth is practically unaffected by the sublayer, since only a small fraction of the total momentum is included there.

The boundary layer growth can now be determined utilizing the integrated momentum equation

$$\frac{d\theta}{dx} + \left(\frac{H_F + 2}{u_e}\frac{du_e}{dx} + \frac{1}{r}\frac{dr}{dx} + \frac{1}{\rho_e}\frac{d\rho_e}{dx}\right)\theta = \frac{\tau}{\rho_e u_e^2} = \frac{C_f}{2} \quad \ldots\ldots [9]$$

To integrate the above equation we require expressions for the momentum thickness θ, and the form factor $H_F = \delta^*/\theta$. Using Eq. [4] and a 1/7 power law these relations are found for a highly cooled blunt body to be; $\theta = (7/72)\delta(1.2)$. with 1.2 representing a mean value, and $H_F \ll 2$. Thus with $\theta = \theta(\delta)$ known and $H_F \approx 0$ we find on integrating Eq. [9] from $x = 0$ where wet set $\delta = 0$ that

$$\delta^{5/4} = \frac{0.289}{u_e^{5/2} r^{5/4} \rho_e^{5/4} (1.2)} \int_0^x \left(\frac{\nu_e}{u_e}\right)^{1/4} u_e^{5/2} r^{5/4} \rho_e^{5/4} dx \quad \ldots\ldots [10]$$

Utilizing Eq. [10], the Blasius skin friction relation, Eq. [5], and the Lewis and Prandtl number corrections, we can now write the final heat transfer equation for a highly cooled turbulent boundary layer subject to a pressure gradient as

$$\frac{Nu}{(Re_x)^{0.8}} = 0.029 Pr^{1/3} [F(x)]^{1/5} \left[1 + (Le^\beta - 1)\frac{h_{De}}{H_e}\right] \quad \ldots [11]$$

where we remind the reader that Nu and Re_x are based on properties at the edge of the boundary layer. Here $F(x)$ is a form factor for the pressure gradient effect and is given by

$$F(x)^{-1} = \frac{(u_e/\nu_e)^{1/4}}{u_e^{5/2} r^{5/4} \rho_e^{5/4}} \frac{1}{x} \int_0^x \left(\frac{\nu_e}{u_e}\right)^{1/4} u_e^{5/2} r^{5/4} \rho_e^{5/4} dx \quad \ldots [12]$$

Clearly $F(x) \to 1$ as $x \to \infty$ and $\frac{dp}{dx} \to 0$, as for example far downstream on a hemisphere cylinder. Furthermore it can be shown that $F(x)$ is always greater than 1 for a positive pressure gradient, and will always have a maximum in the region of maximum mass flow, and hence local Mach number of one.

References

1 Fay, J. A. and Riddell, F. R., "Theory of Stagnation Point Heat Transfer in Dissociated Air," Res. Rept. No. 1, Avco Research Laboratory, Everett, Mass., June 1956. (To be published in *Journal of the Aeronautical Sciences*, Jan. 1958).

2 Young, A. D., "Boundary Layers" in "Modern Developments in Fluid Dynamics, High Speed Flow," vol. I, (L. Howarth, Editor), Oxford, London, 1953, pp. 375–475.

3 Colburn, A. P., "A Method of Correlating Forced Convection Heat Transfer Data and a Comparison with Fluid Friction,"

Trans. Amer. Inst. Chem. Eng., vol. 29, 1933, pp. 174–210.

4 Rubesin, M. W., "A Modified Reynolds Analogy for the Compressible Turbulent Boundary Layer on a Flat Plate," NACA T.N. 2917, March 1953.

5 Lees, L., "Laminar Heat Transfer Over Blunt-Nosed Bodies at Hypersonic Flight Speeds," JET PROPULSION, vol. 26, April 1956, pp. 259–269.

Heat Transfer to a General Three-Dimensional Stagnation Point

ELI RESHOTKO[1]

California Institute of Technology, Pasadena, Calif.

The equations for the compressible laminar boundary layer at the stagnation point of a body having unequal principal curvatures are presented. A simple representation for the heat transfer to such a body is obtained for the case of the very cold wall. Estimates based on this representation are made for the heat transfer at other temperature levels.

Nomenclature

c_p	=	specific heat at constant pressure
F	=	$f\sqrt{1+K}$
f, g	=	stream functions for similar solutions
H	=	enthalpy
K	=	ratio of principal velocity gradients (Eq. [11])
k	=	thermal conductivity
Pr	=	Prandtl number
p	=	pressure
q	=	heat transfer rate to wall
$\mathcal{R}$	=	gas constant
R_x, R_z	=	principal radii of curvature
T	=	temperature
U, W	=	transformed velocity in X and Z directions, respectively
u, v, w	=	velocities in x, y, and z directions, respectively
X, Z	=	transformed coordinates along body surface
x, z	=	coordinates along body surface
Y	=	transformed normal coordinate
y	=	normal coordinate
η	=	boundary layer similarity variable
θ	=	$\dfrac{H - H_w}{H_0 - H_w}$
λ	=	$\eta\sqrt{1+K}$
ρ	=	density
μ	=	absolute viscosity
ν	=	kinematic viscosity
φ, ψ	=	components of stream function

Subscripts

e	=	local condition outside boundary layer (external)
sp	=	stagnation point value
w	=	wall value
0	=	free-stream stagnation value
∞	=	free-stream static value

A coordinate symbol used as a subscript generally denotes partial differentiation with respect to that coordinate.

Boundary Layer Equations

THE COORDINATE system chosen is shown in Fig. 1. In the vicinity of the stagnation point, these coordinates are Cartesian. The pertinent compressible boundary layer equations are

Continuity

$$(\rho u)_x + (\rho v)_y + (\rho w)_z = 0 \quad \ldots\ldots [1]$$

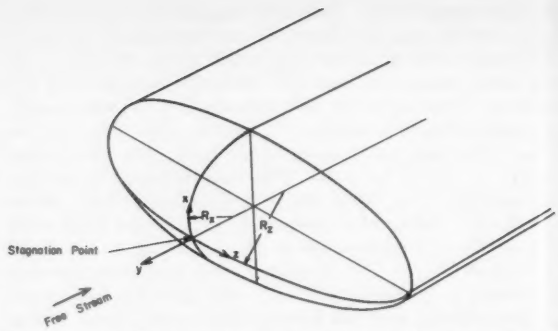

Fig. 1 Coordinate system for general three-dimensional stagnation point

Momentum

$$\rho u u_x + \rho v u_y + \rho w u_z = \rho_e x \left[\left(\frac{du_e}{dx}\right)_{sp}\right]^2 + (\mu u_y)_y \quad \ldots\ldots [2a]$$

$$p_y = 0 \quad \ldots\ldots [2b]$$

$$\rho u w_x + \rho v w_y + \rho w w_z = \rho_e z \left[\left(\frac{dw_e}{dZ}\right)_{sp}\right]^2 + (\mu w_y)_y \quad \ldots [2c]$$

Energy

$$\rho u \theta_x + \rho v \theta_y + \rho w \theta_z = \left(\frac{\mu}{Pr}\,\theta_y\right)_y \quad \ldots\ldots [3]$$

State

$$p = \rho \mathcal{R} T \quad \ldots\ldots [4]$$

The boundary conditions for these equations are

$$\text{At } y = 0 \qquad u = v = w = \theta = 0$$
$$y \to \infty \qquad u = u_e,\ w = w_e,\ \theta = 1$$

The viscosity is assumed to be a linear function of the temperature according to the relation

$$\mu = \frac{\mu_w}{T_w} T \quad \ldots\ldots [5]$$

The velocities in Equations [1 and 2] can be replaced through the definition of the two component stream functions (ψ, φ)

$$\psi_y = \frac{\rho u}{\rho_0} \qquad \psi_x + \varphi_z = -\frac{\rho v}{\rho_0} \qquad \varphi_y = \frac{\rho w}{\rho_0} \quad \ldots\ldots [6]$$

Equations [6] automatically satisfy the continuity equation.

Upon making the transformation of coordinates

$$X = \int_0^z \left(\frac{\mu_w T_0}{\mu_0 T_w}\right) dx \qquad Y = \int_0^y \frac{\rho}{\rho_0}\, dy \qquad Z = \int_0^z \left(\frac{\mu_w T_0}{\mu_0 T_w}\right) dz$$
$$\ldots\ldots [7]$$

and introducing the following similarity transformation

$$\psi = f(\eta) x \sqrt{\nu_0 \left(\frac{dU_e}{dX}\right)_{sp}} \qquad \varphi = Kg(\eta) z \sqrt{\nu_0 \left(\frac{dU_e}{dX}\right)_{sp}}$$
$$\eta = Y \sqrt{\frac{(dU_e/dX)_{sp}}{\nu_0}} \quad \ldots\ldots [8]$$

Equations [1–3] reduce to the ordinary differential equations

$$f''' + (f + Kg) f'' = f'^2 - 1 - \left(\frac{H_w}{H_0} - 1\right)(1 - \theta) \quad \ldots [9a]$$

$$g''' + (f + Kg) g'' = K\left[g'^2 - 1 - \left(\frac{H_w}{H_0} - 1\right)(1 - \theta)\right]$$
$$\ldots\ldots [9b]$$

$$\theta'' + Pr(f + Kg)\theta' = 0 \quad \ldots\ldots [9c]$$

Received November 12, 1957.

[1] Guggenheim Aeronautical Laboratory. On leave of absence from Lewis Flight Propulsion Laboratory, NACA.

with boundary conditions

$$\text{At } \eta = 0 \quad f = f' = g = g' = \theta = 0$$
$$\eta \to \infty \quad f' = g' = \theta = 1 \qquad [10]$$

The parameter K in Equations [9] is related to the principal velocity gradients

$$K = \frac{(dW_e/dZ)_{sp}}{(dU_e/dX)_{sp}} = \frac{(dw_e/dz)_{sp}}{(du_e/dx)_{sp}} \qquad [11]$$

It is readily seen from Equations [9 and 11] that the case $K = 0$ corresponds to the two-dimensional stagnation point while $K = 1$ represents the axially-symmetric stagnation point. If the X coordinate is identified with the larger principal curvature then all stagnation points have $0 \leq K \leq 1$.

For incompressible flow, H_w/H_0 is taken as unity in Equations [9a and 9b]. The resulting equations were originally obtained and numerically solved by Howarth (1).[2] In principle, [9] with boundary conditions [10] can be solved for many values of K, H_w/H_0, θ and Prandtl number. It was suggested by Professor L. Lees, however, that perhaps a simple solution could be obtained for the very cold wall where $H_w/H_0 \ll 1$. This is in fact the case.

Solution for Very Cold Wall

For $H_w/H_0 = 0$, Equations [9] become

$$f''' + (f + Kg)f'' = f'^2 - \theta \qquad [12a]$$

$$g''' + (f + Kg)g'' = K(g'^2 - \theta) \qquad [12b]$$

$$\theta'' + Pr(f + Kg)\theta' = 0 \qquad [12c]$$

It has already been shown in (2) that at this temperature level the right hand sides of [12a] and [12b] have a small effect on heat transfer and for simplicity can be neglected. Equations [12] then become

$$f''' + (f + Kg)f'' = 0 \qquad [13a]$$

$$g''' + (f + Kg)g'' = 0 \qquad [13b]$$

$$\theta'' + Pr(f + Kg)\theta' = 0 \qquad [13c]$$

Since the functions f and g satisfy the same boundary conditions (see Eq. [10]), then for Equations [13], $f = g$, and Equations (13) become

$$f''' + (1 + K)ff'' = 0 \qquad [14a, b]$$

$$\theta'' + Pr(1 + K)f\theta' = 0 \qquad [14c]$$

Now let $F = f\sqrt{1 + K}$ and $\lambda = \eta\sqrt{1 + K}$. Equations [14] then reduce to the Blasius equation and its accompanying energy equation

$$\left.\begin{aligned} F_{\lambda\lambda\lambda} + FF_{\lambda\lambda} &= 0 \\ \theta_{\lambda\lambda} + PrF\theta_\lambda &= 0 \end{aligned}\right\} \qquad [15]$$

which have the well-known wall values $(F_{\lambda\lambda})_w = 0.470$ and, for $Pr = 1$, $(\theta_\lambda)_w = 0.470$. Returning then to the functions of Equations [14]

$$\left.\begin{aligned} f_w'' &= 0.470\sqrt{1 + K} \\ (\theta_w')_{Pr=1} &= 0.470\sqrt{1 + K} \end{aligned}\right\} \qquad [16]$$

Calculation of Heat Transfer

The local rate of heat transfer per unit area to a stagnation point is expressed

$$q = \frac{k_w}{c_p}\theta_w' Pr^{0.4}\sqrt{\frac{\rho_w}{\mu_w}\left(\frac{du_e}{dx}\right)_{sp}}(H_0 - H_w) \qquad [17a]$$

or

$$q = \theta_w' Pr^{-0.6}\sqrt{\rho_w\mu_w\left(\frac{du_e}{dx}\right)_{sp}}(H_0 - H_w) \qquad [17b]$$

where the value of θ_w' is that for Prandtl number 1 and may be read from Fig. 2. The lowest curve in Fig. 2 is that of Eq. [16]. The other curves are estimates based on [16] of the variation of θ_w' for $H_w/H_0 = 0$, 1, 2 where the end-points are obtained from the exact solutions of (3–5) for two-dimensional and axially-symmetric stagnation points. The variation of heat transfer at the stagnation point with Prandtl number is included in Equations [17] as $Pr^{0.4}$.

The velocity gradient $(du_e/dx)_{sp}$ is possibly evaluated from modified Newtonian flow using the expression

$$\left(\frac{du_e}{dx}\right)_{sp} = \sqrt{\frac{2}{R_x}\left(\frac{p_{sp} - p_\infty}{\rho_s p}\right)} \qquad [18]$$

where R_x is the smaller principal radius of curvature. The ratio of velocity gradients K is related to the principal radii of curvature by the expression

$$K = \sqrt{\frac{R_x}{R_z}} \qquad [19]$$

The effects of dissociation for Lewis number of one can be roughly accounted for by using external fluid properties in place of the wall fluid properties in Eq. [17b] as was done in (2). A better approximation to the effects of dissociation would be obtained through multiplying the right side of [17b] by $(\rho_s\mu_e/\rho_w\mu_w)^{0.4}$ (Reference 6).

References

1 Howarth, L., "The Boundary Layer in Three Dimensional Flow,"—Part II. "The Flow Near a Stagnation Point," *Philosophical Magazine*, vol. 7s, no. 42, 1951, pp. 1433–1440.

2 Lees, Lester, "Laminar Heat Transfer over Blunt-Nosed

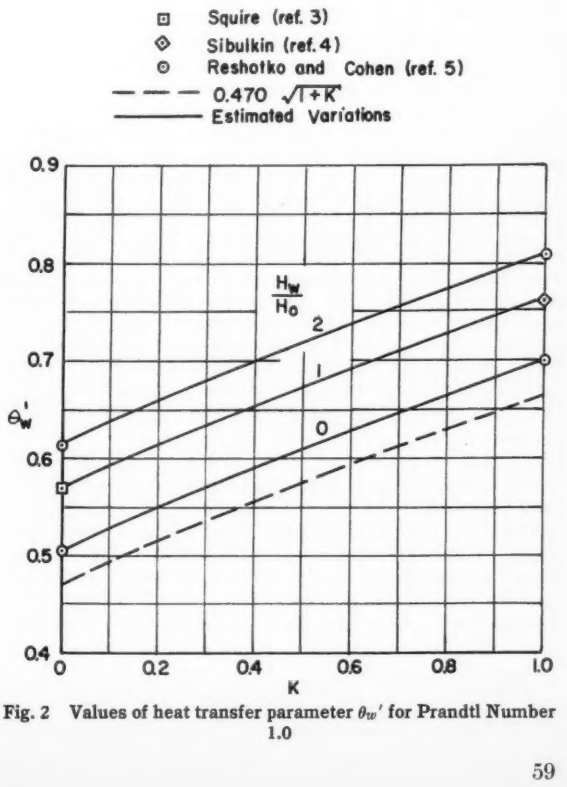

Fig. 2 Values of heat transfer parameter θ_w' for Prandtl Number 1.0

[2] Numbers in parentheses indicate References at end of paper.

Bodies at Hypersonic Flight Speeds," JET PROPULSION, vol. 26, no. 4, April 1956, pp. 259–269.

3 Goldstein, Sydney, editor, "Modern Developments in Fluid Dynamics," vol. II, First edition. Clarendon Press (Oxford), 1938, p. 631.

4 Sibulkin, M., "Heat Transfer Near the Forward Stagnation Point of a Body of Revolution," *Journal of the Aeronautical Sciences*, vol. 19, no. 8, August 1952, p. 570.

5 Reshotko, Eli and Cohen, Clarence B., "Heat Transfer at the Forward Stagnation Point of Blunt Bodies," NACA TN 3513, 1955.

6 Fay, J. A. and Riddell, F. R., "Stagnation Point Heat Transfer in Dissociated Air," AVCO Research Laboratory, Research Note 18, June 1956.

On the Rational Choice of Flame-Holder Shape

ABBOTT A. PUTNAM[1]

Battelle Memorial Institute, Columbus, Ohio

IN DESIGNING a flame-holder system, the first requirement is that the flame-holder system be capable of maintaining a stable flame over a given range of mixtures and flow velocities. Next, this flame must propagate across the mixture from the holders so that all the fuel is consumed. Finally, combustion should take place with minimum pressure losses and in a system of minimum length.

For simplicity, let us consider a combustor in which the most stringent requirement is related to flow velocity and to mixture ratio, and the length of the combustor is fixed. Because a flame can spread only so fast in a stream, the fixed length of combustor fixes the area served by each component of a grid flame holder. In an open system, the larger the flame holder the greater the velocity of final instability (1).[2] However, when the flame holder is in a restricted region, the flow velocity past the flame holder increases as its size increases, for a fixed average flow velocity over the entire cross section. Thus, a point will be reached where increasing the size is not beneficial. It follows that for each shape of flame holder, and each mixture ratio, a curve may be drawn giving the maximum average flow velocity that may be obtained in a fixed size of duct or associated area.

Fig. 1 shows plots of such curves for two different configurations of flame holder, designated by F and U, as a function of reciprocal area of the duct. Since all operating conditions of a given shape must fall below the corresponding curve on this plot, these curves may be termed envelope curves. The relative positions of the curves are related to the angle between the initial flame front and the flow direction (2).

If the design condition is such that only one shape of holder will satisfy the flame-holding requirements, then there is no further problem. The shape has been fixed. However, suppose that several holders will satisfy the requirements. Then, the advantages of one shape relative to another must be weighed. The question of flame-holder drag must be considered.

Fig. 2 gives an indication of the variation of drag for a given shape of flame holder. The dashed curve, corresponding to either envelope curve of Fig. 1, may be considered to be composed of infinitesimal segments of curves of constant drag force. The left-hand parts of two such curves of constant drag force are shown as solid lines; the right-hand parts are not indicated because a greater flame-holding ability can be obtained with smaller drag using a smaller holder in the right-

Received July 26, 1957.

[1] Assistant Chief, Aeronautics and Thermodynamics Div. Mem. ARS.

[2] Numbers in parentheses indicate References at end of paper.

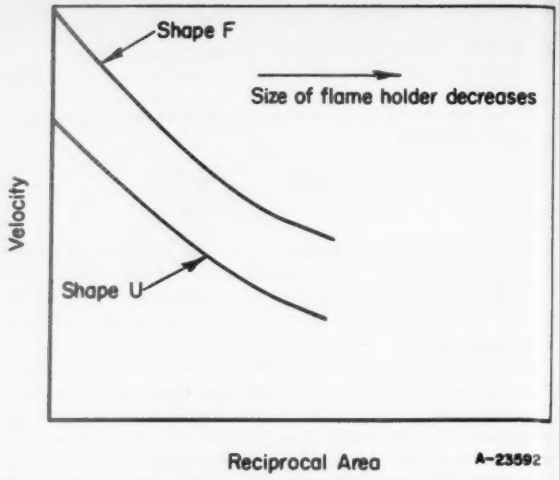

Fig. 1 Curves of maximum flame-holding ability for two shapes of flame holder

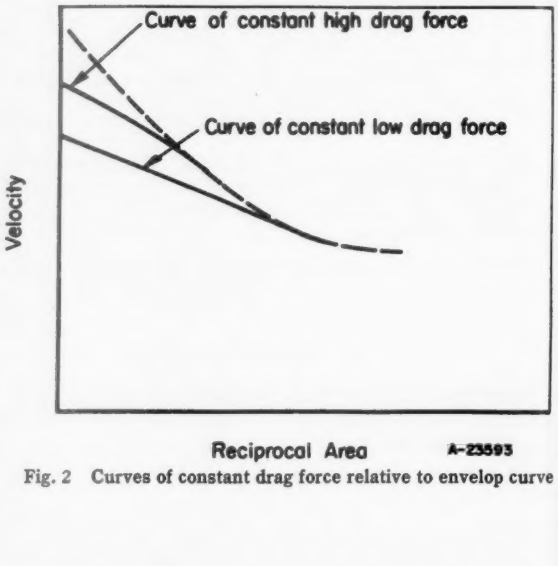

Fig. 2 Curves of constant drag force relative to envelop curve

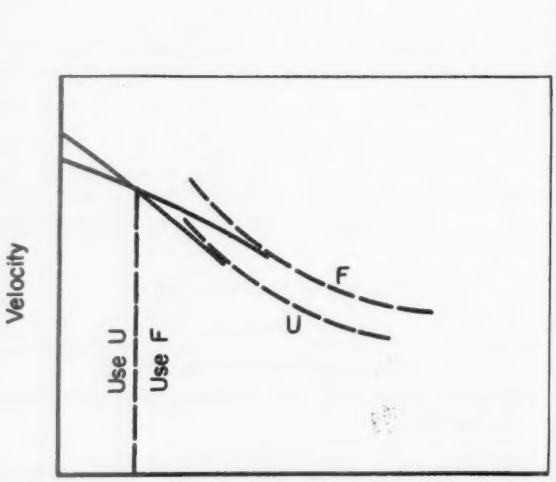

Fig. 3 Curves of constant drag holding for two shapes

hand region. It is seen from this figure that savings in drag force can be obtained by not overdesigning a holding system.

The next question is whether it is better (a) to use the shape of holder, the envelope curve of which just meets the design requirements, or (b) to use a shape, the envelope of which is too high, but use a smaller size holder with a lower drag. This question is answered in (3) for the case $1/S = 0$, that is, for a holder in an infinitely wide stream. For minimum drag, one should use the shape associated with the lowest envelope curve that will meet the requirements.

Fig. 3 shows the extrapolation of this information to finite values of duct area. A drag force is chosen, and then the curves of constant drag force are drawn. For $1/S \rightarrow 0$, shape U should be used to obtain the maximum flame-hold ability for a given amount of drag, or minimum drag for a given amount of flame-holding ability. For $1/S \rightarrow \infty$, or $S \rightarrow 0$, shape F should be used The change-over point is a function of the design velocity.

These considerations demonstrate that, to make a scientific decision as to the optimum shape of flame holder to choose, the flame-holding ability and hot drag of various shapes of flame holders must be known as a function of both flame-holder size and duct size.

References

1 Kutzko, G. G., "Investigation of Limits of Flame Stability of Disk Flame Holders in Free Stream," WADC Technical Report 55-134 (May 1955).

2 Putnam, A. A., "Effect of Boundary Layer Thickness on Flame Stability," *Fuel*, vol. 33, no. 3, July 1954, p. 355.

3 Kutzko, G. G., "Investigation of Flame Stability and Drag Losses for Flame Holders on a Free Stream," WADC Technical Report 55-429 (November 1955).

Book Reviews

Ali Bulent Cambel, Northwestern University, *Associate Editor*

Physical Measurements in Gas Dynamics and Combustion, edited by R. W. Ladenburg (Part 1) and B. Lewis, R. N. Pease and H. S. Taylor (Part 2); Volume IX, High Speed Aerodynamics and Combustion, Princeton University Press, Princeton, N. J., 1954. $12.50.

Reviewed by F. H. Wright
Jet Propulsion Laboratory

"Physical Measurements in Gas Dynamics and Combustion" contains a wealth of information about experimental techniques and supplies sufficient background material to permit intelligent application of the techniques. A refreshing feature of the book is the choice of authors. The twenty-two authors of the several sections have developed the methods they write about, or have had long experience in their practical application. As a result, they write with vigor and authority and in a way that makes interesting reading.

This book is much more than a handbook for the experimentalist—it is also a book for the general reader. It succeeds in reaching both audiences. However, it is not completely successful in coping with the duality of presentation required. The task of satisfying both audiences is an almost impossible one. For the experimentalist, complete information on each method is required, either within an article, or in easily available references. Evaluation of techniques, analysis of accuracies, delineation of fields of application, critical discussion of references and comparison of a method with other ways of performing the same task are also needed. Further, the experimentalist wishes the author to share his wealth of experience with the reader, suggesting experimental tricks and pointing out pitfalls.

On the other hand, for the general reader many of the practical details are unnecessary. The general reader needs a book that describes the experimental methods in a simple fashion that will lead him to an understanding of the object of experimentation, and that will help him to interpret experimental results. He requires discussion of the quantities to be measured, of the possible lines of attack on the problems and of the principle experimental techniques and attainable accuracies.

However, an abundance of detail is provided for the worker who plans to use the methods, and there are presented without boring the general reader. But the experimentalist, particularly the novice, will have difficulty in applying some of the methods. Expanded analysis and cataloguing of the references, perhaps designating the basic and important references by asterisks, would have helped to supplement the necessarily concise text. Also, more discussion of the details and tricks not readily found in references would have been greatly appreciated by the experimenter.

Little space is devoted to the orientation of the general reader. There is no introductory chapter to acquaint the reader with the important properties to be measured in high speed and combustion flows and with the circumstances of measurement. An introductory chapter might also have outlined the methods of measurement and compared them. It might have indicated possible accuracies and ranges of applicability. In addition to this general introduction, introductory chapters for the several divisions of the book would have been valuable. The first chapter of the book, is, indeed, an introduction to optical methods, supplying the necessary theoretical background for interferometric schlieren and shadow methods. A similar but less theoretical chapter for each of the other divisions would have been appropriate. All divisions would have benefited from discussion of the quantities to be measured, conditions of measurement and comparison of possible techniques. An introduction would also have provided the opportunity for relating one division to other portions of the book, showing relations between measured quantities and comparing widely differing techniques.

Both the experimentalist and the general reader should be pleased with the coverage provided by this book. Personal preference might, in particular instances, dictate a different choice of subject matter but there can be no great quarrel about the selection that has been made. The present reviewer, for example, would like to have seen the section on pressure measurements expanded. He would also like to have seen more discussion of flow visualization techniques, which frequently provide the avenues of approach to understanding the phenomena in new and complex fields. Space in the book might also have been found for methods of measurement of fluid properties such as humidity, composition, etc.

These criticisms are minor and the authors are to be congratulated on the articles they have produced. All of the chapters are scientifically sound and concisely provide the necessary information. Several chapters are superb. This book is recommended both as an introduction to the experimental methods of high speed gas dynamics and combustion and as a reference for an experimentalist working in these fields.

Thermodynamics and Statistical Mechanics, by A. H. Wilson, Cambridge University Press, New York, 495 pp. $9.50.

Reviewed by E. F. Obert
Northwestern University

There are so many books on thermodynamics and statistical mechanics that each new book should have a definite objective and a definite place in the literature. This new book by A. H. Wilson ful-

fills these prerequisites since it is directly aimed at the theoretical physicist and presents a detailed but compact survey of the subjects of thermodynamics and statistical mechanics and their interrelationships. The engineer in research or in teaching will find the book to be valuable since the physical significance of the various steps in analysis is emphasized while the mathematical detail is minimized. Thus the presentation stresses the salient points of thermodynamics as illustrated by the statistical mechanics, without the intervention of detail which elementary texts must include for full understanding.

The first three chapters would seem to belie the objectives since classical thermodynamics is covered through a considerable range of elementary as well as advanced topics. The concepts of temperature, the first and second laws and equilibrium are discussed briefly in the usual manner, with greater detail paid to the stability requirements of homogeneous substances. But starting with Chapter Four entitled, "The Axiomatic Foundation of Thermodynamics," the diversity of coverage and the objectives of the author come alive. Here temperature and the first and second laws are adequately reviewed in the axiomatic manner of Caratheodory following the simplified analysis of Born. In Chapter Five "Statistical Mechanics," the fundamental concepts of statistical mechanics, are reviewed briefly and then applied to obtain the concepts, first, of temperature and then of entropy, and other thermodynamic functions. The chapter is completed by sections on the perfect gas, the transition to classical mechanics, and the quantal statistical mechanics.

Chapter Six, "Some Applications of Statistical Mechanics," reviews the specific heats of gases, crystalline solids, Fermi-Dirac and Einstein-Bose systems as prerequisite material for Chapter Seven, "The Third Law of Thermodynamics." The discussion of the third law is excellent (and illustrates why the author emphasized certain topics in previous chapters). Chapter Eight, "Imperfect Gases," is also an excellent and complete job and discusses the behavior of gases from the empirical through the thermodynamic aspects with added discussion from the viewpoint of statistical mechanics.

The diversity of coverage is shown by the topics in the remainder of the book: Equilibria, the properties of helium, electric and magnetic phenomena, polar substances, superconductivity, gas mixtures, chemical reactions, solutions and solids.

Whether or not the book will appeal to the theoretical physicist must be answered by a member of that group; this reviewer is of the opinion that the book will be a valuable addition to the library of the engineer engaged in teaching or research since it is one of the relatively few books in thermodynamics which stresses the physics, rather than the chemistry of the subject, and supplies immediately the added information offered by the statistical mechanics.

Thermal Stresses, by B. E. Gatewood, McGraw-Hill Book Company, Inc., New York, 1957, 247 pp. $7.50

Reviewed by P. N. Stevens
Convair-Fort Worth

This book is based on a course which the author gave to graduate aeronautical engineering students at the Air Force Institute of Technology. The author presents a comprehensive approach which is not restricted only to the classical elastic thermal stress problem. All phases of the structural design problem are investigated and includes areas such as the temperature distribution, the elastic and inelastic applied and thermal stresses, allowable stresses, and various effects of elevated temperatures.

In Chapter 1, the author gives the thermal-stress equations, starting with simple cases and building up to the general three-dimensional equations. In the rest of the book, reference is made to Chapter 1 for the thermal-stress formulas. Chapter 2 gives the temperature equations for heat conduction, heat radiation, heat convection and aerodynamic heating, and ap-

JET PROPULSION
AND
JOURNAL OF THE BRITISH INTERPLANETARY SOCIETY

now available from their first year of publication

By arrangement with *The American Rocket Society* and *The British Interplanetary Society*, KRAUS REPRINT CORPORATION has just re-issued these two important journals from vol. 1 and thus made available to research programs the most comprehensive source of technical information in the entire Rockets and Missiles field.

JET PROPULSION
Complete set, vols. 1-22, 1930-1952
bound in library buckram $148.50

JOURNAL OF THE BRITISH INTERPLANETARY SOCIETY
Complete set, vols. 1-14, 1934-1955
bound in library buckram $180.00

All single volumes of both journals available separately. Please ask for detailed price list.

Jet Propulsion vols. 23-26 (1953-1956) scheduled for reprint early 1958.

Please order now.

Single back issues, as far as still available in the original edition, should be ordered from:

BACK ISSUES CORPORATION
805 Mamaroneck Avenue, Mamaroneck, N. Y.

KRAUS REPRINT CORPORATION, 16 E. 46TH ST., NEW YORK 17, N.Y.

plies them to obtain the heat-balance equations for an idealized structural element on a typical aircraft or missile structure. Reference is made in the later chapters to the temperature equations in Chapter 2.

In Chapter 3 the temperatures and thermal stresses for an idealized structural element consisting of a skin element at one uniform temperature joined to a stringer element at a different uniform temperature are determined. In this case time is the only independent variable for the idealized element. With certain assumptions concerning the aerodynamic heating of the skin element, the heat radiation to the stringer, and the thermal resistance of the joint between the skin and the stringer, analytical solutions for the temperature and thermal stress are obtained. The important parameters involving geometry, material properties and time are determined, and curves of maximum stress against these parameters are constructed.

In Chapter 4 the procedures of Chapter 3 are extended to the case of one-dimensional temperature and thermal-stress variation. With time and the thickness dimension as independent variables, analytical solutions are obtained for a thick plate or a beam or a multiweb box beam of an aircraft structure. Chapter 5 gives some of the simpler two-dimensional thermal-stress problems of particular interest, but the general two-dimensional problem is considered in Chapter 9.

Chapter 6 is devoted to material properties, allowable stresses under various loading conditions, and efficiencies of materials at elevated temperatures. Some discussion of thermal fatigue and thermal shock of materials also is given. In Chapter 7 the stress-analysis problem of combining the applied stresses, thermal stresses and allowable stresses is considered. Particular emphasis is put on the inelastic thermal stresses, the inelastic combination of applied and thermal stresses and the time at which the applied and thermal stresses are combined. In Chapter 8 the deflection and stiffness of the structure under elevated temperatures and thermal stresses are considered. Simple procedures are given to determine the approximate deflection and stiffness of the structure and the resultant effects upon the thermal stresses and upon flutter.

In Chapter 9 some cases of the general two-dimensional thermal-stress problem are considered. In particular the energy and complex-variable methods are discussed and applied to several problems.

It is the reviewer's opinion that this book fulfills in part the general need for a comprehensive coverage of the general general stress problem. However, the basic information and problem-solution procedures presented lean heavily toward the aircraft structures field and are not directly relatable to problem areas in the nuclear and other fields. The basic difference is in the heat generation source terms and in the materials of construction. It is felt that additional emphasis should have been given to these problem areas because of the strong influence imposed by the thermal stress problem on all nuclear reactor design considerations.

When you need an aluminum fuel pump this big for your rocket to the moon, Morris Bean & Company will cast it for you.

Actually, no such casting exists.

It could.

We have developed unique foundry techniques which we now use in production on castings weighing thousands of pounds. These castings have extensive areas 9 to 12 inches thick which must be porosity free.

We are also casting solid and hollow mandrels used to form solid propellant.

The outstanding contribution of our large aluminum castings is drastically reduced first and ultimate costs.

Telephone or write for information now.

Morris Bean & Company
Yellow Springs 6, Ohio

large aluminum castings!

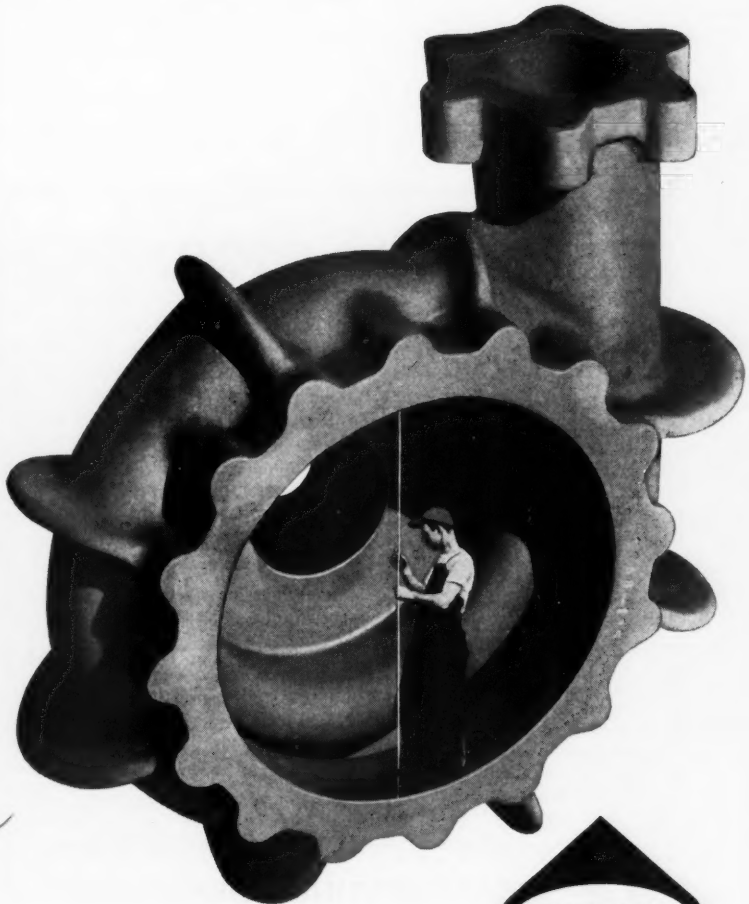

BEAN

New Patents

George F. McLaughlin, *Contributor*

Turbojet driven helicopter (2,811,324). Ralph P. Alex, Fairfield, Conn., assignor to United Aircraft Corp.

Gas turbine engine mounted on a gear box aft of the rotor shaft, its jet discharge directed rearwardly. The power shaft is directed forwardly toward the rotor shaft.

Variable area nozzle (2,811,831). Frederick L. Geary and Wm. Taylor Jr., South Glastonbury, Conn., assignors to United Aircraft Corp.

Flaps pivotally mounted on a ring around the outlet. Bell crank levers mounted on the outlet duct, one for each flap, are connected to actuate adjacent flaps for varying the outlet area.

Combustor for turbine of aircraft starter (2,811,832). Cameron D. Flanigen and Robert Wiedis, Maywood, N. J., assignors to Bendix Aviation Corp.

A compact combustor to provide gases to the turbine of a jet engine starter. A turbulator plate provides an annular inclined passage for air moving in pocket-like louvres projecting into a bowl-shaped combustion chamber.

Turbine cooling (2,811,833). Wilgus S. Broffitt, Indianapolis, Ind., assignor to General Motors Corp.

Conduits conduct cooling air from outer air jackets to a chamber at the front of the turbine rotor. A ring adjacent the chamber has passages rotatable in and out of registery with the conduits to control the delivery of air from the conduits to the chamber.

Turbine blade cooling systems (2,812,157). Wm. A. Turunen, Patrick W. O'Connell and De Owen Nichols Jr., Ann Arbor, Mich., assignors to General Motors Corp.

Rotor blades each with a coolant passage in its central portion sealed at its outer end. Radially extending passages in the turbine wheel communicate with passages in the blades. A duct from a condenser chamber conveys coolant from the turbine wheel passage to the chamber.

Jet engine or gas turbine with electric ignition (2,811,676). W. B. Smits, Voorburg, Netherlands, assignor to Smitsvonk N. V.

Low voltage surface discharge spark plug for each burner, connected in series. Condensers, sequentially connected with a source of electrical energy, fire atomized fuel associated with each plug.

Process for preparing a liquid oxygen explosive (2,812,246). Samuel W. Martin, Oak Park, Ill., assignor to Great Lakes Carbon Corp.

Method comprises preparing a hard, granular nonactivated absorbent carbon by the thermal expansion of finely divided bituminous coal suspended in liquid oxygen. The oxygen contains gas maintained at a temperature about 1200 to 1700 C, and an upheat rate higher than 1000 C per sec.

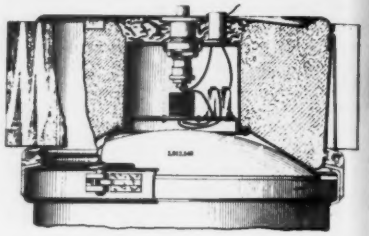

Delayed opening parachute pack (2,812,148). Gordon L. Fogal and Graham B. Brown, Alexandria, Va.

Mechanism for releasing a parachute from a pack in response to barometric pressure corresponding to a preselected altitude. Firing of an explosive charge, operated by switches, causes separation of the chute from the pack.

Pulse jet engines with rearwardly opening air inlet (2,812,635). J. Le Foll and J. H. Bertin, Neuilly-sur-Seine, France, assignors to SNECMA Co.

Air inlet connected to one end of the combustion chamber and having an orifice facing toward the rear. An exhaust pipe is fed solely from the chamber. A pipe bend of 180 deg connects the beginning of the exhaust pipe with the other end of the chamber to form a continuous gas conveying duct.

Process and device for deflecting jets (2,812,636). M. Kadosch, F. G. Paris, J. H. Bertin and R. H. Marchal, Paris, France, assignors to SNECMA Co.

Outwardly curved convex extension of a wall of a propulsive nozzle in which fluid is blown in a tangent direction. A valve controls the supply of pressure fluid to the blowing means.

Fuel air ratio regulation for combustion systems (2,812,637). Homer M. Fox, Bartlesville, Okla., assignor to Phillips Petroleum Co.

System of recovering low pressure and high pressure air streams from a combustion apparatus. Means for flowing any stoichiometric excess of air from the high pressure air stream to the low pressure air stream.

Fuel system (2,812,715). Arnold H. Redding and Donald F. Winters, Folsom, Pa., assignors to Westinghouse Electric Corp.

Fuel tank pump for providing a predetermined head pressure in the supply conduit. A valve in the recirculation conduit is responsive to a fuel demand signal to control recirculation of fuel pumped in excess of the quantity demanded by the engine.

Gas turbine engines (2,812,897). L. Mc T. Cameron, Bristol, England, assignor to The Bristol Aeroplane Co.

Ring of hollow inlet guide vanes in the air intake. Air from the compressor is led to the interior of the vanes, and conduits lead heat into exchange relationship with the turbine.

EDITORS NOTE: Patents listed above were selected from the Official Gazette of the U. S. Patent Office. Printed copies of Patents may be obtained from the Commissioner of Patents, Washington 25, D. C., at a cost of 25 cents each; design patents, 10 cents.

DATA PROCESSING SPECIALISTS!

Get in now—at the beginning of the new era in missiles!

When you join Telecomputing's Engineering Services Division, you will be given full scope to allow you to grow...your talents will be used to the fullest... recognition and rewards will be yours as a matter of course.

Engineering services is a member of an integrated five-company missile systems corporation which designs and manufactures its own data-processing equipment. Our efforts are directed toward the "systems concept." We are engaged in the reduction of large amounts of flight test data being generated by the daily missile firings on the integrated Holloman-White Sands range.

ATTRACTIVE SALARIES
PROFIT SHARING

RELOCATION PAY
ACCREDITED EDUCATION
GROUP INSURANCE

A NEW LIFE IN NEW MEXICO'S FABULOUS "LAND OF ENCHANTMENT"

MOUNTAIN SKIING AND DESERT RESORTS WITHIN 30 MINUTES!

A WONDERFUL PLACE TO MAKE YOUR HOME — GRAND COUNTRY TO RAISE KIDS!

Send resume to Director of Technical Personnel

TELECOMPUTING CORPORATION
Engineering Services Division
BOX 447 • HOLLOMAN AIR FORCE BASE • NEW MEXICO

DOUBLE DIAGNOSIS TO PREVENT "HEART DISEASE"

...BY THE B&H JETCAL® ANALYZER

Two of the most important factors that affect jet engine life, efficiency, and safe operation are *Exhaust Gas Temperature (EGT)* and *Engine Speed (RPM)*. Excess heat will reduce "bucket" life as much as 50% and low EGT materially reduces efficiency and thrust. Any of such conditions will make operation of the aircraft both costly and dangerous. The *JETCAL Analyzer predetermines* accuracy of the EGT and (interrelatedly) Tachometer systems and isolates errors if they exist.

The *JETCAL* ANALYZES JET ENGINES 10 WAYS:

1) The JETCAL Analyzer *functionally* tests EGT thermocouple circuit of a jet aircraft or pilotless aircraft missile for error *without running the engine or disconnecting any wiring*. GUARANTEED ACCURACY is ±4°C. at engine test temperature.

2) Checks individual thermocouples "on the bench" before placement in parallel harness.

3) Checks thermocouples within the harness for continuity.

4) Checks thermocouples *and* paralleling harness for accuracy.

5) Checks resistance of the Exhaust Gas Temperature system.

6) Checks insulation of the EGT circuit for shorts to ground and for shorts between leads.

7) Checks EGT Indicators (in or out of the aircraft).

8) Checks EGT system with engine removed from aircraft (in production line or overhaul shop).

9) Reads jet engine speed while the engine is running with a guaranteed accuracy of ±0.1% in the range of 0-110% RPM. Additionally, the TAKCAL circuit can be used to trouble shoot and isolate errors in the aircraft tachometer system.

10) JETCAL Analyzer enables engine adjustment to proper relationship between engine temperature and engine RPM for maximum thrust and efficiency during engine run (Tabbing or Micing).

ALSO *functionally* checks aircraft Over-Heat Detectors and Wing Anti-Ice Systems (thermal switch and continuous wire) by using TEMPCAL Probes.. Rapid heat rise . . . 3 minutes to 800°F! Fast cycling time of thermal switches . . . 4 to 5 complete cycles per minute for bench checking in production.

Tests EGT System Accuracy to ±4°C at Test Temperature

(functionally, without running the engine)

Tests RPM Accuracy to 10 RPM in 10,000 RPM (±0.1%)

The JETCAL is in worldwide use . . . by the U. S. Navy and Air Force as well as by major aircraft and engine manufacturers. Write, wire or phone for complete information.

B & H INSTRUMENT CO., INC.

3479 West Vickery Blvd. • Fort Worth 7, Texas

Sales-Engineering Offices:

VALLEY STREAM, L.I., N. Y.: 108 So. Franklin, LO 1-9220 • DAYTON, O.: 209 Commercial Bldg., BA 4-4563 • COMPTON, CAL.: 105 N. Bradfield St., NE 6-8970

ENGLAND: Bryans Aeroquipment Ltd. (Licensee), 15, Willow Lane, Mitcham, Surrey

Technical Literature Digest

M. H. Smith, *Associate Editor*, and M. H. Fisher, *Contributor*
The James Forrestal Research Center, Princeton University

Nuclear Propulsion

Tabulation, Bibliography and Structure of Binary Intermetallic Compounds, I. Compounds of Lithium, Sodium, Potassium, and Rubidium, by S. G. Epstein, D. M. Bailey, R. L. Smythe, G. R. Kilp and J. F. Smith, *Atomic Energy Comm.*, ISC-795, Sept. 1956, 31 pp.

Thermal and Electrical Properties of Graphite Irradiated at Temperatures from 100 to 425 K, by G. E. Deegan, *Atomic Energy Comm.*, NAA-SR-1716, Dec. 1956, 77 pp.

The Determination of Power and Temperature Overshoot in the Reactor Flash Problem, by K. T. Spinny, *Atomic Energy Comm.*, PNL-421, Nov. 1956, 16 pp.

Studies of Flow Distribution in the Core of a Quarter Scale Flow Model of the PWR Reactor, by Herbert R. Hazard and John M. Allen, *Atomic Energy Comm.*, BMI-1141, Oct. 1956, 46 pp.

Design Evaluation of BER (Boiling Experimental Reactor) in Regard to Internal Explosions, by F. B. Porzel, *Atomic Energy Comm.*, ANL-5651, Jan. 1957, 107 pp.

A Review of the Reaction Kinetics of Deuterium and Tritium Compounds, V: Association—Addition and Elimination Reactions, by Lawrence M. Brown, *Atomic Energy Commission*, NBS-4674, June 1956, 25 pp.

A Review of the Reaction Kinetics of Deuterium and Triterium Compounds, VI: Solvolysis Reactions, by Lawrence M. Brown, *Atomic Energy Comm.*, NBS-4712, July 1956, 18 pp.

Fusion for Flight, *Missiles and Rockets*, vol. 2, June 1957, p. 65.

Atomic Power Packages for Missile Launching Sites, *Missiles and Rockets*, vol. 2, June 1957, pp. 66–67.

Air Force Studies Ion Power, by Henry T. Simmons, *Missiles and Rockets*, vol. 2, June 1957, pp. 76.

M/r Bibliography, Atomic Power for Aircraft and Missiles, *Missiles and Rockets*, vol. 2, June 1957, pp. 136, 138, 140.

Ion Propulsion and Why, by Ernest Stuhlinger, *Missiles and Rockets*, vol. 2, June 1957, pp. 82, 84–85.

The Ion Rocket, by John E. Naugle, *Missiles and Rockets*, vol. 2, June 1957, pp. 87–88.

Fuels for the Atomic Rocket, by Alfred J. Zaehringer, *Missiles and Rockets*, vol. 2, June 1957, pp. 93–94.

Nuclear Powered Rockets, by Rudolf H. Reichel, *Missiles and Rockets*, vol. 2, June 1957, pp. 96–97.

Analysis of the Interaction of Electromagnetic Radiation with a Plasma in a Magnetic Field, by Laurence S. Hall, Andrew L. Gardner and Osmund T. Fundingsland, *Atomic Energy Comm.*, UCRL-4744, Sept. 1956, 34 pp.

Present Status of the Problem of Rocket Propulsion by Nuclear Energy, by F. Winterberg, *Fusées et Recherche Aeron.*, vol. 2, no. 1, March 1957, pp. 9–22 (in French).

Some Aspects of Nuclear Energy Propulsion, by Thomas Reis and Paul Ageron, *Fusées et Recherche Aeron*, vol. 2, No. 1, March 1957, pp. 23–33 (in French).

Pinch Effect, by Louis C. Burkhardt, Robert E. Dunaway, Joseh W. Mather, James A. Phillips, George A. Sawyer, Thomas F. Stratton, Emory J. Stovall Jr. and James L. Tuck, *J. Appl. Phys.*, vol. 28, May 1957, pp. 519–521.

EDITOR'S NOTE: Contributions from E. R. G. Eckert, J. P. Hartnett, T. F. Irvine Jr. and P. J. Schneider of the Heat Transfer Laboratory, University of Minnesota, are gratefully acknowledged.

"MONOBALL"®
Self-Aligning Bearings

CHARACTERISTICS

	ANALYSIS	RECOMMENDED USE
1	Stainless Steel Ball and Race	For types operating under high temperature (800-1200 degrees F.).
2	Chrome Alloy Steel Ball and Race	For types operating under high radial ultimate loads (3000-893,000 lbs.).
3	Bronze Race and Chrome Steel Ball	For types operating under normal loads with minimum friction requirements.

Thousands in use. Backed by years of service life. Wide variety of Plain Types in bore sizes 3/16" to 6" Dia. Rod end types in similar size range with externally or internally threaded shanks. Our Engineers welcome an opportunity of studying individual requirements and prescribing a type or types which will serve under your demanding conditions. Southwest can design special types to fit individual specifications. As a result of thorough study of different operating conditions, various steel alloys have been used to meet specific needs. Write for revised Engineering Manual describing complete line. Dept. JP-58.

SOUTHWEST PRODUCTS CO.
1705 SO. MOUNTAIN AVE., MONROVIA, CALIFORNIA

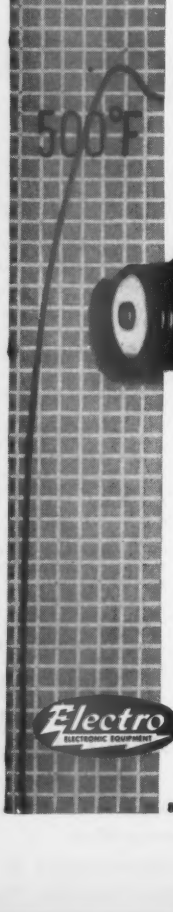

High Ambient Temperature Magnetic Transducers

translate mechanical motion into AC voltage

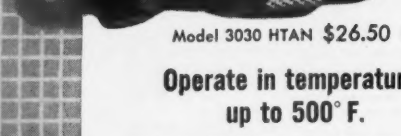

Actual size

Model 3030 HTAN $26.50 list

Operate in temperatures up to 500° F.

Internal Teflon construction and Teflon insulated wire.

Available in miniature size:
Model 3015 HT $16.50 list
(1-9/32" long — 1/3 oz.)

Write for new bulletin CMP 656 and quantity prices!

Electro ELECTRONIC EQUIPMENT

ELECTRO PRODUCTS LABORATORIES
4501-J Ravenswood Ave., Chicago 40, Ill.
Canada: Atlas Radio Ltd., Toronto

8067

Guidance Systems and Components

Functional Operation of Guidance and Control Components in Kay-1 (LARK) During Noise and Vibration Test, by E. D. Bush, *Naval Air Missile Test Center, Tech. Rep.* 13, April 1947, 44 pp. (Declassified from Confidential by authority by NAMTC letter A9/Ser. 362, 7/20/56.)

German Data on SG-66 Stabilizer, by E. L. Burnside, *North American Aviation, Inc., Rep.* AL202, June 1947, 55 pp. (Declassified from Confidential by authority of North American Aviation, Inc., letter 54D-6233, citing WADC letter WCSG, 8/6/54.)

Performance of the German SG-66 Stabilized Platform under Laboratory Conditions, by R. M. Benson, *North American Aviation, Inc., Rep.* AL357, June 1948, 24 pp. (Declassified from Confidential by authority of North American Aviation, Inc., letter 54D-6233, citing WADC letter WCSG, 8/6/54.)

Autopilot System of the NATIV (RTV-A-3) Missile, by K. R. Jackson and W. D. Lyon, *North American Aviation, Inc., Rep.* AL894, Nov. 1949, 85 pp. (Declassified from Confidential by authority of North American Aviation, Inc., letter 54D-6233, citing WADC letter WCSG, 8/6/54.)

Doppler Navigation, by William J. Tull, *Aeron. Engng. Rev.*, vol. 16, May 1957, pp. 58–61.

Radio Tracking, Orbit and Communication for the Earth Satellite, by John Pl. Hagen, *Aeron. Engng. Rev.*, vol. 16, May 1957, pp. 62–66.

Self-Contained Navigation Systems, by Robert W. West, *Aeron. Engng. Rev.*, vol. 16, May 1957, pp. 96–98.

Missile Guidance Techniques and Guided Missile Weapons System Considerations, by William C. Hodgson and John C. Ryon, *Fusées et Recherche Aeron.*, vol. 2, no. 1, March 1957, pp. 53–63 (in English).

Out-of-Print Copies Of JP Now Available

Under an agreement with the AMERICAN ROCKET SOCIETY, Kraus Reprint Corp., 16, E. 46th St., New York 17, N. Y., has made available complete back files of JET PROPULSION, dating back to the first year of publication.

Vols. 1–22 (1930–1952) are offered at $148.50, bound. In addition, Vols. 1–2, 3–7, 8–10 and 11–13 are available at $14 each, unbound; Vol. 14 and 15 at $9 per volume, unbound; Vol. 16, 17, 18, 19, 20 and 21 at $14 per volume, unbound; and Vol. 22 at $12, unbound. Single units or volumes can be supplied bound at $1.50 additionally per unit or volume. Vols. 23–26 are scheduled for reprint early this year.

Kraus is also offering back copies of the *Journal of the British Interplanetary Society.* Vols. 1–14 (1934–1955) are offered at $180, bound; Vols. 1–5 in one volume (sold as a unit only) at $20, unbound; and Vols. 6–14 at $20 per volume unbound.

STEPPER AUTOMATIC PULSE TIMER

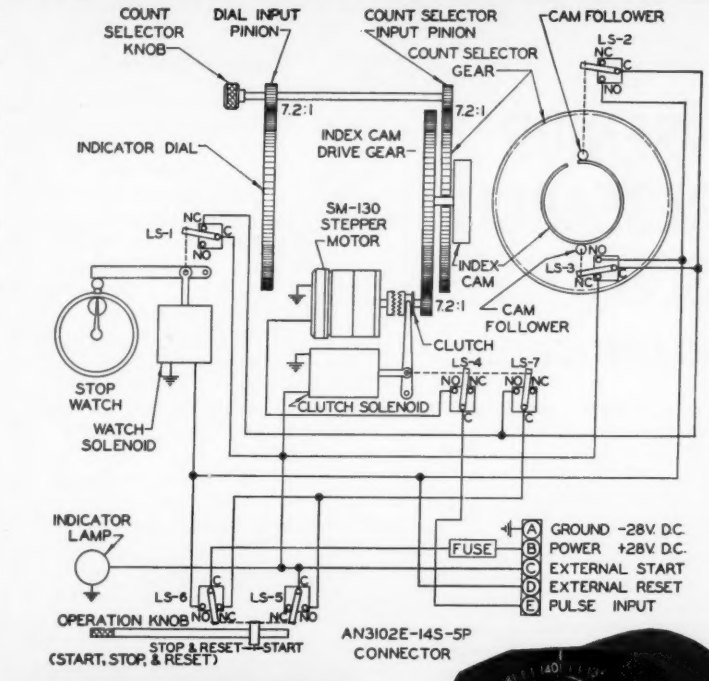

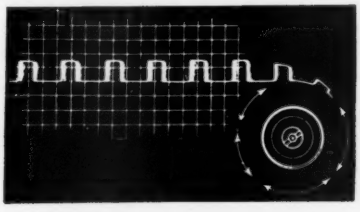

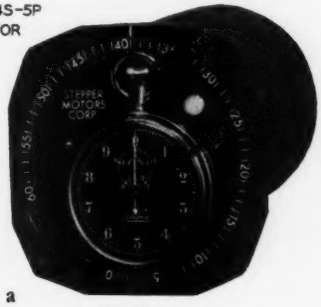

Model K-165

This Automatic Pulse Timer mounts in a standard 3⅛" mounting. The initial usage of the Automatic Pulse Timer was for a difficult instrumentation problem encountered on test aircraft—timing the pulses from a fuel flow transducer and thus determining specific fuel consumption. It successfully replaced a complex and unreliable method.

The Automatic Pulse Timer incorporates an uni-directional Stepper Motor along with complimentary gears, cams, solenoids, switches, an indicator light and—for an accurate independent time base—a stop watch. It is designed to visually record the lapsed time of an occurance of a specific number of electrical impulses. The Pulse Timer can count pre-selected quantity of 2 to 60 pulses, having a uniform or variable rate up to 25 pulses per second.

In this application the combined accuracy of the fuel flow transmitter and the automatic pulse timer is better than 1%, and of this the timer contributes essentially no error. When the broad input requirements are available, the unit can be used for timing pulses regardless of the source from which they may originate.

DETAILED OPERATIONAL SEQUENCE IS AVAILABLE UPON REQUEST.

STEPPER MOTORS CORPORATION

Subsidiary of California Eastern Aviation, Inc.

7441 West Wilson Avenue • Chicago 31, Illinois

• WEST COAST FACILITY 11879 W. FLORENCE AVE. CULVER CITY, CALIF.

SENIOR RESEARCH SCIENTIST

INTERIOR BALLISTICS

A challenging position now exists at Aerojet-General Corporation for a man of broad, fundamental background capable of original experimental and theoretical studies. The complex interrelations of mathematics, physics, and chemistry as applied to the interior ballistics of rockets offer challenging problems to the creative research man.

The application of unsteady-state theory to ignition of propellant and to the study of temperature-resistant materials is typical of the problems encountered. Combustion of solid propellants, the rheological behavior of solid propellants in complex grain configuration, and the gas flow and heat transfer in nozzles are related important fields for research.

Particularly important is the ability to formulate experiments for the verification of theoretical calculations, devise the necessary equipment, conduct the experiments, and analyze the data using the most advanced techniques, including digital and analogue computers.

For further details on this interesting position in an ideal Western climate,

write: Dr. James H. Wiegand, Head, Interior Ballistics Research Dept.

AEROJET-GENERAL CORPORATION
P.O. Box 1947
SACRAMENTO, CALIFORNIA

Recent Advances in Cermets

(*Continued from page 15*)

tions in addition to their high melting and oxidation resisting properties.

Bearing Materials

It might be worthwhile mentioning that a use of true cermets at relatively low temperatures has lately become interesting: The possibility of using these materials, with or without binder, as non-lubricated bearings is being investigated at temperatures between 800 and 1500 F (5). At these temperatures, the ordinary steels or common bearing materials either become too soft or their frictional properties are no longer favorable. It is believed that cermets might have a very interesting and important role to play in such applications. Not only does the high melting point indicate that they are unlikely to seize or gall at these temperatures, but the number of possible combinations of unlike materials is very large, especially if it is considered that both binder and hard phase can be varied. It would be desirable if not only the sleeve of the bearing could be produced from cermets but also the shaft; the latter should, however, be made of a different material. Problems of joining these materials to the standard steels would still have to be solved. The low friction properties against steel of WC-TiC cutting materials (which are a kind of a cermet) are well known, and it is believed that the further development and testing of hard metals against different hard metals will finally result in obtaining materials for high temperature bearing applications. Very little work has so far been done on the determination of frictional properties in the range of 1000 F, but the interest has been aroused, and it is believed that this field might bring about the first large-scale application for some of these materials.

Research and Development Work

Research and development work during the last few years has gone in two directions: The first one is an attempt to better understand the reasons why cermets behave as they do and to find, if possible, means to improve the impact resistance and ductility of some compositions. The other development work has investigated new production methods for cermet materials with the intention to increase the sizes of the parts which can be manufactured and to make fabrication of sheet-like parts possible.

Microstructure

The fundamental research work has concentrated on the study of the microstructure of a number of compositions and of the role the surface energy between metal binder and hard material plays in ductility and high temperature properties. This has been done both in systems involving true oxide ceramics and others using metallic refractories. The wetting properties between ferrous metals and copper on one side and ceramics and hard metals on the other have been carefully studied (6), and it was found that a zero wetting angle is at least desirable, if not necessary, for a good cermet material. The original idea that the strength at high temperature is due to a continuous skeleton of ceramic material is no longer considered correct (7), at least for the largest number of cases. On the contrary, it was found that isolated particles uniformly dispersed in a matrix result in much more desirable properties (8). Impact behavior is improved without sacrifice of strength. Norton's idea (9) that the strength of a cermet is essentially due to the peculiar state of stress in the binder material seems to be substantiated. The dependence of strength and other properties on the distribution of these isolated particles in the matrix, as well as on the size of the particles themselves, has also helped to bring about a better understanding of these materials (10). Infiltration of a carbide skeleton with metal binder material has been used as a means to obtain a desirable microstructure. After infiltration and soaking of the material at high temperature, the original skeleton is not preserved, but the carbide particles become separated from each other and well distributed in the matrix (11). However, it must be said that all these attempts (in spite of the progress they might have brought towards a better understanding) have not been able to produce a material which would be usable without fundamentally changing the design presently in use for engines or other applications. It is still too difficult to work with essentially brittle materials. A lot has to be learned about the interactions between binder and hard material, about the nature of the bond between the two constituents, and about the effect the microstructure has on the general properties. We are far from the time where we can prescribe a certain microstructure in order to impart to a material the properties desirable for a certain application. We know, however, that the degree to which the fundamental properties of both constituents become apparent in the behavior of the final product depends to a large extent on the microstructure present. It seems now, even more so than some years ago, that the kind and nature of refractory hard metal or ceramic used in the cermet material is of lesser importance than the distribu-

tion of the particles within the matrix. How far grain size plays a role in the pure hard metals or ceramics is still not too certain.

The materials most frequently used for all these investigations are the standard cermets. No essentially different material has been developed or investigated during the last few years. This is due to the reasoning mentioned above. Titanium carbide-nickel cermets have been most widely studied and some work has been done on chromium carbide, titanium boride, zirconium boride and some similar materials. In the case of mixtures of true ceramics with metals, alumina-base cermets have been studied (12) and a magnesium oxide-nickel material (13) has been developed.

A peculiar kind of cermet was recently produced for applications in the nuclear energy field, especially for control rods. The material is used rather extensively and is called "Boral"; it consists of boron carbide dispersed in an aluminum matrix. It can be rolled out into sheets. The same idea is applied to a stainless steel material containing Samarium or Europium or Gadolinium oxide (14). An excellent, uniform distribution of the neutron absorbing material within the steel matrix can be obtained. On the other hand, the use of pure borides and silicides of rare earth metals such as Gadolinium, Dysprosium or Europium was recently made possible (15).

New Production Methods

The development of new manufacturing procedures has borrowed a lot of experience from the ceramic industry. Slip casting (16) has found applications in the production of larger parts, crucibles or containers from cermet materials. The standard methods are applied with only slight modifications.

To produce even larger pieces, or to impart the desirable cermet properties to very large areas, coating processes have been developed. The well-known method for spraying oxide materials can also be applied, with some modifications, to cermets. It is now possible to coat steels, graphite, refractories and other materials with borides, silicides and carbides which melt below 5000 F. Development work to extend the spraying methods to extremely high melting materials is in progress. For the time being, coatings are applied as protection against attack by liquid metals (17), but applications as high temperature protection are under test. The coatings are usually porous which, however, has proved to be non-objectionable in many cases. Another offspring of this development is the production of large pieces by spraying the cermet material against a thin sheet metal form (18). The material can be deposited to any

THESE ENGINES ARE NOW IN PRODUCTION AT C. A. E.

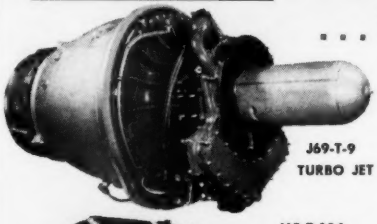
J69-T-9 TURBO JET

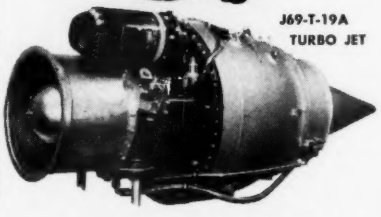
J69-T-19A TURBO JET

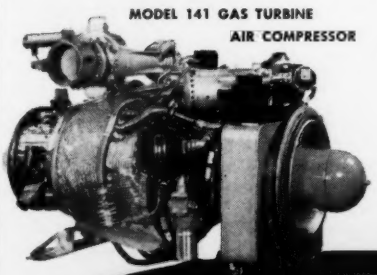
MODEL 141 GAS TURBINE AIR COMPRESSOR

... the T-37 Twin Jet Trainer with C. A. E. Turbine Power

Air Corps flight training routine took a significant step forward recently, when the T-37 twin jet trainer entered its Phase VIII testing at Bainbridge Air Base, Georgia. Twenty hand-picked officers embarked on a course known as PROJECT PALM, with the two-way goal of training for them, and suitability testing for the plane. This new high-performance ship advances the jet phase of fliers' training to an earlier stage in the training schedule, speeding the transition from propeller-driven planes to jets, with gains in both safety and economy. Twin J69-T-9 turbines by C.A.E. provide the power.

CONTINENTAL AVIATION & ENGINEERING CORPORATION
12700 KERCHEVAL AVENUE, DETROIT 15, MICHIGAN
SUBSIDIARY OF CONTINENTAL MOTORS CORPORATION

GILMORE

SIX COMPONENT THRUST MEASURING SYSTEM*

Completes First Year of Missile Testing

Installed at a West Coast missile testing facility, in August, 1956, this Gilmore weight and thrust measuring system indicates and records values of missile weight, propellant weight, thrust, gimballing motor forces, and thrust mis-alignment forces. Forces are translated into values represented by terms (a) weight and thrust, (b) pitch moment, (c) yaw moment, (d) roll moment, (e) XX axis sideload, (f) YY axis sideload. The system compensates for the effect of sideload with respect to wind and with respect to interaction with moments.

Computing equipment isolates all fixed components. A portable calibration unit, calibrated by the National Bureau of Standards, is included in the installation. System accuracy is 0.1%.

*Patents Pending

For details on this and other Gilmore Systems Write Dept. J-1

Instrumentation Systems For Industry and Science

GILMORE INDUSTRIES, INC.
5713 Euclid Ave. • Cleveland 3, Ohio
West Coast Office: 5245 King St., Riverside, Calif.

desired thickness, and a strong part is formed which has no dimensional limitations. The sheet metal form can later be removed by chemical means if desired, so that a pure cermet piece is obtained as an end-product. The surface of the pre-form is reproduced in every detail and a smooth surface can readily be obtained. Ribs or other stiffeners can be incorporated without difficulty. The method is still in its infancy, but it is expected to open new applications for cermet materials. Nose cones, leading edge parts and similar components which were formerly produced from sheet metal seem to be naturals for this method. The strength of the material as produced by this "Spray-Forming" method should be satisfactory for most applications. If desired, however, an additional sintering treatment can be applied which improves the properties to some degree.

Even though the developments of the last two years have not shown a considerable increase in the application of cermets, it seems to be clear that these materials are still of extreme interest for all high temperature applications, both in the aircraft and in the nuclear industries. Designing for cermet materials is still very difficult, and a lot has to be learned to make good use of them. However, as the requirements for higher temperatures are increasing constantly, we will soon have reached a point where no other materials but cermets, hard metals and oxide ceramics will have a chance for proper performance.

References[3]

1 Luini, L., "Material Property Requirements and Test Methods," Conference on Heat Tolerant Metals, Albuquerque, N.M. (1957).

2 Steinitz, R., "Cermets, New High Temperature Materials," JET PROPULSION, vol. 25, 1955, p. 326; "Cermets and Metallic Refractories," *Aviation Age*, R & D Technical Handbook (1957), p. F-6.

3 Steinitz, R., "Materials for Very High Temperatures," *Powder Metallurgy Bulletin vol.* 7, (1956), p. 155.

4 Warde, J. M., "Materials for Nuclear Power Reactors," *Materials & Methods*, vol. 44, no. 2, (1956), p. 121.

5 Battelle Memorial Institute, "Investigation of Ceramic and Cermet Materials to Evaluate Friction, Wear, Overall Compatibility and General Operating Characteristics Under Various Environmental Conditions," WADC Contract AF 33(616)-3995 (1957).

6 Hamjian, H. J. and Lidman, W. G., "Investigation of Bonding Between Metals and Ceramics I," NACA TN 1948 (1949); Graham, J. W., "Sintered Titanium Carbides," *Iron Age*, vol. 172 (1953), p. 148; Humenik, M., and Parikh, N. M., "Fundamental Concepts Related to Microstructure and Physical Properties of Cermet Systems," *Journal of the American Ceramic Society*, vol. 39, (1956), p. 60; Parikh, N. M. and Humenik, M., "Wettability and Microstructure Studies in Liquid Phase Sintering," *Journal of the American Ceramic Society*, vol. 40, (1957), p. 315; Baxter, J. R. and Roberts, A. L., "Development of Metal Ceramics From Metal Oxide Systems," Symposium on Powder Metallurgy, Iron and Steel Institute, p. 315, (London 1956).

7 Sandford, E. J. and Trent, E. M., "The Physical Metallurgy of Sintered Carbides," Symposium on Powder Metallurgy, Iron and Steel Institute, p. 84, (London 1947); Norton, J. T., "Some Observations on the Role of the Binder in Cemented Refractory Alloys," *Powder Metallurgy Bulletin* vol. 6, (1951), p. 75; Gurland, J. and Norton, J. T., "Role of the Binder Phase in Cemented WC-Co Alloys," *Trans. AIME*, vol. 194, (1952), p. 1051; Humenik, M. and Parikh, N. M., "Fundamental Concepts Related to Microstructure and Physical Properties of Cermet Systems," *Journal of the American Ceramic Society*, vol. 39, (1956), p. 60.

8 Shaler, A. J., "Factors in TiC-Base Cermets," WADC TR 52-327 (1952). Probst, H. B., and McHenry, H. T., "A Study of the Impact Behavior of High Temperature Materials," NACA TN 3894 (1957).

9 Norton, J. T., "Some Observations on the Role of the Binder in Cemented Refractory Alloys," *Powder Metallurgy Bulletin* vol. 6, (1951), p. 75.

10 Gurland, J., and Bardzil, P., "Relation of Strength, Composition and Grain Size of Sintered WC-Co Alloys," *Trans. AIME*, vol. 203, (1955), p. 311.

11 Skolnik, L. P., and Goetzel, C. G., "TiC Products Produced by the Infiltration Technique," ASTM Spec. Techn. Publ. 174 (1956). Blumenthal, H., and Silverman, R., "A Study of the Microstructure of TiC," *Trans. AIME*, vol. 203, (1955), p. 317.

12 Lindenthal, J. W., Stradley, J. G., and Shevlin, T. S., "Alumina-Base Cermets," WADC TR 54-173 (1957).

13 White, A. E. S., et al, "Metal Ceramic Bodies," Symposium On Powder Metallurgy, Iron & Steel Institute, p. 311 (London 1956). Montgomery, E. T., and Rempes, P. E., "Exploratory Study of Ni-Magnesia Cermets," WADC TR 53-164 (1953).

14 Ray, W. E., "Extrusion of a Complex Shape Through a Round Die," *Metal Progress*, vol. 72, no. 3, (1957), p. 65.

15 Recent Development of American Electro Metal Div. of Firth Sterling, Inc., Yonkers, N.Y.

16 Hausner, H. H., and Ferries, D. P., "Metal Powder Slip Castings," *Materials & Methods*, vol. 3, no. 5, (1956), p. 132.

17 "Boride Coating Protects Metals Exposed to Molten Aluminum," *Materials & Methods*, vol. 44, no. 4, (1956), p. 143.

18 New Development of American Electro Metal Div. of Firth Sterling, Inc., Yonkers, N.Y.

[3] The given references are only a small and rather arbitrary selection of a large number of publications. They will describe more in detail the ideas mentioned in this paper, but they should not be taken as being the most important ones.